



# Durham E-Theses

---

## *Blade row interaction in radial turbomachines*

Sato, Kenji

### How to cite:

---

Sato, Kenji (1999) *Blade row interaction in radial turbomachines*, Durham theses, Durham University. Available at Durham E-Theses Online: <http://etheses.dur.ac.uk/4349/>

### Use policy

---

The full-text may be used and/or reproduced, and given to third parties in any format or medium, without prior permission or charge, for personal research or study, educational, or not-for-profit purposes provided that:

- a full bibliographic reference is made to the original source
- a [link](#) is made to the metadata record in Durham E-Theses
- the full-text is not changed in any way

The full-text must not be sold in any format or medium without the formal permission of the copyright holders.

Please consult the [full Durham E-Theses policy](#) for further details.

# **BLADE ROW INTERACTION IN RADIAL TURBOMACHINES**

**Kenji Sato**

School of Engineering, University of Durham

The copyright of this thesis rests  
with the author. No quotation  
from it should be published  
without the written consent of the  
author and information derived  
from it should be acknowledged.

A dissertation submitted to the University of Durham

for the degree of Doctor of Philosophy

September 1999



27 JAN 2000

# PREFACE

Now I am coming to the end of the research work of my Ph. D. course and recollecting my memories during the stay in Durham. I have been supported by so many people academically and other matters.

First of all, I would like to express my gratitude to my supervisor Dr. Li He for his continuous and uncompromising guidance and monumental patience. Without them, this research work would still be far from finished. I am also deeply indebted to Prof. Nagashima in Japan for providing me an opportunity to do research under the supervision of Dr. Li He.

The discussions with my colleagues, Dr. Wei Ning, Dr. Jerry Ismael, Dr. David Bell, Stephen Dewhurst, Olivier Queune, Dr. Tie Chen, Yun Zheng, P Vasanthakumar, have been very useful. This dissertation owes much to the ideas and knowledges inspired through them. Dr. Wei Ning deserves my additional thanks for giving me tactful advice on CFD and also being a good friend since I arrived in Durham. His special Chinese cuisine at his home party was wonderful!

I must acknowledge my debt to Manami Uchida, David Sims-Williams and Anthony Ryan for their help to improve the text of the dissertation, which resulted in large amounts of important corrections and improvements in description.

I am also indebted to Mitsubishi Heavy Industries in Japan for the partial support of the project on the development of the numerical flow method.

Finally my thanks to Katsue, Yuko, Hiroyuki and Masa for their support. I would like to dedicate this dissertation and my labour throughout this Ph.D course to them.

# ABSTRACT

A computational study has been performed to investigate the effects of blade row interaction on the performance of radial turbomachines, which was motivated by the need to improve our understanding of the blade row interaction phenomena for further improvement in the performance.

High-speed centrifugal compressor stages with three settings of radial gap are configured and simulated using a three-dimensional Navier-Stokes flow method in order to investigate the impact of blade row interaction on stage efficiency. The performance predictions show that the efficiency deteriorates if the gap between blade rows is reduced to intensify blade row interaction, which is in contradiction to the general trend for stage axial compressors. In the compressors tested, the wake chopping by diffuser vanes, which usually benefits efficiency in axial compressor stages, causes unfavourable wake compression through the diffuser passages to deteriorate the efficiency.

Similarly, hydraulic turbine stages with three settings of radial gap are simulated numerically. A new three-dimensional Navier-Stokes flow method based upon the dual-time stepping technique combined with the pseudo-compressibility method has been developed for hydraulic flow simulations. This method is validated extensively with several test cases where analytical and experimental data are available, including a centrifugal pump case with blade row interaction. Some numerical tests are conducted to examine the dependency of the flow solutions on several numerical parameters, which serve to justify the sensitivity of the solutions. Then, the method is applied to performance predictions of the hydraulic turbine stages.

The numerical performance predictions for the turbines show that, by reducing the radial gap, the loss generation in the nozzle increases, which has a decisive influence on stage efficiency. The blade surface boundary layer loss and wake flow mixing loss, enhanced with a higher level of flow velocity around blading and the potential flow disturbances, are responsible for the observed trend.

# TABLE OF CONTENTS

<b>1. INTRODUCTION .....</b>	<b>1</b>
1.1. GENERAL INTRODUCTION .....	1
1.2. RADIAL TURBOMACHINES .....	2
1.3. BLADE ROW INTERACTION .....	4
1.4. NUMERICAL METHODS FOR BLADE ROW INTERACTION PROBLEMS .....	5
1.5. OVERVIEW OF THE PRESENT RESEARCH .....	6
<b>2. LITERATURE SURVEY.....</b>	<b>8</b>
2.1. INTRODUCTION .....	8
2.2. CENTRIFUGAL COMPRESSORS AND PUMPS .....	8
2.3. RADIAL TURBINES .....	11
2.4. LOSS MECHANISMS .....	12
2.5. NUMERICAL METHODS FOR BLADE ROW INTERACTION PROBLEMS .....	15
2.6. INCOMPRESSIBLE FLOW METHODS .....	21
2.7. CONCLUDING REMARKS .....	24
<b>3. BASELINE NUMERICAL METHOD FOR COMPRESSIBLE FLOWS .....</b>	<b>26</b>
3.1. GOVERNING EQUATIONS.....	26
3.2. NUMERICAL SCHEME.....	27
3.3. TREATMENT OF VISCOUS TERMS .....	29
3.4. TIME-CONSISTENT MULTI-GRID TECHNIQUE .....	29
3.5. BOUNDARY CONDITIONS .....	30
3.6. SLIDING BOUNDARY TREATMENT BETWEEN BLADE ROWS.....	31
3.7. PARALLEL COMPUTING .....	32
<b>4. VALIDATION OF THE COMPRESSIBLE FLOW METHOD .....</b>	<b>33</b>
4.1. INTRODUCTION .....	34

4.2.	KRAIN'S CENTRIFUGAL IMPELLER .....	33
4.3.	NUMERICAL CONDITIONS .....	34
4.4.	PERFORMANCE MAPS .....	35
4.5.	CIRCUMFERENTIALLY AVERAGED STATIC PRESSURE.....	36
4.6.	STREAMWISE MEASUREMENT SECTIONS .....	36
4.7.	MESH DEPENDENCY .....	39
4.8.	EFFECT OF TIP CLEARANCE FLOW .....	40
4.9.	SUMMARY.....	40
<b>5.</b>	<b>ANALYSIS OF HIGH SPEED CENTRIFUGAL COMPRESSOR STAGES</b> .....	<b>42</b>
5.1.	INTRODUCTION .....	42
5.2.	CENTRIFUGAL COMPRESSOR FLOWS WITH BLADE ROW INTERACTION .....	42
5.3.	SUMMARY.....	51
<b>6.</b>	<b>DEVELOPMENT OF AN INCOMPRESSIBLE SOLUTION METHOD</b> .....	<b>52</b>
6.1.	INTRODUCTION .....	52
6.2.	GOVERNING EQUATIONS.....	53
6.3.	DUAL-TIME INTEGRATION SCHEME .....	54
6.4.	EIGEN-VALUE SCALED NUMERICAL DAMPING.....	57
6.5.	BOUNDARY CONDITIONS .....	59
6.6.	MULTI-GRID SOLUTION ACCELERATION TECHNIQUES.....	59
6.7.	ISSUES ON CAVITATION .....	61
6.8.	PARALLEL COMPUTING .....	62
<b>7.</b>	<b>VALIDATION OF THE INCOMPRESSIBLE FLOW METHOD</b> .....	<b>65</b>
7.1.	INTRODUCTION .....	65
7.2.	DURHAM LINEAR TURBINE CASCADE.....	66
7.3.	UNSTEADY LAMINAR BOUNDARY LAYER.....	69
7.4.	CENTRIFUGAL PUMP WITH VANED DIFFUSER .....	74

7.5. SUMMARY.....	80
<b>8. ANALYSIS OF HYDRAULIC TURBINE STAGES .....</b>	<b>82</b>
8.1. INTRODUCTION.....	82
8.2. FRANCIS TURBINE FLOWS WITH BLADE ROW INTERACTION .....	83
8.3. SUMMARY.....	90
<b>9. CONCLUSIONS AND RECOMMENDATIONS .....</b>	<b>92</b>
9.1. NUMERICAL METHOD.....	92
9.2. FLOWS IN CENTRIFUGAL COMPRESSORS.....	94
9.3. FLOWS IN RADIAL TURBINES.....	95
9.4. SUGGESTIONS FOR FUTURE RESEARCH.....	96
<b>REFERENCES.....</b>	<b>99</b>
<b>APPENDICES .....</b>	<b>110</b>
APPENDIX 1. ABSOLUTE FLOW ANGLE IN RADIAL FLOW PASSAGE .....	110
APPENDIX 2. ANGLE OF WAKE LINES IN RADIAL FLOW PASSAGE .....	111
APPENDIX 3. WAKE LENGTH IN RADIAL FLOW PASSAGE .....	113
APPENDIX 4. ENTROPY IN INCOMPRESSIBLE SUBSTANCES.....	115
<b>FIGURES.....</b>	<b>116</b>

# NOMENCLATURE

A	Surface area of control volume [m <sup>2</sup> ]
C	Absolute velocity [m/s]
D	Diameter [m]
E	Fluid internal energy [J/kg]
F	Flux vector in x direction
G	Flux vector in $\theta$ direction
H	Flux vector in r direction
L	Typical length scale
NPSH	Net positive suction head
Q	Volumetric flow rate [m <sup>3</sup> /s]
R	Gas constant [J/kg·K] or net flux vector
$\tilde{R}$	Modified net flux vector for dual-time stepping technique
Re	Reynolds number
S	Source term vector
SI, SJ, SK	Directed face area in i, j, k surfaces
T	Temperature [K] or Torque [N·m]
T <sub>v</sub>	Shear stress vector
U	Rotation speed of rotor [m/s] or Conservative variable vector
U <sub>∞</sub>	Free stream flow velocity [m/s]
V	Velocity [m/s] or Volume [m <sup>3</sup> ]
W	Relative flow velocity [m/s]
Y <sub>p1</sub> , Y <sub>p2</sub>	Blade pitch angle
b	Passage height [m]
c <sub>f</sub>	Skin friction coefficient
f	Physical frequency [Hz]



$h_s$	Absolute stagnation pressure head at pump inlet or at turbine exit
$h_v$	Absolute vapor pressure head
$k$	Reduced frequency
$\dot{m}$	Mass flow rate
$n$	Unit vector
$p$	Static pressure [ $N/m^2$ ]
$p_t$	Total pressure [ $N/m^2$ ]
$r$	Representative radius of control volume [m]
$s$	Entropy [kg·K/J]
$t$	Physical time [s]
$\tilde{t}$	Pseudo time [s]
$u$	Velocity component in axial direction [m/s]
$v$	Velocity component in circumferential direction[m/s]
$w$	Velocity component in radial direction[m/s]
$\Theta$	Conservative variable vector with pseudo-compressibility
$\tilde{\Theta}$	Conservative variable vector for incompressible flow
$\Phi$	Local numerical damping coefficient
$\beta$	Sound speed [m/s]or Artificial sound speed [m/s]
$\gamma$	Specific heat ratio
$\varepsilon$	Local numerical damping coefficient
$\eta$	Efficiency
$\mu$	Viscosity [kg/m·s]
$\rho$	Density of fluid [kg/m <sup>3</sup> ]
$\tau$	Shear stress
$\phi$	Flow rate coefficient = $\frac{4Q}{U_2 \pi D_2^2}$

$\psi$  Total pressure rise coefficient =  $\frac{P_{t4} - P_{t0}}{\rho U_2^2}$

$\omega$  Rotation speed [radian/s]

### Subscript

avg Averaged value

c,m,f Coarse, intermediate and fine meshes in the multigrid method

exit Exit of computational domain

i,j,k Indices of grid in three directions

inlet Inlet of computational domain

ref Reference value

t Stagnation state

w Wall surface

x Axial component

r Radial component

$\theta$  Circumferential component

0 At inlet

1 At leading edge of first blade row

2 At trailing edge of first blade row

3 At leading edge of second blade row

4 At trailing edge of second blade row

### Superscript

n Physical time level

m Pseudo-time level in the dual-time stepping technique

$\bar{(\ )}$  Unsteady perturbation

# 1. INTRODUCTION

## 1.1. General Introduction

The advantage of radial configurations for turbomachinery has been well recognised in a wide variety of applications, including small aircraft gas turbines, industrial gas turbines, turbochargers and hydraulic machines. The radial flow turbomachines are usually configured with stator vanes (figure 1-1) that either diffuse (compressors, pumps) or accelerate (turbines) the flows for energy transfer, although vaneless configurations are preferred for small systems where manufacturing cost is of most importance. In multiple blade row configurations, adjacent blades (rotor and stator) will interact with each other in an unsteady manner. This phenomenon is called *blade row interaction*, an essential feature of any turbomachinery stages. In general, spacings between rotor blades and stator vanes in radial turbomachines tend to be smaller than those found in axial turbomachines. For this reason, blade row interaction in radial turbomachines would be stronger than that in axial turbomachines. Therefore, an adequate estimation of the effects of blade row interaction is essential for the improvement in efficiency and for structural analysis of radial turbomachines.

With development of efficient numerical flow methods (*Computational Fluid Dynamics: CFD*) and ever-increasing performance of digital computers, it is now feasible to analyse the blade row interaction effects numerically. The numerical flow analyses provide high-resolution information in time and space, which would be otherwise very difficult to achieve in experimental flow analyses. In fact, for axial flow machines, many numerical analyses concerning the blade row interaction effects have been published in the literature. However, the works on radial stage turbomachines related to the blade row interaction effects are very limited. This lead to the main motivation of the present work. The main emphasis of the work is placed on the correlation between the aerodynamic performance of radial turbomachinery stages and the radial gap between rotor blades and stator vanes.

## 1.2. Radial Turbomachines

In a radial configuration, the blade speed changes considerably along streamlines so that the relative velocity change through a rotor passage required for a specified enthalpy change is less than that found in an axial counterpart. For centrifugal compressors and pumps, this means a higher pressure-rise is obtainable with the same amount of diffusion rate through the impeller passage. This is advantageous since it is the diffusion of the relative flow that brings about the boundary layer growth and separations responsible for major losses. For radial flow turbines, the reduced change in relative velocity implies that higher pressure-ratio can be applied before the onset of some phenomena with significant loss generation (e.g. transonic losses, cavitation, etc).

The radial configuration inherently involves a 90-degree bend of flow from the axial to radial direction or vice versa in the meridional plane. This usually results in a long twisted three-dimensional rotor passage in order to realise smooth flow development. The blade angle of the rotor may change considerably from the inlet to the exit, and this results in the directional changes of the centrifugal force due to the blade curvature. From a structural requirement, the hub of a rotor blade needs to be much thicker than the tip. Consequently, the solidity of rotor blades changes considerably in the spanwise direction. For high-pressure-ratio radial turbines with high entry-temperature, this effect becomes even more severe since they have to accommodate the cooling air passage.

Hence, flows in the rotors of radial machines usually are of a high three-dimensionality. They are characterised by streamwise vortices generated along wall surfaces and interactions among them. The mechanism of a vortex pair on rotor blade surfaces, for example, can be explained in a relatively rotating frame as follows: the coriolis acceleration due to the shaft rotation and the centrifugal force due to the meridional curvature of the passage usually produce a positive pressure gradient toward the hub in the spanwise direction (figure 1-2a). Meanwhile, the relative flow velocity distribution is not uniform between blades and tends to have the highest velocity in the middle, and the velocity decreases toward the blade surfaces due to wall shear stress. Since the effect of the coriolis acceleration and the centrifugal force is proportional to the local relative flow velocity, the flow in the middle passage tends to be directed toward the hub while the flow near the blade surfaces is directed toward the casing.

Consequently, a vortex is formed on each blade surface (figure 1-2b). Similarly, a vortex is formed on each endwall surface (figure 1-3a) due to the coriolis acceleration in the pitchwise direction (figure 1-3b). The actual flow patterns inside the passage depend strongly on the relative strengths of those streamwise vortices so that only a fully three-dimensional viscous flow analysis method will provide realistic pictures of the radial turbomachinery flows.

Interactions between the streamwise vortices and the wall shear layers usually culminate in a severely deformed flow discharged from radial rotors. For centrifugal compressors and pumps, the discharged flows from the impeller is referred to as *jet-wake flow* (Dean and Senoo 1960) named from a distinct low momentum fluid region that usually locates on the suction side and that is segregated from the high speed main flow (figure 1-4a). For radial turbines, Huntsman (1993) observed a distorted flow discharged from a turbine rotor with low momentum fluid on the shroud/suction surfaces in the experimental study (figure 1-4b). It has been known that the performance and stable operating range of radial rotors are adversely affected by the presence of the exit flow non-uniformity (Zangeneh et al. 1999)

For systems with stator vanes, blade row interaction is present between the rotor and the stator. In order to change the intensity of blade row interaction, which is known to influence the efficiency and the structural integrity of the systems, spacing between the rotor and the stator (radial gap) is the possible parameters to be varied. Conventional approaches estimating stage performance are mostly based upon parametric performance analyses with experimental correlation (Watanabe et al. 1971, Amineni et al. 1996, Tamaki et al. 1999). Since they are not necessarily founded on flow physics, it is difficult to guarantee the applicability of experimental correlations between certain parameters and the performance to other types of machines.

In the design of radial turbomachines, the radial gap should be decided through the optimization among several design parameters (e.g. size, weight, structure, etc.). Whereas the radial gap may have a large bearing on overall efficiency, other design parameters may take precedence. For aeroengine applications, the size and the weight of the system will become important requirements to be met. On the other hand, for high speed turbomachines and hydraulic machines, structural integrity of the systems will be of greater concern. For instance, the blade natural frequencies must be compared with the blade passing frequencies to ensure that they are not too close. A Campbell diagram is

widely used for the purpose (Came and Robinson 1999). However, a certain level of radial gap between the rotor and the stator must be kept to ensure that there is an adequate durability (Flaxington and Swain 1999).

Modern CFD techniques have been applied successfully to the computations of steady flows in radial turbomachines. Viscous solution methods solving Reynolds-averaged Navier-Stokes equations can include practically all the information necessary to reproduce flow structures. Even in early numerical attempts with relatively coarse grids, development of the non-uniform flow structure with a segregated low momentum flow was captured. For stage flows, very few efforts have been made so far to simulate flows with blade row interaction using numerical methods.

### 1.3. Blade Row Interaction

Flows in turbomachinery are inherently unsteady. The flow in the discrete passages between the blading of turbomachines presents non-uniformity in the pressure and velocity distributions. In the presence of the relative movements of the blade rows due to the shaft rotation, the non-uniformity of the flow generated by blades in a row is seen as a periodic disturbance in the other frame. As demonstrated by Dean (1959), the flow unsteadiness provides the basic mechanism for energy transfer, which is essential to the operation of turbomachines. If the rotating blade row is located relatively close to the stationary row, circumferential flow non-uniformities in the relative frame generated by both rows are expected to interact with each other in an unsteady manner. These effects are usually classified into *potential flow effect* and *wake flow effect* depicted in figure 1-5. The potential flow effect is an inviscid flow phenomenon produced by the non-uniform pressure distribution around the blading. The effect can propagate both upstream and downstream at the speed of sound relative to the local flow and it usually decays relatively quickly. The wake flow originates from the blade surface boundary layers of upstream blade rows and is a viscous phenomenon although interactions of the wake with downstream components occur through both inviscid and viscous mechanisms. The magnitude of the wake decays relatively slowly by viscous diffusion.

Recently, active research on the blade row interaction phenomena in axial turbomachines have shed light on the understanding of generic loss mechanisms due to

various sources (Adamczyk 1996, Valkov and Tan 1998). Among them, there are two mechanisms with significant influences on the performance: *wake recovery* that usually benefits efficiency (Smith 1966) and *wake/boundary layer interaction* that is often detrimental to efficiency (Addison and Hodson 1990). For axial flow compressors, reducing the blade row spacing usually benefits efficiency due to the dominant influence of the wake recovery. However, the effect of blade row spacing in axial flow turbines is less clear although many experiments observed reduced efficiency at smaller blade row spacing.

Given the progress in the area of blade row interaction effects on axial flow machines, experimental and numerical research on blade row interaction in radial configurations are very limited. For radial machines, blade row spacing may be used to control intensity of the interaction as in axial flow machines, but little study of this kind has been reported.

#### 1.4. Numerical Methods for Blade Row Interaction Problems

CFD techniques are playing a greater role in the flow analysis of turbomachinery. In fact, numerical simulations based upon the Euler and Navier-Stokes equations have become invaluable tools not only for flow analysis but also for industrial turbomachinery design (Dawes and Denton 1999). The applications cover a wide range from transonic axial turbomachinery flows to centrifugal pumps. In the last decade, the development of efficient numerical methods has contributed to a considerable progress on the physical understanding of the flow phenomena. Currently, most numerical flow simulations are carried out under steady conditions that implicitly assume that the blade rows in stage turbomachines are sufficiently far apart so that the flows between the blade rows are uniform in both space and time. In reality, the blade row spacing is very small for various reasons (e.g. size, efficiency, etc.). Consequently, the flow around the blading of the turbomachines is usually highly unsteady and, for further improvement of the turbomachinery design, it is necessarily required to take into account the impact of the blade row interaction effects in performance evaluation.

Recently various numerical approaches have been adopted to simulate the blade row interaction effects. The simplest approach is to introduce a *mixing plane* between

blade rows where information can communicate through pitchwise-averaged values of flow variables (Denton 1992). The methods with the mixing plane offer the efficiency of steady flow approach while they take into account the “steady” blade row interaction effects. Recent efforts to model the unsteady blade row interaction effects on time-averaged flow quantities are showing encouraging results (Rhie et al. 1998). Non-linear time-marching approaches provide the most physically realistic way to simulate unsteady flows so that the methods have been applied almost exclusively to basic flow analyses in blade row interaction phenomena (e.g. Erdos et al 1977, Rai 1985, 1987, Giles 1988).

Flow governing equations are usually solved by time-integration algorithms. They can be classified into two classes: density based time-marching, usually referred to simply as the *time-marching method* and pressure based method referred to as the *pressure correction method*. The density based time-marching method originally developed to calculate transonic flow problems has been well adapted to other flow speed range for both steady and unsteady conditions. The method, however, has severe limitation in low speed flows where density change becomes very small. Chorin (1967) proposed a method to solve incompressible flow governing equations by introducing pseudo-compressibility in time-marching algorithm. The *pseudo-compressibility method* is not time-accurate so that the method in its original form cannot be applied to unsteady flow computations. The pressure correction approach (Harlow and Welch 1965) was originally developed to solve incompressible flows but later extended to deal with flow compressibility. The method has been mainly applied to steady flow simulations, but it is also applicable to unsteady flows by solving the pressure correction equation accurately at each discrete time step.

## 1.5. Overview of the Present Research

The principal objective of the research described in the following chapters is to evaluate the impact of the blade row interaction effects on the performance of radial turbomachines, covering a wide range of Mach number including incompressible flows for hydraulic machines. The research is carried out purely numerically.

Several relevant matters are reviewed through a survey of literature in Chapter 2. This deals with the developments of basic physical understanding of steady and



unsteady radial turbomachinery flows and relevant loss mechanisms and the latest advancement of numerical methods to tackle these problems.

For compressible flow simulations, a 3D unsteady multi-stage compressible turbomachinery flow method “TF3D” developed by He (1996c) was used. In Chapter 3, basic structure and methodology of the flow method are described. The flow method was validated with a centrifugal compressor flow as described in Chapter 4. Then it was applied to the unsteady flow simulations in the stage centrifugal compressors in order to investigate the effect of blade row interaction on the system performance. Those numerical results are presented in Chapter 5.

A new unsteady incompressible flow method “TF3D-M0” was developed through the course of the research. The solution method is based upon the combination of the *dual-time stepping technique* (Jameson 1991) and the *pseudo-compressibility method* (Chorin 1967). The basic methodology behind the developed flow method and some important features are described in Chapter 6. In Chapter 7, validations of the developed method for several well-established analytical or experimental cases are described. The validation includes one unsteady turbomachinery flow case. Then the flow method was applied to the unsteady flow simulations in Francis turbine stages with different radial gaps between the rotor and the stator. The unsteady and time-averaged numerical solutions were compared to estimate the stage loss. These results are discussed in Chapter 8.

Finally in Chapter 9, the work is concluded with some suggestions for future work.

## 2. LITERATURE SURVEY

### 2.1. Introduction

This dissertation describes the unsteady viscous flow analyses of radial stage turbomachines using CFD techniques. To set this work in context, the present literature survey is divided into roughly two parts. The first part describes basic physical aspects in turbomachinery flows. Current understanding of both steady and unsteady radial turbomachinery flows and of general blade row interaction effects especially on efficiency are described. The second part examines available numerical methods for unsteady flow analyses. The state of art in the development of the numerical methods for the blade row interaction problems is reviewed. Numerical methods for incompressible flows applied to turbomachinery are also described.

### 2.2. Centrifugal Compressors and Pumps

The complexity of the flow field in the centrifugal compressors and pumps has been well recognised with its strong fluid swirling motion associated with pressure gradient across the passages. One of the first major advances in the understanding of three-dimensional flow in the centrifugal impeller was the jet-wake flow concept introduced by Dean and Senoo (1960). This model identifies the low momentum fluid near the suction surface of the blade that is segregated from the high momentum fluid located on the pressure surface side. The significance of the jet-wake flow model lies in the recognition of the dominant roles of flow viscosity on the flow pattern observed toward the exit of the centrifugal impeller. The experimental work of Eckardt (1976), applying the laser anemometry technique for the measurement of the relative flow inside the impeller passage, substantiated the jet-wake flow structure in the centrifugal impeller. Moore (1973) investigated the mechanism of the jet-wake flow pattern in an experiment with a simple radial flow passage, and a correlation between a local stagnation of the potential flow in the passage and the wake flow generation was inferred. Krain (1988)

also performed laser anemometry measurements for a low specific speed centrifugal impeller with 30 degree backward sweep and identified low momentum fluid near the shroud surface in between the blades, which differed from the classical jet-wake flow pattern. The backward sweep in the centrifugal impeller is usually introduced to reduce the discharged absolute flow Mach number and to reduce the required diffusion in the following diffuser. In addition, the flow observation by Krain suggested that the backward sweep also modified the discharged flow pattern due to a reduced blade loading toward the impeller trailing edge.

Recent experimental work by Hathaway et al. (1992, 1993) and Chriss et al. (1996) using a low speed large scale centrifugal compressor facility revealed a more detailed insight into the flow development in the centrifugal impeller. The experiment, with a heavily instrumented impeller passage and the use of laser anemometry, enables a high-resolution flow measurement that serves as a sound physical base for analysis and an invaluable test case for numerical code validations.

A remarkable progress in understanding the physical phenomena in the last decade has been strongly promoted by the three-dimensional numerical steady flow solutions of the Navier-Stokes equations applied to centrifugal impellers. Notable works are those by Hah and Krain (1990), Casey et al. (1992), Hirsch et al. (1996). These important insights into steady impeller flow physics has been successfully applied to advanced blade design (Zangeneh et al. 1996, Goto et al. 1996, Zangeneh et al. 1999) and contributed to an appreciable performance gain.

On the other hand, the unsteady flows of centrifugal stages with diffuser vanes have been less investigated despite their wide applications to the medium or high-pressure ratio machines. This is probably due to the difficulty of the experiments at high-speed unsteady flow conditions. In fact, the majority of the experimental work for centrifugal compressor stages (Hayami 1990, Amineni et al. 1996, Rogers 1996, Tamaki et al. 1999) are mainly concerned with the time-averaged system performance using low speed measurement probes or pressure taps.

Inoue and Cumpsty (1984) studied experimentally the unsteady blade row interaction effects in centrifugal compressor stages. The geometry of the test impeller, which was representative of modern high-speed centrifugal impeller, was modified to operate at a low speed so that a time resolved unsteady measurement of the velocity

profile by the hot-wire technique was possible. The modified impeller was combined with several configurations of circular arc diffuser vanes. The experimental data revealed that a large periodic unsteadiness in the entry zone of the diffuser was attenuated very rapidly downstream of the throat of the diffuser. However, no explanation was made for this observation. Unsteady flow measurements for a transonic centrifugal compressor stage have been carried out by Yamaguchi and Nagashima (1996) using the high-speed pressure transducer mounted on the shroud wall in flat plate or double circular arc diffuser passages. Their experimental data suggested that, unlike the radial diffuser flow at low speed, the perturbation by the blade row interaction did not diminish after the throat area.

In radial flow machines, the spacing between the rotor and the stator is generally small (typically 5~10 percent of the rotor tip radius), yielding a strong potential flow effect due to blade row interaction. Takemura and Goto (1996) carried out an experimental study supported with CFD analysis with the mixing plane treatment based upon the Denton method. They found that the blockage effect of the downstream diffuser vanes was capable of changing the flow pattern at the impeller exit in a mixed-flow pump stage. The influence of the potential flow effect on the impeller-discharged flow was also investigated experimentally by Ubaldi et al. (1996) for a simplified centrifugal pump model. The phase-locked ensemble-averaged data shows a clear picture of the impeller-discharged flows perturbed by the diffuser vanes, suggesting the considerable impact of the potential flow effects.

Among very limited number of CFD applications on the blade row interaction problems in centrifugal machines, Dawes (1995) and Yamane and Nagashima (1998) have reported three-dimensional numerical flow analyses based upon the time-marching algorithm and both results showed encouraging comparisons with experimental data. The numerical solutions presented highly unsteady flow fluctuations due to blade row interaction in centrifugal compressors. However, correlations between the blade row interaction and loss generation were still unclear. For hydraulic pumps, the magnitude of unsteadiness is known to be very large. For example, Arndt et al. (1989) observed in their experiment on a hydraulic pump stage that the magnitude of the pressure fluctuation became comparable to the total pressure rise through the system. However, little applications of CFD technique on the unsteady incompressible flow can be found.

Generally, experimental observations seem to suggest the advantage of the

vaned diffuser system over the vaneless counterpart in terms of the aerodynamic efficiency (Flaxington and Swain 1999). The difference is usually attributed to the reduced passage length owing to the deflection of the streamlines and resultant reduction of the endwall boundary layer loss (Whitfield and Baines 1990). In axial flow machines, it is recognised that blade row interaction has significant influence on the stage performance. Analogous to axial compressors, some contribution from the unsteady interaction to loss generation can be expected whether it is beneficial or not. Nevertheless, there has been little work concerning unsteady loss mechanisms on centrifugal machines.

### **2.3. Radial Turbines**

Designs of radial turbines are largely based upon the experimental correlation derived from the observations of the overall performances in actual machines (Benson 1970, Watanabe et al. 1971). The methods of flow analyses that are based upon the physical conservation laws are limited.

In radial turbine flows, analogous to centrifugal impeller flows, flow patterns in the streamwise sections are characterised with strong secondary flows induced by the streamwise vortices (Baines 1996). They may result in flow non-uniformity in the rotor passage, similar to centrifugal impeller flows (Huntsman et al. 1992).

Small radial turbines for turbochargers are configured with spiral-shaped inlet volutes that generate flow swirling motions entering into turbine rotors. For relatively large radial turbines where the efficiency is an important parameter, a vaned nozzle is usually adopted in order to provide a stable flow swirl into the turbine rotors. As demonstrated experimentally by Hashemi et al. (1984), the flow in radial nozzle cascade produces the vortex and the secondary flow as in axial counterparts, and they are expected to interact with the downstream rotor blades. In contrast to centrifugal compressor/pump stages where the wake flows interact with largely two-dimensional diffuser vanes, the wake flows in radial turbines will interact with three-dimensional rotor passages that does not permit two-dimensional flow analysis. In high temperature applications, the nozzle vanes as well as the rotor blade may be configured with internal cooling provision. Consequently, the blades will become thick to accommodate internal

cooling air passages and this will contribute to the enhanced flow non-uniformity due to wake flows. The resultant blade row interaction effects may become considerable.

In the axial turbine stage, the performance of the system is influenced by the blade row interaction effect (Hodson, 1984). Although a similar trend is expected in the radial turbines, neither experimental nor numerical work was found on this issue.

## 2.4. Loss Mechanisms

For most turbomachines, efficiency is probably the most important parameter and much effort has been contributed to reduce the loss generation in the system in order to improve the efficiency. Conventionally, the sources of loss in a steady flow field in a cascade are classified into three major components: *profile loss*, *endwall loss* and *Leakage loss* (Denton 1993).

The profile loss mainly indicates a loss due to the boundary layer on the blade surfaces away from the endwall surfaces. This also includes the wake flow mixing loss after the blade trailing edge. For a blade with relatively large aspect ratio, the profile loss is usually estimated with two-dimensional assumptions. The endwall loss is basically due to the endwall boundary layers and their motion while passing through the cascade (secondary flow). The latter itself does not create loss but it has a potential to create loss through viscous diffusion. In practical situations, the distinction between the profile loss and the endwall loss components is not clear, and they usually interact with each other through the secondary flow motion. In the last decade, much effort has been devoted to analyse the secondary flow motion by the vorticity theory (Came and Marsh 1974, Glynn and Marsh 1980) or by experimental investigations (Gregory-Smith, 1982, Gregory-Smith et al. 1987). The current understanding of the secondary flow through a cascade was summarised by Sieverding (1985). The tip leakage loss arises when there is a leakage flow either over the tips of the blades or below the hub. The magnitude of the tip leakage loss can be expected to be large for radial machines given the low aspect ratio and a relatively large tip gap especially near the trailing edge. For instance, Farge et al. (1989) pointed out in the experimental study of a centrifugal impeller flow that the tip leakage flow changed not only the magnitude of the wake but also its location in the impeller passage. For unshrouded machines, the interaction between the endwall

boundary layers and the tip leakage flows becomes very strong.

Under the influence of the flow disturbances due to blade row interaction, the behaviour of the flow in the passage becomes much more complex and, consequently, the traditional loss theory under the steady assumption must be modified. For unsteady flows, the sources of loss may be classified in the similar manner as for steady cases, but the periodic disturbances are expected to alter the impact of each loss mechanism on the stage efficiency.

Behaviour of the boundary layer under periodic flow disturbances has been an active research topic both in the turbomachinery and general fluid research fields. The most simple case is the laminar boundary layer flow under a small sinusoidal flow disturbance and it has been studied by many researchers analytically and numerically (Lighthill 1954, Ackerberg 1972, Cebeci 1977). In turbomachinery flows, the flow phenomena are usually much more complicated. For instance, the boundary layers on the blade surface experience not only periodic disturbances of flow parallel to the boundary layer but also convective flow either toward or away from the blade surfaces (figure 2-1). Many researchers point out that the blade row interaction would induce the transition of boundary layers especially on the suction surface (Addison and Hodson, 1990). Valkov and Tan (1998) suggested that the unsteady flow disturbances on the boundary layer also increase loss generation through non-transitional wake-boundary layer interaction. A normal consequence is the increased loss level due to blade row interaction (Hodson, 1984, Okiishi et al. 1985). However, the transition of the boundary layer may prevent laminar separation and reduce the total loss generation (Poensgen and Gallus 1991).

Under the steady flow assumption, kinetic energy due to the flow non-uniformity generated upstream is usually considered as a direct source of loss. This is because the viscosity is the main mechanism to dissipate (irreversibly) the flow non-uniformity to a uniform state. With a presence of downstream blade row, some portion of the kinetic energy in the flow non-uniformity may be recovered through the unsteady wake/blade interaction. This is best illustrated in the model of Smith (1966) that shows a schematic view of the wake/blade interaction (figure 2-2). In the figure, the upstream blade is fixed in space, and the downstream cascade is moving in the horizontal direction from left to right at the velocity  $U$ . The wake flow from the upstream blade moves downstream in the direction of the absolute velocity  $C$ . The downstream row chops a wake into segments and reorients them through the passage due to the non-uniform

velocity distribution in the pitchwise direction. Here, a two-dimensional wake can be considered as being contained between two vortex sheets, and the velocity difference between the centre of the wake and the main stream determines the strength of the vortices. Under the assumption of inviscid flow, Kelvin's theorem would suggest that a quantity of fluid in the wake bounded by the vortex sheets would remain constant, and so if the wake is stretched, the velocity difference between the centre of the wake and mainstream is decreased. Conversely, the velocity difference is intensified when the wake is compressed (figure 2-3).

An experimental work by Smith (1970) has shown a performance gain in both the efficiency and the pressure rise in a low-speed research compressor, by reducing blade row spacing. The blade row spacing has a direct influence on the intensity of wake-blade interaction. Therefore, if the spacing is relatively large, the wake-blade row interaction will be weakened since the intensity of the upstream wake is attenuated by viscous diffusion before reaching the downstream blade row. Conversely, if the spacing is relatively small, the interaction will be enhanced. An explanation of the link between the performance gain and the blade row spacing is put forward by Smith (1966) in the wake/blade interaction model as stated above. By the passage of upstream wakes through a blade row, the velocity difference between the centre of the wake and the mainstream is reduced before being mixed out by viscous diffusion and, consequently, the wake mixing loss is reduced (*wake recovery*).

Poensgen and Gallus (1991) reported enhanced rotor wake attenuation in the presence of downstream stator blades in their experiment with an annular cascade stage. The rate of the wake attenuation with the stator was twice as fast as that without a stator. The result indicates a strong influence of the downstream cascade on the wake attenuation and implies the significance of the wake recovery process.

A two-dimensional numerical analysis of the wake recovery process by Adamczyk (1996) for an incompressible and inviscid flow under the linear perturbation assumption demonstrated that a maximum of 70 percent of the wake mixing loss was recovered through the process. Numerical experiments by Valkov and Tan (1998) and Van Zante et al. (1997) also confirmed that most of the potential loss in the wake mixing could be recovered reversibly when the blade rows are closely located.

Streamwise vortices generated in a blade row are convected through



downstream blade rows in a similar manner with the wake flows. Nevertheless, the contribution of the streamwise vortices to the system performance is quite opposite to the wake interaction. Kelvin's theorem suggests that a streamwise vortex will intensify the secondary kinetic energy proportionally to the stretching squared (Denton 1993). Through subsequent viscous dissipation, the secondary kinetic energy will be converted to loss that has detrimental effect on the performance.

Another important source of unsteadiness in blade row interaction is the potential flow effect from downstream rows. However its direct impact on the flow field and the loss generation in adjacent blade rows has still not been fully investigated.

## 2.5. Numerical Methods for Blade Row Interaction Problems

### 2.5.1. Basic parameters for blade row interaction

For unsteady flow analyses, it is usually convenient to look at the flow phenomena in terms of the *reduced frequency* that is defined as:

$$k = \frac{\omega L}{V_{\text{ref}}} \quad \text{eq. 2-1}$$

where  $\omega = 2\pi f$  and  $f$  (Hz) is the physical frequency of the unsteadiness.  $V_{\text{ref}}$  (m/s) is the reference velocity and  $L$  (m) is the reference length scale. For blade row interaction problems, those values are usually taken as the blade passing frequency, inlet velocity and the length of the blade chord respectively. The physical meaning of the reduced frequency is the ratio between a time scale for a fluid particle to be convected for the reference length and the time scale of unsteadiness. The scale of this parameter indicates the degree of unsteadiness. If this value is small enough, the process can be assumed to be quasi-steady.

The concept of *inter-blade phase angle* has been widely used to describe the blade flutter problems and the same concept was extended to describe the blade row interaction phenomena. In turbomachinery stages where the stationary and rotating cascades are involved, the concept of the inter-blade phase angle states that there is a constant phase difference between the neighbouring blades in the absence of the other sources of unsteadiness (e.g. vortex shedding, etc.). For example, for a single stage

turbomachine where the blade pitch angles are  $Y_{p1}$  and  $Y_{p2}$  for the first and second rows (figure 2-4), the phase difference between the upper and lower periodic boundary for the second row is (He 1996a);

$$\sigma = 2\pi \left( 1 - \frac{Y_{p2}}{Y_{p1}} \right) \quad \text{eq. 2-2}$$

The inter-blade phase angle for the first blade row is calculated by exchanging the locations of the blade pitch angles for the first and second rows in the formula. An important implication of the inter-blade phase angle is that, for the unsteady flow computations of turbomachinery stages, sufficient numbers of blade passages in each row have to be computed so that there is no phase difference between the periodic boundaries. Alternatively, phase-shifted boundary condition must be applied at periodic boundaries for computations with a single-passage domain.

### 2.5.2. Steady approach with mixing plane

The *mixing plane approach* for the flow computations of multi-stage turbomachinery is introduced as a direct extension of the steady flow approach while taking into account the blade row steady coupling effect for the purpose of predicting stage matching (Denton 1992). In this method, one representative blade passage from each row is calculated in a steady manner and the information is exchanged between the neighbouring blade rows through the mixing planes. An obvious advantage of the method is its efficiency while it is still possible to include many important features in the stage environment (e.g. downstream blockage, etc.). However, the unsteady effects on the time-averaged flow are neglected.

The mixing plane approaches assume that the mixing of the non-uniform flows occurs instantly rather than gradually through the downstream blade rows (Dawes and Denton 1999). In this process there is an implicit assumption that the loss created through the mixing plane is of the same magnitude as the loss generated through the gradual mixing which occurs in practice. Fritsch and Giles (1995) pointed out in their numerical study that the mixing plane approaches considerably overestimated the loss level in turbine stage flow computations.

The recent trend for the computations of flows in multiple blade row is to introduce the *deterministic stress* that takes into account the time-averaged unsteady blade row interaction effects without actually performing unsteady flow computations. The deterministic stress approach is based upon the concept of Adamczyk (1985), expressing the effects of blade row interaction in the stress forms in an analogy to the Reynolds stresses model of turbulent flows. A significant aspect of the concept is that, ideally, the time-averaged solutions of the turbomachinery flows in the stage configurations can be obtained by simply solving the average passage equations taking into account the blade row interaction effects. The average passage equations with the deterministic stress terms, as the Reynolds-averaged Navier-Stokes equations, do not contain sufficient information to determine the average passage solutions. Thus, the deterministic stress terms must be modelled under some assumption to close the governing equations. Despite the complexity of the modelling issue of the average passage equations, the concept attracts many researchers' attention with the recognition of the difficulty of unsteady multi-row flow computations especially in design. Some examples of numerical performance estimations for turbomachinery stages based upon the deterministic stress modelling can be found in the works by Adamczyk (1986, 1990), Hall (1997) and Rhie et al. (1998).

However, currently used deterministic stress models for the blade row interaction problems are still not practical and further research is needed. In addition, if the unsteady phenomena themselves are of interest (e.g. unsteady flow analysis, structural analysis, etc.) unsteady methods must be used.

### 2.5.3. Non-linear time-marching approach

The *non-linear time-marching method* is probably the most straightforward way to calculate unsteady flows. The solutions are marched in the physical time as it is in the physical phenomena so that, basically, there are no assumptions introduced apart from the temporal discretisation error. Theoretically, by reducing the scale of the time step, it is possible to capture all physical phenomena without modelling. Practically, the lower limit of physical time step is restricted by the computational efficiency and the unsteady flow phenomena of interest.

In general, the time-marching methods can be divided into two categories based

upon their formulation of the discretised equations in time: they are explicit and implicit formulations. The scheme based upon an explicit formulation has advantages in its simplicity and relatively small computational cost per time step. Porting to vector/parallel computers is also relatively straightforward. However, for a stable computation, the maximum time step must be restricted by the *Courant-Friedrichs-Lewy* (CFL) criterion that limits the convergence rate especially in viscous flow computations. On the other hand, the implicit time-marching formulation is not restricted by the CFL condition and the time step is more flexibly chosen. However, the computational cost per time step is usually much larger in comparison to the explicit scheme.

The first remarkable attempt to simulate the blade row interactions was performed by Erdos et al. (1977) solving 2D Euler equation by the Mac-Cormack explicit scheme. In this work, in order to deal with the problem arising from the inter-blade phase angle between the periodic boundaries, a method was proposed to store the variables at the boundaries through the whole period of the computation. The method was named the *direct store method*. Despite the simplicity of the concept and possible reduction of the computational cost, the number of applications is limited (Koya and Kotake 1985). It is because the method requires a large amount of data storage for the boundary values stored in one period. This limitation makes the method practically unacceptable for three-dimensional flow computations. It is also known that the method suffers from a slow convergence rate when an initial guess is not properly defined.

The *time-inclined method* proposed by Giles (1988) successfully avoids the problem of the large memory requirement of the direct store method. In this method, a computational time plane through the passage is inclined in the pitchwise direction so that direct connection between the upper and lower periodic boundaries can be applied. Although the method has an advantage such that no extra computer storage is required, the time-inclination angles of the computational planes are restricted to a certain pitch ratio of the rotor and the stator in the stage. Also, the method can only be applied to situations where unsteadiness of single frequency is involved. For blade row interaction problems, it is usually the case that several sources of unsteadiness are involved.

He (1990) proposed the *shape correction method*, a novel phase-shifted periodic boundary treatment. The time-dependent solutions at the periodic boundaries are Fourier-transformed to calculate components in terms of amplitudes and phase angles. The boundary values at upper and lower periodic boundaries are calculated using the Fourier

components. The method is neither restricted by the memory requirement problem nor any blade counts in the stage configurations. The method was originally applied to the blade flutter problems and is introduced to the blade row interaction problem by He (1996a). It must be pointed out that all the phase-shifted boundary treatments assume the periodic variation of flow properties at the boundaries. This implies that the method cannot be applied when there are other sources of unsteadiness (e.g. vortex shedding, boundary layer separation, etc.).

An alternative approach has been used by Rai (1985, 1987) for the computations of blade row interaction problems. The complexity of the phase-shifted boundary conditions was avoided by re-scaling the blading in order to mimic the overall cascade loading without changing the blade profile. The method predicted the time-averaged performance successfully.

In parallel to the intensive efforts to model the phase-shifted treatments, significant efforts have been made to improve the efficiency of the time accurate non-linear numerical methods. As far as unsteady viscous flow computations are concerned, efforts seem to have been concentrated on the development of the implicit scheme where the time step can be more flexibly chosen. Unsteady flow computations in stage turbomachinery based upon implicit formulations were found in the works by Rai (1985, 1987), Copenhaver et al. (1993), Yamane and Nagashima (1998).

Meanwhile, some researchers explored the possibility of efficient unsteady numerical methods based upon the efficient multi-grid concept. Jameson (1991) proposed the *dual-time stepping technique* for time accurate unsteady flow computations. The time-dependent flow governing equations discretised in an implicit form are solved in the pseudo-time domain at each physical time step and the solutions are integrated. In the pseudo-time marching process, the flow governing equations with the physical time derivative terms are integrated with an efficient multi-grid method until convergence. At the convergence in the pseudo-time domain, the pseudo-time derivative terms reduce to zero to recover the time-dependent flow governing equations. Applications of the method for turbomachinery flows are found in Arnone (1995) and He (1999).

The novel *time-consistent multi-grid method* for unsteady flow computations was introduced by He (1993) using a multi-grid concept. The original multi-grid method is not applicable to unsteady flow computations since the time accuracy is not guaranteed

with the accelerated information speed caused by the introduction of coarse grids. The basic concept of the time-consistent multi-grid method is to confine the loss of time accuracy inside a negligible scale in comparison to the time scale of physical phenomena of interest by restricting the maximum scale of the coarse grid. The effectiveness of the method is demonstrated in the works of Jung et al. (1997) and He (1999). It has been reported that, in unsteady flow computations with the time-consistent multi-grid method, the time step length enlarged by a factor of 15 in comparison to the CFL criteria gave a satisfactory time accuracy when it was compared with the experimental data (He 1993, 1999).

Despite the high computational cost of the non-linear time-marching approaches for unsteady flow computations, they will continue to receive greatest attention from fluid researchers due to its flexibility and accuracy. The solutions of the non-linear time-marching methods will also serve to provide an invaluable database for the validation of other numerical approaches.

#### 2.5.4. Time-linearised approach

The most basic assumption of the *time-linearised approach* is the linear behaviour of the unsteady flow perturbations. In this method, the governing equations are linearised about a non-linear steady solution. Small unsteady disturbances are usually assumed to vary harmonically in the physical time. For the unsteady flow computations, firstly the non-linear equations are solved to obtain a steady solution. Then the linearised equations about a steady solution are solved in the frequency domain. This time-linearised approach is efficient since the unsteady flow computation is effectively transferred to the successive steady flow computations. The method has been mainly applied to blade flutter problems, but it was also used to simulate blade row interaction problems (Adamczyk 1996).

He and Ning (1998) addressed the limitation of the linear assumption and proposed a non-linear harmonic method, which can include the non-linear effect of the unsteady disturbances. The method successfully improves the accuracy of the prediction when the non-linearity of the flow becomes obvious.

Although this method is capable of dealing with multiple sources of

unsteadiness by simply repeating the computations in different frequencies, it effectively means that computational cost increases, and the advantage over the non-linear time-marching method may become questionable. Furthermore, the linearised methods are essentially formulated based upon the linear assumptions as well as the harmonic motion of flow perturbations. When applied to actual flow computations, the limit of the methods must be carefully evaluated.

## 2.6. Incompressible Flow Methods

### 2.6.1. Pseudo-compressibility method

Since the invention of the density-based time-marching method by Moretti and Abbett (1966), it has become one of the most popular methods to solve various flow problems. Although the method was originally developed to solve transonic flow problems, the applications of the method cover subsonic and supersonic flows in the various situations with its accuracy and flexibility. The versatility of the time-marching method is due to a time-evolutionary nature of flows where the governing equations are described in the time-dependent forms. A problem arises for the incompressible flows when the flow governing equations become time-independent. The general formulation of the flow continuity equation of the compressible flow in the differential form is,

$$\frac{\partial \rho}{\partial t} + \nabla(\rho \mathbf{V}) = 0 \quad \text{eq. 2-3}$$

For incompressible flows, the density of fluid does not change in time and space so that the formulation of the continuity equation reduces to a velocity divergence free condition as,

$$\nabla \mathbf{V} = 0 \quad \text{eq. 2-4}$$

Due to the time-independent form of the continuity equation, the conventional time-marching method cannot be applied to incompressible flows as for hydraulic flows. In fact, the problems are not restricted to incompressible flows. Even for compressible fluid flows, when they are operated in a low Mach number region (typically  $M < 0.3$ ), the time-marching method suffers a severe reduction of the convergence rate or the stability of computations due to a small density change of fluid.

To alleviate the problem involved in the incompressible flow governing system, Chorin (1967) proposed a method to introduce pseudo-compressibility in the continuity equation that recovers the time-dependent form of the flow governing equations. The general definition of the sound speed  $\beta$  in fluid is,

$$\beta^2 = \frac{\partial p}{\partial \rho} \quad \text{eq. 2-5}$$

In the *pseudo-compressibility method*, an artificial speed of sound is specified rather than that being decided by the local flow variables and the modified continuity equation becomes,

$$\frac{\partial p}{\partial \tilde{t}} = -\rho \beta^2 \nabla \cdot \mathbf{V} \quad \text{eq. 2-6}$$

where  $\tilde{t}$  denotes the pseudo-time.

This modified form of the continuity equation has a time-dependent term. The method effectively modifies the continuity equation so that the flow governing equations can be integrated using the conventional time-marching algorithms. The solutions of interest here are steady, where the unphysical pressure derivative term reduces to zero to fully satisfy the velocity divergence free condition of the incompressible continuity equation. The obvious advantage of the method lies in its methodological similarity with the conventional time-marching method and it is not an arduous task for an experienced CFD developer to implement the pseudo-compressibility method in the frame of a time-marching compressible flow method. The method has found wide applications in steady incompressible flow computations (Rizzi and Eriksson 1985, Kwak et al. 1986, Walker and Dawes 1990, Farmer et al. 1994).

Due to the introduction of an unphysical pseudo-compressibility term in the continuity equation, the pseudo-compressibility method is not time-accurate and the method in its original form cannot be applied to unsteady flow computations. For time-accurate flow computations, Rogers and Kwak (1990) introduced time-derivative terms in the flow governing equations that is similar to the dual-time stepping technique. Belov et al. (1994) proposed a method to solve the pseudo-compressibility equations with time derivative terms based upon a multi-grid algorithm for unsteady incompressible inviscid flows with a free surface.



### 2.6.2. Preconditioning method

Any fluid substances have finite density change. Therefore, theoretically, the time-marching method can be applied to any fluid problems. However, in practice, the method loses its effectiveness with “incompressible flow” for mainly two reasons. These are the increased restriction of the CFL criteria and reflections of the long wavelength errors at the inlet and exit boundaries at low Mach number conditions. Both problems arise from the disparity of speeds between the convective and acoustical waves.

The *preconditioning method* was introduced to ease these problems (Turkel 1987). The method preconditions the flow governing equations and prescribes an artificial acoustic speed that minimises the gap in between various wave speeds. The method can be considered as a generalised form of the pseudo-compressibility method for flows with Mach number ranges from a low speed to a supersonic. In this method, the preconditioned equations are marched until a steady convergent state when the artificially prescribed terms in the flow governing equations reduce to zero to satisfy the steady flow governing equations. The applications of the method for compressible flows can be found in Choi and Merkle (1993), Weiss and Smith (1995).

### 2.6.3. Pressure correction method

The *pressure-based method* complements the time-marching method as a major family of CFD methods. The original concept of the pressure-based method was proposed by Harlow and Welch (1965) for a time-dependent free-surface problem. Since then, the idea of the pressure-based method has found a wide variety of applications for solving incompressible flow problems. A notable example based upon this concept is *pressure correction method* for the steady parabolic flows by Patankar and Spalding (1972).

In the time-dependent pressure correction method, the equations are solved in time in the same way as the time-marching method,

$$\frac{\rho u^* - \rho u^n}{\Delta t} = -\nabla \cdot (\rho u \otimes u)^n - \nabla p^* + \nabla \cdot \tau^n \quad \text{eq. 2-7}$$

where  $\rho \mathbf{u}^*$  is the intermediate momentum field given from an assumed pressure field  $p^*$ . In general  $\rho \mathbf{u}^*$  will not satisfy the continuity equation. Hence, the final pressure and velocity distributions will be given by introducing the corrections to those intermediate distributions as,

$$\bar{\mathbf{u}}^{n+1} = \bar{\mathbf{u}}^* + \bar{\mathbf{u}}' \quad \text{eq. 2-8}$$

$$p^{n+1} = p^* + p' \quad \text{eq. 2-9}$$

From the momentum and continuity equations, the correction field of the pressure is given in the Poisson equation form as,

$$\Delta p' = \frac{1}{\Delta t} \rho \bar{\nabla} \cdot \bar{\mathbf{u}}^* \quad \text{eq. 2-10}$$

To complete the governing system, the corrections for the momentum and pressure are sought by solving this Poisson equation in terms of the pressure correction.

The advantage of the method is that it is directly applicable to unsteady flows by accurately solving the pressure Poisson equation at each time step. However, because of the elliptic nature of the Poisson equation, the convergence of the solution is usually very slow (Shyy et al. 1992). As a result, computational cost is mainly for solving the pressure correction equation. Although the method is originally developed for incompressible flow computations, it is also applicable to the compressible flow by allowing the density variation of the fluid (Issa and Lockwood 1977).

## 2.7. Concluding Remarks

Detailed experimental data as well as steady numerical solutions are gradually disclosing the mechanisms of the flow development in radial turbomachinery flows. Common features observed are that the flow patterns in streamwise sections are determined by the streamwise vortices, which is essentially of a three-dimensional nature. Consequently, only fully three-dimensional methods will provide realistic solutions of the flows in radial turbomachines.

In order to achieve higher efficiency, a radial rotor is combined with a row of stators in middle and large-scale radial turbomachines. Relatively close proximity of blade rows and highly non-uniform flows usually introduce strong blade row interaction for these machines. Recent active research on the blade row interaction effects is confined to axial flow situations, and little has been reported for radial flow machines.

Among various numerical methods used for blade row interaction problems, non-linear time-marching method is the most physically solid approach for basic flow analysis in unsteady environments. The density-based time-marching method is widely used for the unsteady flow computations with blade row interaction. Mach number range of the density-based time-marching method is limited to high-speeds and, accordingly, little has been reported for flow analysis of the blade row interaction problems in hydraulic machines where flows are essentially incompressible.

## 3. BASELINE NUMERICAL METHOD FOR COMPRESSIBLE FLOWS

The aim of the current research is the evaluation of the loss generation due to blade row interaction. For the analysis of phenomena, the prime interest is in the unsteady flow responses to the disturbances. Detailed flow observations require time-dependent unsteady flow computations with minimal approximations or modelling of flow phenomena. For this purpose, the non-linear Navier-Stokes equations are adopted. In this chapter, the base-line method for the analysis of compressible flow models is described.

### 3.1. Governing Equations

The baseline numerical method used in this study was the non-linear time-marching flow method developed for the computations of unsteady, compressible, multi-stage, multi-passage, turbomachinery flows (He 1996c). The numerical method solves three-dimensional, time-dependent, thin-layer Navier-Stokes equations defined in absolute cylindrical co-ordinates in the integral form. The formulation of the equations is,

$$\frac{\partial}{\partial t} \iiint_{\Delta V} U dV + \iint_{\Delta A} [Fn_x + (G - U\omega r)n_\theta + Hn_r] \cdot dA = \iiint_{\Delta V} (S_i + S_v) dV \quad \text{eq. 3-1}$$

where

$$U = \begin{pmatrix} \rho \\ \rho u \\ \rho vr \\ \rho w \\ \rho E \end{pmatrix} \quad F = \begin{pmatrix} \rho u \\ \rho uu + p \\ \rho uv \\ \rho uw \\ (\rho E + p)u \end{pmatrix} \quad G = \begin{pmatrix} \rho v \\ \rho uv \\ (\rho vv + p)r \\ \rho vw \\ (\rho E + p)v \end{pmatrix} \quad H = \begin{pmatrix} \rho w \\ \rho uw \\ \rho wvr \\ \rho ww + p \\ (\rho E + p)w \end{pmatrix} \quad S_i = \begin{pmatrix} 0 \\ 0 \\ 0 \\ -(p + \rho vv)/r \\ 0 \end{pmatrix}$$

eq. 3-2

The term  $U\omega r$  is the flux term that accounts for the movement of the blade when

the row is rotating. The effect of flow viscosity is taken into account in a body force form in  $S_v$ . In the flow governing equations, there are six variables against five equations to be solved. To close the equation system, the value of static pressure is correlated with other flow variables by equation of state as,

$$p = (\gamma - 1) \left( \rho E - \frac{1}{2} \rho (u^2 + v^2 + w^2) \right) \quad \text{eq. 3-3}$$

### 3.2. Numerical Scheme

The governing equations are discretised in the finite volume form with a cell-centre variable-storage. A structured H-type mesh is employed to form the computational domain. The fluxes over hexahedral cell are summed yielding discrete equations in the following form:

$$\frac{\partial U_{ijk}}{\partial t} \Delta V_{ijk} = R_{ijk} + D_{ijk} \quad \text{eq. 3-4}$$

where R is the flux change and D is the numerical damping term introduced for a stable computation. The subscript  $ijk$  suggests the indices of the cell concerned.

The numerical scheme in the flow method is based upon the scheme proposed by Jameson (1982) with a second order accurate four stage Runge-Kutta time integration technique. The time derivative terms in the governing equations is discretised as follows,

$$U^{n+\frac{1}{4}} = U^n - \frac{1}{4} \frac{\Delta t}{\Delta V} (R^n - D^n) \quad \text{eq. 3-5a}$$

$$U^{n+\frac{1}{3}} = U^n - \frac{1}{3} \frac{\Delta t}{\Delta V} \left( R^{n+\frac{1}{4}} - D^n \right) \quad \text{eq. 3-5b}$$

$$U^{n+\frac{1}{2}} = U^n - \frac{1}{2} \frac{\Delta t}{\Delta V} \left( R^{n+\frac{1}{3}} - D^{n+\frac{1}{3}} \right) \quad \text{eq. 3-5c}$$

$$U^{n+1} = U^n - \frac{\Delta t}{\Delta V} \left( R^{n+\frac{1}{2}} - D^{n+\frac{1}{3}} \right) \quad \text{eq. 3-5d}$$

and

$$R = \sum_{\text{faces}} (F + (G - U\omega r) + H) \cdot \Delta A - (S_i + S_v) \Delta V \quad \text{eq. 3-6}$$

The flux terms on the cell surfaces are evaluated by linear interpolation which results in the second order spatial accuracy of the scheme.

For a sharp shock capturing ability in transonic flow computations, a blend of second and fourth order numerical damping terms is introduced with a pressure sensor (Jameson 1982). The numerical damping terms in the equations are divided into the components in the three directions as,

$$D_{ijk} = \left( d_{i,j+\frac{1}{2},k} - d_{i,j-\frac{1}{2},k} \right)_x + \left( d_{i+\frac{1}{2},j,k} - d_{i-\frac{1}{2},j,k} \right)_y + \left( d_{i,j,k+\frac{1}{2}} - d_{i,j,k-\frac{1}{2}} \right)_z \quad \text{eq. 3-7}$$

and

$$\left( d_{i,j+\frac{1}{2},k} \right)_x = \left[ \epsilon_{i,j+\frac{1}{2},k}^{(2)} (U_{i,j+1,k} - U_{i,j,k}) - \epsilon_{i,j+\frac{1}{2},k}^{(4)} (U_{i,j+2,k} - 3U_{i,j+1,k} + 3U_{i,j,k} - U_{i,j-1,k}) \right] \frac{\Delta V_{i,j+1,k}}{\Delta t} \quad \text{eq. 3-8}$$

where  $\epsilon^{(2)}$  and  $\epsilon^{(4)}$  are second and fourth order smoothing coefficients that are defined as follow,

$$\epsilon_{i,j+\frac{1}{2},k}^{(2)} = \max(v_{i,j+2,k}, v_{i,j+1,k}, v_{i,j,k}, v_{i,j-1,k}) \quad \text{eq. 3-9}$$

$$v_{i,j,k} = K^{(2)} \frac{|p_{i,j+1,k} - 2p_{i,j,k} + p_{i,j-1,k}|}{|p_{i,j+1,k} + 2p_{i,j,k} + p_{i,j-1,k}|} \quad \text{eq. 3-10}$$

$$\epsilon_{i,j+\frac{1}{2},k}^{(4)} = \max \left( 0, \left( K^{(4)} - K^{(2\&4)} \epsilon_{i,j+\frac{1}{2},k}^{(2)} \right) \right) \quad \text{eq. 3-11}$$

where  $K^{(2)}$ ,  $K^{(4)}$  and  $K^{(2\&4)}$  are constants used to control the amount of numerical

dissipation. If the pressure gradient is small, the fourth order numerical damping terms come into effect for stable computations. In the vicinity of a shock-wave, where a sharp pressure gradient occurs, the fourth order damping terms are switched off and the second order damping terms suppress the oscillations around the shock.

### 3.3. Treatment of Viscous Terms

The flow viscosity is included in the form of source terms in  $S_v$  in the governing equations. To reduce the computational cost, the viscosity effects are modelled under the thin-layer assumption so that the viscous stress terms in the directions tangential to solid surfaces are included (He and Denton, 1994). Those terms  $\tau$  are transformed for the body force form as:

$$\iiint_{\Delta V} S_v dV = \iint_A T_v dA \quad \text{eq. 3-12}$$

where

$$T_v = \begin{pmatrix} 0 \\ \tau \cos(\zeta) \\ \tau \cos(\eta) \\ \tau \cos(\xi) \\ 0 \end{pmatrix} \quad \text{eq. 3-13}$$

and  $\zeta$ ,  $\eta$  and  $\xi$  are angles between the velocity and the  $x$ ,  $\theta$  and  $r$  directions, respectively. The shear stresses were calculated with a standard Baldwin-Lomax mixing length model with the thin-layer approximation.

### 3.4. Time-Consistent Multi-Grid Technique

The efficiency of computations is significantly improved by the time-consistent multi-grid method (He 1996b) adopted in the flow method. The basic concept of the method is the same as that of the two-grid method (He 1993). In the two-grid method, the basic fine grid and an overlaid coarser grid are defined on the computational domain.

Quantities on the fine grid are updated by the flux contributions from both the fine grid and the coarse grid, whilst the time step is dictated by the CFL criteria defined on the coarse mesh scale. The time-consistent multi-grid method introduces intermediate meshes between the fine and coarse mesh in order to improve time accuracy. The form of the resultant method is,

$$\frac{\Delta U_f}{\Delta t_c} = \frac{L_f}{L_c} \frac{R_f}{\Delta V_f} + \sum^M \frac{L_m}{L_c} \frac{R_m}{\Delta V_c} + \left( 1 - \frac{L_f}{L_c} - \sum^M \frac{L_m}{L_c} \right) \frac{R_c}{\Delta V_c} \quad \text{eq. 3-14}$$

where  $M$  denotes the level of the intermediate grids and  $L$  is the minimum length scale of a particular grid. The subscripts  $f$ ,  $m$  and  $c$  denote the fine, intermediate and coarse grid respectively.

With an introduction of the coarse grid, the time accuracy on the fine mesh is no longer guaranteed. However, the loss of time accuracy is expected to be negligible provided that the coarse grid scale is much smaller than the typical length scale of the unsteadiness of the blade row interaction.

### 3.5. Boundary Conditions

The boundary conditions must be applied through the course of the computations at the inlet and the exit boundaries. At the inlet boundary, total pressure, total temperature and two flow angles are specified while static pressure is fixed at the exit boundary to control the mass flow rate. Other undefined flow variables at the boundaries are extrapolated from the interior of the domain.

Non-physical reflections from the inlet and exit boundaries are not desirable: therefore a simplified one-dimensional non-reflecting boundary treatment (Giles 1990) is applied at both those boundaries. This boundary condition makes it possible to reduce the length of the inlet and exit computational domains and is therefore advantageous in terms of the computational cost.

If the no-slip wall boundary condition for viscous computations is specified, the mesh must be highly refined near the wall surfaces in order to resolve the thin viscous layers. An additional computational cost due to the mesh refinement near the wall surface



is not desirable, especially for computationally intensive unsteady flow simulations. Therefore, fluids at the solid boundary are allowed to slip and the wall shear stresses are computed using either the laminar frictional law or an approximate log-law model of Denton (1992), depending on the Reynolds numbers calculated on the first grid points from the walls. They are defined as,

$$\tau_w = \frac{1}{2} c_f \rho_w W_w^2 \quad \text{eq. 3-15}$$

$$c_f = \begin{cases} \frac{2}{\text{Re}_w} & : \text{Re}_w < 125 \\ -0.001767 + \frac{0.03177}{\ln(\text{Re}_w)} + \frac{0.25614}{(\ln(\text{Re}_w))^2} & : \text{Re}_w \geq 125 \end{cases} \quad \text{eq. 3-16}$$

$$\text{Re}_w = \frac{\rho_w W_w \Delta y_w}{\mu} \quad \text{eq. 3-17}$$

where  $W$  is the relative velocity and  $\Delta y$  is the distance from the wall. The subscript  $w$  denotes the first grid points away from the wall surface.

In the current flow method, the effect of the tip clearance flow is implemented by simply applying the periodic boundary treatment between the adjacent blade rows inside the tip gap. Chima (1996) conducted a numerical experiment to evaluate the accuracy of this simple tip clearance model by comparing it to a more sophisticated tip clearance model with multi-block flow method. It was concluded that the numerical flow solution with this simple tip clearance model gave a good agreement with the solution from the multi-block flow method. A similar observation was also ascertained by Hathaway and Wood (1996) for a low-speed centrifugal impeller with a numerical experiment.

### 3.6. Sliding Boundary Treatment between Blade Rows

For unsteady flow computations of stage configurations with a relative movement between blade rows, a smooth information exchange is required between the moving and stationary meshes attached to either rotor or stator blades. For the purpose of

the information exchange, a sliding patched grid approach is used.

The current flow method employs phantom cells to handle the boundary treatment, therefore, the information exchange at the sliding interface is operated in a similar manner (figure 3-1). At the sliding interface, a phantom cell from one frame (point "a" from frame 1) overlaps the real cells on the other frame. The values in the phantom cell are calculated by a linear interpolation on the real cells (points "A" and "B" from frame 2). This interface treatment has a second order spatial accuracy that is consistent with the discretisation scheme of the flow method. Although this approach does not guarantee flux conservation at the interface, the error in the mass conservation was found to be negligible.

### **3.7. Parallel Computing**

In the current research, flow simulations have been conducted mainly on a SGI Power Challenge with 16 R10000 processors. To take full advantages of the computational environment, the TF3D flow method was adapted for parallel computing supported by the SGI compiler. First, the possibility of parallel computing was sought through the course of development of the new incompressible flow method TF3D-M0 as described in Chapter 6. Then it was transferred to the TF3D flow method. Some data of the performance gain through parallel computing will be presented in Chapter 6.

## 4. VALIDATION OF THE COMPRESSIBLE FLOW METHOD

### 4.1. Introduction

In general, flows in centrifugal compressors present quite different structures compared with axial flow counterparts. Strong pressure gradients associated with meridional and tangential bends and the radial flow passage are primarily responsible for those differences. In addition, for high speed centrifugal compressors, a large increase in the density due to the high pressure rise along the impeller passage necessitates the meridional flow area to decrease, and that reduces the blade height even further to accommodate the same mass flow. As a result, the relative thickness of wall shear layers compared with the blade heights becomes large toward the trailing edges of centrifugal impellers. Consequently, the discharged flows from centrifugal impellers are quite different with those obtained by the potential flow theory. This is quite a contrast with axial compressors where the viscous effect is usually confined to a region near the surfaces of the walls or to the inside of the blade wakes.

The flow method introduced in the previous chapter was originally designed and validated only for axial turbomachines. Therefore, it must be validated for centrifugal compressor flows. For this purpose, a steady centrifugal impeller flow where extensive experimental data were available was calculated to address the applicability of the numerical method in the centrifugal flow environments.

### 4.2. Krain's Centrifugal Impeller

The test centrifugal impeller designed by Krain (1984) was used for the validation, which has 24 full blades with 30-degree backward sweep followed by a constant area vaneless diffuser (figure 4-1). At the design point, the impeller accommodates a mass flow rate of 4.0 kg/s. Maximum total pressure is about 4.5, non-

dimensionalised by the atmospheric pressure. Basic dimensions of the centrifugal impeller are given in table 4-1. The tip clearance is 0.5 mm at the leading edge and 0.2 mm at the trailing edge, which corresponds to about 0.6 % and 1.6 % of the blade heights respectively. The experimental measurements were carried out for this impeller by Krain (1988) at six sections through the impeller passage perpendicular to the shroud wall at 0, 20, 40, 60, 80 and 100 % chordwise positions from the leading edge. At each measurement plane, the meridional velocity and the flow angles were measured using the Laser-2-Focus (L2F) velocimeter at five spanwise positions from the casing to the hub at 10, 30, 50, 70 and 90% of the span.

<b>Impeller</b>		
Inlet blade diameter at tip	=	133.15 mm
Inlet blade diameter at hub	=	43.72 mm
Outlet diameter	=	400.00 mm
Number of blades	=	24
<b>Operating conditions (at design)</b>		
Rotational speed	=	22360 rpm
Mass flow rate	=	4.08 kg/s
Total pressure ratio	=	4.5

Table 4-1 Basic parameters of Krain's centrifugal impeller

### 4.3. Numerical Conditions

Krain's impeller combined with a vaneless diffuser was calculated and the solution was compared with the experimental data. For the steady flow calculation, a computational mesh with 126945 grid points in total (mesh F: 35x93x39 in the pitchwise, streamwise and spanwise directions, respectively) was used (figure 4-2). The tip gap height was taken at a constant ratio of 1.0 percent of the blade height through the impeller blade passage and four grid points were allocated across the tip gap. Through the impeller passage, streamwise sections in the computational mesh were carefully

arranged to correspond to the measurement sections in the experiment in order to avoid three-dimensional interpolations. Flow calculations with a relatively coarse mesh with 67425 grid points in total (mesh C: 25x93x29, figure 4-3) were also conducted to observe the mesh dependency of the solutions. Two grid points were allocated in the tip gap for mesh C. For the comparison of the flow field at the design point, predicted mass flow rates for both meshes were carefully controlled to ensure a maximum error to be less than 0.01 percent by adjusting the static pressure specified at the exit boundary. The data from the calculations were post-processed to be directly comparable to the experimental data.

#### **4.4. Performance Maps**

The calculation with mesh F was conducted at the design mass flow rate, while the calculations with mesh C were operated over 6 mass flow-rate points down to the numerical surge point.

In the flow calculations, it was found that the total pressure rise and impeller efficiency changed considerably depending on the measurement plane downstream of the impeller trailing edge due to the high loss generation rate in the vaneless diffuser. The exact measurement plane in the experiment was not known. Therefore, the computational measurement plane was taken slightly downstream from the impeller trailing edge where the total pressure ratio given by the calculation at design point corresponded to the experiment (13 percent impeller trailing edge radius away from the impeller trailing edge).

Figure 4-4 shows the total pressure ratio and figure 4-5 shows the impeller polytropic efficiency against the mass flow rate from both the experiment and the numerical data. The trend of the experiment is captured in the calculations. It must be emphasised that there is little difference observed between the solutions from mesh F and mesh C in terms of both the total pressure ratio and the impeller efficiency.

#### **4.5. Circumferentially Averaged Static Pressure**

Figure 4-6 shows the circumferentially averaged shroud static pressure

distribution against the non-dimensional meridional distance from the impeller leading edge. The predicted static pressure distribution is in good agreement with the experimental data inside the blade passage. In the calculation, a local drop in the pressure rise is observed immediately downstream from the impeller trailing edge while the experimental data in that section were not available. This observation in the numerical data is attributed to the flow separation on the shroud surface (figure 4-7).

## 4.6. Streamwise Measurement Sections

Comparisons between the numerical and the experimental meridional flow velocity and pitchwise flow angle contours (figure 4-8 and figure 4-9) were carried out at six measurement sections from the inlet to the exit of the centrifugal impeller. The comparison was made simultaneously considering the secondary vectors, the static pressure and the loss distributions (figure 4-10, figure 4-11 and figure 4-12) following the flow development through the impeller passage. The secondary vector in the current study was defined as the flow velocity components that are not aligned with streamwise computational grid lines. The meridional flow velocity profiles through the impeller passage both from the numerical and experimental data are also shown in figure 4-13.

### 4.6.1. At inlet

From the experimental data (figure 4-8a, figure 4-13a), the meridional flow velocity has a positive gradient from the pressure surface toward the suction surface that is consistent with the inviscid flow theory (Eckardt 1976). The numerical results present a similar distribution. The predicted pitchwise flow angle captures the trend of the experiment (figure 4-9a). The spanwise circumferential flow velocity distribution due to the radius change generates the spanwise flow angle distribution, which is more apparent near the shroud. The flow angle variation in the pitchwise direction is mainly attributed to the increasing blade thickness at the blade leading edge. A noticeable scale of vortices is already generated near the endwall surface in the secondary velocity vectors (figure 4-10a).

#### 4.6.2. 20% chord section

The distribution of the meridional flow velocity (figure 4-8b) and the pitchwise flow angle (figure 4-9b) in the experiment is correctly reproduced in the calculations. The meridional flow velocity distribution shows that the viscous effects are apparent only near the solid surfaces. The numerical solution seems to capture a low momentum fluid region on the shroud surface, although it is not clear in the experiment.

The secondary flow vectors (figure 4-10b) show that a vortex is formed on both blade surfaces. The origin of the vortices can be explained by looking at the impeller passage from a rotating frame at the same speed as the impeller shaft rotation. Here, the flow in the impeller passage experiences the coriolis acceleration force due to the shaft rotation and the centrifugal force due to meridional curvature both directed toward the hub and are balanced with the static pressure gradient in the spanwise direction. Inside the blade surface boundary layers, the low momentum fluid will be convected according to the spanwise pressure gradient (figure 4-11b) and the resulting motion leads to a formation of the vortex near the blade surfaces. Similarly, the formation of endwall vortices is expected due to the coriolis acceleration force ( $2\omega W$ ) and the blade loading effect, although it is not apparent at this section (figure 4-10b). This will become clearer in the downstream sections with an increase of the relative tangential velocity component of the flow.

#### 4.6.3. 40% chord section

The core of the low momentum fluid is gradually developing in the mid-pitch region on the shroud surface, which is driven to the centre of the flow passage by the tip leakage flow (figure 4-10c). The flow at the centre of the passage is gradually deflected toward the pressure surface by the vortices generated on the endwall surfaces. The secondary velocity vector distribution (4-10c) presents a flow field that is quite similar to the flow model by Güllich (1999), which superimposes the vortices formed on the blade surfaces and on the endwall surfaces (figure 4-14). As in the model, a pair of streamwise vortices is produced at the shroud/pressure surface corner and at the hub/suction surface corner in the numerical solution.

#### 4.6.4. 60% chord section

Toward downstream in the impeller passage, the blade height shortens significantly. The relative thickness of the low momentum fluid region therefore increases and it covers about half the span at this section (figure 4-12d and figure 4-13d). With the increase of the velocity component in the radial direction, the influence of the coriolis acceleration gradually dominates the secondary flow motion (figure 4-10d).

The vortex at the pressure/shroud surface corner is developing over a wider area while the vortex at the opposite corner is reducing in scale. The static pressure distribution shows a larger pressure gradient near the shroud surface compared to the hub surface (figure 4-11d). At the same time, the low momentum fluid region on the shroud surface does not possess sufficient radial velocity component and coriolis force to resist the higher pressure gradient. Consequently, the vortex on the shroud surface is stronger than that on the hub surface.

The core of the low momentum fluid (figure 4-8d, figure 4-12d) was found at the merging point of the tip clearance flow and the secondary flow driven by the endwall vortex (figure 4-10d). This flow pattern will also be observed in the downstream sections.

The comparison between the numerical results and the experimental data is good.

#### 4.6.5. 80% chord section

At this section, viscous effects dominate the entire flow passage. In the secondary velocity vector map, the vortex at the shroud/pressure surface corner is developed to cover the entire flow field, and the vortex in the opposite corner is further reduced in scale and is driven to the corner. The tip leakage vortex is seen on the suction/shroud surface corner.

Similar to the 60% chord section, the core of the low momentum fluid (figure 4-8e, figure 4-12e) locates at the merging point of the tip leakage flow and the secondary flow driven by the endwall vortex (figure 4-10e). This implies that a correct prediction of the location of the low momentum fluid requires a correct tip leakage flow prediction.



The numerical results continue to show a good agreement with the experimental data.

#### 4.6.6. Exit sections

The secondary flow vector map in the exit section (figure 4-10f) presents quite a different flow pattern from the 80% chord section (figure 4-10e). A strong streamwise vortex present in the 80% chord section diminishes in this section. The backward sweep can be expected to cause this effect. The flow curvature produces the centrifugal acceleration from the pressure to suction surfaces that effectively cancels the effect of the coriolis force in the blade to blade surface. The numerical results show a fair agreement with the experiment.

### 4.7. Mesh Dependency

In order to examine the mesh dependency of the solutions, the calculations were carried out with two meshes with different mesh densities in the spanwise and pitchwise directions. One of the key aspects to be compared is the location of the low momentum flow that is determined by a delicate balance between the streamwise vortices and the tip clearance flow.

Figure 4-15 shows the comparison of the meridional flow velocity profiles between the solutions from mesh F and mesh C at 40 %, 60%, 80% and 100% chord sections. The results do not show marked differences, suggesting that the grid-convergent solution was almost obtained even with the coarse mesh C. Other flow variables at different chord sections were also compared and showed little differences between the results from the two meshes.

### 4.8. Effect of Tip Clearance Flow

The tip clearance flow is one of the most important phenomena in turbomachinery flows that may influence the pressure rise, flow range, and efficiency of

the system. For unshrouded centrifugal impellers, the tip clearance flow is known to have a great impact not only on the performance with associated tip leakage losses but also the flow structures through the impeller passage as suggested by Farge et al. (1989).

In order to evaluate the tip clearance effects on this centrifugal impeller flow, numerical simulations without implementing tip clearance model and with an increased tip gap (3% of the blade height) were also conducted. The comparisons of the solutions were carried out at the design mass flow rate.

The meridional flow velocity profiles are compared among the numerical results with 0%, 1% and 3% of tip gaps at 60%, 80% and 100% chord sections in figure 4-16. The velocity profiles without tip gap suggest that the minimum velocity near the shroud locates closer to the blade suction surface when it is compared with the case with 1% tip gap, which is the closest to the experimental condition (0.6~1.6%). The difference is attributed to the effect of the tip clearance flow that carries the low momentum fluid at the shroud/suction corner toward the centre of the passage. This is clearly seen in the secondary flow vectors where the counter-clockwise vortex on the shroud/suction surface has a much smaller scale compared to the one with the tip clearance flow effect (figure 4-17). It is interesting to notice that the meridional flow velocity profiles seem to be better reproduced with 3% tip gap case compared to 1% tip gap case. Although the simple tip clearance flow model adopted in the flow method improved the prediction considerably, the results seem to suggest a prospect of further improvement in the flow prediction if a more sophisticated tip clearance model is used.

#### **4.9. Summary**

A series of steady centrifugal impeller flow calculations for validation purposes was carried out with the compressible turbomachinery flow method TF3D, and those results were examined.

The comparison of the total pressure ratio and the polytropic efficiency distributions showed that the numerical prediction captured the qualitative trend of the experimental data.

The numerical solution was clearly able to capture the development of the low

momentum fluid region on the shroud wall in the centrifugal impeller. The comparison of the meridional flow velocity and the pitchwise flow angle distributions also showed satisfactory agreement between the numerical and experimental data.

The mesh density dependency of the centrifugal impeller flow was examined by comparing the numerical solutions from two meshes with different grid densities. The calculated performances were compared at the design mass flow condition and little difference was observed. The comparison of the meridional flow velocity profiles showed little difference, suggesting the grid-convergent solution was almost obtained with coarse mesh.

The tip clearance flow proved to have a predominant influence on the flow pattern near the shroud wall surface, where the low momentum flow was under a delicate balance between the streamwise vortex motion and the tip clearance flow.

The comparison of the data and the inspections of the details of the flow field in the impeller passage gave confidence in the flow method to carry out the flow simulations of radial turbomachines.

# 5. ANALYSIS OF HIGH SPEED CENTRIFUGAL COMPRESSOR STAGES

## 5.1. Introduction

In the design of axial compressor stages, there are several motivations to reduce the gap between the blade rows. Firstly, reducing the gap will contribute to a reduction of the length and the weight of the compressors. Secondly, it has been reported that the performance of the axial compressors increases with smaller gap due to the unsteady wake recovery (e.g. Adameczyk 1996).

A similar design concept may be considered for centrifugal compressor stages. This will be more important for aero-engine applications since the blade row spacing is directly related to the dimension of the systems. Larger engine dimensions will increase the profile drag. However, the wake recovery argument needs to be justified carefully since there are also several loss mechanisms associated with blade row interaction that are detrimental to the performance. The difference in the configurations and the flow structures in comparison to those in axial machines may change the balance between the beneficial and detrimental loss mechanisms.

In order to investigate the effects of radial gap and blade row interaction on the performances of centrifugal compressor stages, Krain's centrifugal impeller was combined with radial diffusers with different radial gaps, and unsteady flow simulations were carried out using the time-marching flow method described in Chapter 3 and 4.

## 5.2. Centrifugal Compressor Flows with Blade Row Interaction

### 5.2.1. Stage configurations

To configure the test centrifugal compressor stages, Krain's impeller was combined with a generic double circular arc (DCA) diffuser. The numerical simulations

were carried out with three settings of radial gap: 5%, 10% and 15% of the impeller trailing edge radius and will be denoted in the following sections as 5%, 10% and 15% gap cases, respectively. Meridional endwall contours of the vaneless and vaned diffuser parts were of a constant area diffuser to yield a similar level of the relative flow velocity at the diffuser vane leading edge for all the configurations. The blade profile was scaled to keep a constant solidity of 1.0 and the diffuser inlet angle was kept at 71.8 degrees for all the configurations. The number of diffuser vanes was chosen to be 24, which was the same as the number of impeller blades.

### 5.2.2. Numerical conditions

Unsteady flow calculations were conducted with an impeller and a diffuser flow passage. The number of time steps in one blade passing period was 200, corresponding to a time step 8 times larger than that limited by the CFL criteria defined in the finest mesh. The non-reflective boundary treatment option was applied at the inlet and exit boundaries. In the numerical flow simulations, the tip clearance flow was not implemented so that the core of the wake flow would locate closer to the blade suction surface as it is seen in a typical centrifugal impeller flow (figure 4-16).

With the current loss prediction ability by the three dimensional numerical methods, it is difficult to obtain mesh independent solutions in terms of the absolute value of efficiency especially in computationally intensive unsteady flow simulations. However, as long as the flow field is correctly reproduced in the numerical simulations, the qualitative trend in the actual flows should be predicted. Therefore, the current numerical experiments were conducted with meshes of different densities to seek a consistent mesh-independent trend. The efficiency was calculated based upon the mass-flow-averaged and time-averaged total temperature and total pressure measured at the exit boundary of the computational domain located at a constant radius.

Two sets of meshes with different grid densities in streamwise sections were used for each radial gap configuration. The fine meshes (mesh F) had 35 and 41 grid points while the coarse meshes (mesh C) had 29 and 25 grid points in the pitchwise and spanwise directions respectively. For blade row interaction problems, the most intensive unsteady flow was expected in the vaneless space between the impeller blades and the diffuser vanes so that the grid was fairly refined in the streamwise direction in the

vaneless space. On the other hand, grid spacings downstream of the diffuser vanes were stretched in order to reduce the computational cost. As a result, the numbers of grid points in the streamwise direction were different for each radial gap case (140, 146, 151 grid points for 5%, 10% and 15% gap cases respectively). Total numbers of grid points are shown in table 5-1.

A three-dimensional view of the geometry of the centrifugal compressor stage is shown in figure 5-1. In the following, the results presented are from the fine meshes, unless otherwise stated.

	<b>Mesh density</b>	<b>Total grid points</b>	<b>Impeller frame</b>	<b>Diffuser frame</b>
C - 5% gap	coarse	101500	29x77x25	29x63x25
C - 10% gap	coarse	105850	29x77x25	29x69x25
C - 15% gap	coarse	109475	29x77x25	29x74x25
F - 5% gap	fine	200900	35x77x41	35x63x41
F - 10% gap	fine	209510	35x77x41	35x69x41
F - 15% gap	fine	216685	35x77x41	35x74x41

Table 5-1 Computational meshes for the compressor systems

### 5.2.3. Stage performance

Numerical simulations with different radial gaps were carried out at the same static pressure as an exit boundary condition. Under this condition, the mass flow rate was found to vary depending on the radial gaps (table 5-2): the mass flow reduced with increasing radial gap. The difference was probably attributed to slightly different diffuser vane loadings that influenced the static pressure recovery. The maximum difference in the mass flow rates was about 3 percent among the stage solutions with mesh F.

For the calculations with mesh F, the exit static pressure was controlled to achieve the same mass flow rate, in an attempt to ensure the same work input by the impeller blade to the fluid among different radial gap configurations. In this case, the difference in the mass flow rate of less than 0.5 percent was obtained and those results

are also shown in table 5-2.

	Mass flow rate [kg/s]	Total pressure ratio	Isentropic Efficiency
C-5% gap	4.28	4.31	0.859
C-10% gap	4.22	4.32	0.862
C-15% gap	4.16	4.36	0.863
F-5% gap	4.24	4.29	0.851
F-10% gap	4.18	4.30	0.855
F-15% gap	4.12	4.33	0.857
F-5% gap (adjusted mass flow)	4.10	4.36	0.851
F-10% gap (adjusted mass flow)	4.11	4.34	0.856
F-15% gap (adjusted mass flow)	4.12	4.33	0.857

Table 5-2 Performances of the stage compressors

The trends of the time-averaged isentropic efficiency against the radial gaps are compared in figure 5-2 for all the flow conditions. The calculations from mesh C predicted higher efficiency compared to those from mesh F. The difference appears probably because the coarse mesh C did not have sufficient spatial resolution near the wall to resolve the viscous shear layers that contributed to the loss. Nevertheless, the results present a consistent trend where the maximum efficiency is achieved with the largest radial gap, and the efficiency reduces with the reduction of the radial gap. It is significant to note that this observation is in contradiction to those for axial turbomachines where a smaller gap between blade rows usually benefits the efficiency because of the wake recovery process.

Figure 5-3 shows the mass-averaged and time-averaged entropy development along the compressor passage, which is plotted against the radial co-ordinate from about 85% to 135% of the impeller trailing edge radius. In the figure, solid triangles and squares indicate the locations of the diffuser vane leading edges and the trailing edges respectively and the values between them suggest the entropy rise through the diffuser

vane passages. It must be mentioned that the entropy is a direct indication of loss so that a higher entropy level suggests a higher loss level of a corresponding configuration. Although only one set of numerical solutions based upon mesh F at the constant mass flow rate is plotted, the results from other flow condition and mesh density showed the same trend.

In figure 5-3, the plotted lines from the left-end until the impeller trailing edge positions correspond to the impeller passages. The entropy rises in the impeller passage from different radial gaps show almost identical trend apart from the neighbourhood of the impeller trailing edge where the entropy level for the 5% gap case is slightly higher than the other two cases.

The vaneless spaces between the impeller trailing edges and the diffuser leading edges (solid triangle in figure 5-3) are characterised by a very steep entropy rise that is quite a contrast to a moderate entropy rise in the impeller passage.

The entropy rises in the diffuser passages that correspond to the sections between the diffuser leading edges and trailing edges (solid squares in figure 5-3) turn out to be substantially different among different radial gaps (values in figure 5-3). The entropy rise in the diffuser vane passage seems to be the deciding factor for the stage efficiency level.

In the following sections, the causes of differences in the entropy rise among different radial gaps observed in figure 5-3 are examined by dividing a flow passage into the impeller passage, the vaneless space and the diffuser passage.

#### 5.2.4. Impeller passage

At a constant mass flow rate and a constant shaft rotation speed, the entropy development through the impeller passage will follow the same trend, provided that the flow disturbances from outside the impeller are negligible. However, some differences can be found for the 5% gap case near the impeller trailing edge where the entropy level is slightly higher than the other two cases (figure 5-3). Figure 5-4 shows the comparison of the unsteadiness of the relative flow velocity  $\bar{W}$  near the impeller exit at mid span, which is defined as



$$\bar{W} = \frac{1}{N} \sum_{n=1}^N |W^n - W_{avg}| \quad \text{eq. 5-1}$$

where  $W$  and  $W_{avg}$  are the local instantaneous and time-averaged velocities and  $N$  is the number of time steps in a blade passing period.

The distributions of the flow unsteadiness induced by blade row interaction present a similar flow pattern for all the radial gap configurations with two peaks appearing between the blades. No physical explanation has been found yet for this flow pattern. The 5% gap case shows substantially stronger flow unsteadiness compared to the other two cases. The flow unsteadiness is known to enhance the mixing of the flow non-uniformity through the deterministic stress (Adamczyk 1985) that explains the difference in the entropy rise. Since the potential flow effect diminishes relatively quickly in space, it does not seem to show a substantial influence on the entropy rise for the 10% and 15% gap cases that follow almost an identical trend (figure 5-3).

Since the wake flow mixing inside the rotor passage will reduce the benefit of the wake stretching in the vaneless space that will be discussed later, the potential flow effect is detrimental in terms of the stage efficiency.

### 5.2.5. Vaneless space

The flow velocity in the main stream relative to the endwalls becomes the highest in the vaneless space in centrifugal compressors, and it results in a rapid entropy rise due to the dissipation in the endwall boundary layers, which is observed in figure 5-3. Figure 5-5 shows the time-averaged loss ( $\exp(-\Delta s/R)$ ) contours on meridional sections at mid-pitch for three radial gap configurations. In the figure, L.E. and T.E. indicate the radial positions of the leading and trailing edges of the diffuser vanes. The comparison of the loss contours shows that the endwall boundary layers that correspond to high loss regions become substantially thicker for a configuration with a larger radial gap at the same radius compared to that for a smaller radial gap case. The results suggest the effect of the diffuser vanes to prevent the thickening of the endwall boundary layers. The diffusers are also known to prevent the detrimental flow separation (Takemura and Goto 1996).

From the consideration of the endwall boundary layers in the vaneless space, it

may appear that reducing the radial gap will benefit the efficiency since this is where a high proportion of loss is generated in the endwall boundary layers and reducing the gap is expected to reduce the loss. However, as it is seen in figure 5-2, it is not the case for the current centrifugal compressors and the reasons are explained next and in the following section.

A radial flow passage inherently involves the passage expanding in the circumferential direction. This unique feature differentiates the mechanism of the wake diffusion in the radial duct from its axial counterpart. For an axial duct flow, the viscous effect is the main mechanism to dissipate flow non-uniformity while, in radial duct, the wake stretching by the *wake inclination* will also play a role to dissipate the flow non-uniformity. If the flow with the wake is discharged from the impeller, the angle between the wake and the radial direction tends to increase toward downstream (figure 5-6 and Appendix 2). The inclination of the wake line results in a stretching of the wake segment in radial duct and the mechanism of the process is described by a simple algebraic model in Appendix 3. Consequently, the loss due to the wake flow mixing is reduced.

A stage configuration with a larger radial gap will have a more effective space for the wake stretching so that increasing the radial gap is expected to be advantageous as long as the wake inclination effect is concerned.

#### 5.2.6. Diffuser passage

As shown in figure 5-3, the entropy rise in the diffusers varies substantially among different radial gaps with the highest entropy level for the 5% radial gap and the entropy rise reduces by increasing the radial gap.

Part of the loss is attributed to the unsteady loss produced through the wake/boundary layer interaction. Figure 5-7 shows the instantaneous loss contours in the diffuser passages at the mid span section from three radial gap configurations. For the contours of 5% gap case, the disturbances on the vane surface boundary layers by the wake lines are clearly observed as thicker layers of high entropy. On the other hand, the boundary layer disturbances are not clearly seen in the 10% radial gap case and even smaller in 15% radial gap case. Figure 5-8 shows the time-averaged loss contours at the same section with figure 5-7. The suction surface boundary layer on the diffuser vane for

the 5% gap case is thicker than other cases, substantiating the loss production by the wake/boundary layer interaction.

Another contributing factor in the different entropy productions in the diffusers is the wake chopping effect. For axial machines, it is known that the wake chopping will benefit the stage performances. The wake chopping and subsequent wake stretching hypothesised by Smith (1966) occur due to different flow velocities between the suction and pressure side. Figure 5-9 shows a schematic of the mechanism of the wake stretching through a cascade. Here the angle between the suction surface of the blade and the wake segment is defined as  $\sigma$  on the downstream side. For axial flow compressors,  $\sigma$  is usually larger than 90 degrees so that the wake segment tends to be stretched as it is convected downstream (figure 5-9a). On the other hand, *wake compression* will occur when  $\sigma$  is smaller than 90 degrees as shown in figure 5-9b. For the test centrifugal compressor stages, the angle  $\sigma$  defined in a similar manner as in figure 5-10 is smaller than 90 degrees, and the compression of the wake segments occurs in the diffuser passage (figure 5-11). If the wake flow is compressed, the flow non-uniformity will be amplified to increase the mixing loss. Consequently, the wake chopping deteriorates the performance in the current centrifugal compressor stages.

### 5.2.7. Blade forces

Finally, the unsteady fluctuations of the blade forces that indicate the intensity of blade row interaction are examined. The blade forces are calculated by integrating the pressure forces in a certain direction over entire blade surfaces. The histories of the impeller blade force fluctuations acting in the tangential direction are compared among different radial gap configurations in figure 5-12a. The unsteady fluctuations due to blade row interaction reduce rapidly by increasing the radial gap. For the 5% gap case, the amplitude of the tangential force has a magnitude of more than 20 % of the total time-averaged force acting on the impeller blade.

The distributions of the fluctuating blade forces on the blade are of great interest in structural design. In the flow simulations, they were calculated by dividing the blade into 4 meridional parts and the amplitudes of fluctuating forces acting on these quarters are plotted in figure 5-12b. The first quarter corresponds to the leading edge part and fourth to the trailing edge of the impeller part. As expected, the fluctuations of forces are

disproportionally weighted toward the impeller trailing edge, confirming a limited upstream propagation of the potential flow effect.

	1 <sup>st</sup> quarter	2 <sup>nd</sup> quarter	3 <sup>rd</sup> quarter	4 <sup>th</sup> quarter
Case 5% gap	0.213-0.217 [mm]	0.217-0.221 [mm]	0.221-0.226 [mm]	0.226-0.230 [mm]
T-force	291000 [N/m <sup>2</sup> ]	18500 [N/m <sup>2</sup> ]	20600 [N/m <sup>2</sup> ]	22500 [N/m <sup>2</sup> ]
R-force	116000 [N/m <sup>2</sup> ]	82800 [N/m <sup>2</sup> ]	83300 [N/m <sup>2</sup> ]	78100 [N/m <sup>2</sup> ]
Case 10% gap	0.223-0.228 [mm]	0.228-0.232 [mm]	0.232-0.236 [mm]	0.236-0.241 [mm]
T-force	15200 [N/m <sup>2</sup> ]	9350 [N/m <sup>2</sup> ]	7950 [N/m <sup>2</sup> ]	10000 [N/m <sup>2</sup> ]
R-force	55000 [N/m <sup>2</sup> ]	40500 [N/m <sup>2</sup> ]	32300 [N/m <sup>2</sup> ]	32500 [N/m <sup>2</sup> ]
Case 15% gap	0.233-0.238 [mm]	0.238-0.243 [mm]	0.243-0.247 [mm]	0.247-0.252 [mm]
T-force	4740 [N/m <sup>2</sup> ]	3130 [N/m <sup>2</sup> ]	2200 [N/m <sup>2</sup> ]	3410 [N/m <sup>2</sup> ]
R-force	20400 [N/m <sup>2</sup> ]	13800 [N/m <sup>2</sup> ]	9010 [N/m <sup>2</sup> ]	10900 [N/m <sup>2</sup> ]

Table 5-3 Unsteady fluctuations of the forces on diffuser vane

Similarly, the force fluctuations on the diffuser vanes that are divided into four meridional parts are compared in figure 5-13 and in table 5-3. In a diffuser passage, the wake flow effects contribute largely to the blade force fluctuations. Therefore, the fluctuations diminish relatively slowly through the diffuser vane passage as the flow non-uniformity diminishes through a wake flow mixing. It was found that the amplitude of the tangential force intensifies locally at the exit quarter (figure 5-13). Although no explanation was found for this flow characteristic, it is probably due to the interaction between the wake flow and the blade surface boundary layers, which are thicker near the trailing edge of the diffuser.

It is interesting to note that, at a same radial level in different radial gap configurations (figure 5-13), the amplitude of the unsteady fluctuation is consistently higher for the cases where the radial gaps are smaller. This trend can be explained through two flow mechanisms discussed earlier. Firstly, the flow non-uniformity experiences an enhanced mixing through the vaneless space by the wake stretching effect. Secondly, once the non-uniform flow due to the impeller wake enters the diffuser

vane passage, the flow non-uniformity is amplified by the wake compression effect. Consequently, in the presence of the diffuser vane, the non-uniform flow can be conserved further downstream to increase the fluctuations of the blade forces.

### 5.3. Summary

In this chapter, a series of numerical simulations of centrifugal compressor stages with three different radial gaps has been performed in order to examine the impact of blade row interaction on the system performances.

The numerical results suggested that, if the radial gap between an impeller and a diffuser was decreased, the stage efficiency was also decreased. This trend was in contradiction to axial compressor stages where a smaller gap usually benefits the efficiency.

For axial compressors, the wake recovery by the wake chopping and subsequent wake stretching is known to play a dominant role to improve the stage efficiency through blade row interaction. On the other hand, for centrifugal compressors, the wake chopping may not be beneficial for the stage performance. The criteria for the wake recovery were expressed in terms of the angle  $\sigma$  (figure 5-10) that was defined between the blade suction surface and the wake line. If  $\sigma$  is smaller than 90 degrees at the leading edge of the diffuser vane, chopped wake segments will suffer compression near the diffuser leading edge which then increases the wake mixing loss. For many centrifugal compressors especially those with backward sweep,  $\sigma$  is likely to be less than 90 degree and, therefore, the wake-diffuser vane interaction becomes detrimental as it was in the current test compressor stages.

Due to the close proximity between the impeller and the diffuser in centrifugal compressors, a further reduction of the radial gap caused a strong flow disturbance on the diffuser vane boundary layers that increased the loss generation. A reduction of the radial gap also reduced the benefit of the wake stretching in the vaneless space.

The potential flow disturbances from the diffuser vanes increased the entropy rise near the impeller trailing edge. An enhanced mixing of the flow non-uniformity through the flow unsteadiness was expected to be responsible for this observation.

## 6. DEVELOPMENT OF AN INCOMPRESSIBLE SOLUTION METHOD

In the previous chapter, flows in centrifugal compressor stages with blade row interaction have been investigated using a non-linear time-marching method. Meanwhile it is known that blade row interaction has considerable influence on the hydraulic machines where the fluid has much higher density and higher resultant inertia forces. Unfortunately, the conventional density-based time-marching method is known to present severe problems for incompressible flows, and they are essentially not applicable for hydraulic machines as described in the introductory chapter. In this section, a method for solving unsteady incompressible viscous flows is proposed and the implementation of the proposed method is described.

### 6.1. Introduction

The most difficult and time-consuming task in the development of a new numerical flow method is in its validation. Therefore it is desirable that a new numerical method for the incompressible flow computations is developed based upon a well-established flow method. Accordingly it was decided that the baseline framework of the newly-developed incompressible flow method should be the TF3D compressible flow method presented in Chapter 3.

From this starting point, the pseudo-compressibility method (Chorin 1967) seemed to be the best choice with its solid validations by other researchers (Rizzi and Eriksson 1985, Kwak et al. 1986, Walker and Dawes 1990) and its easy implementation into the framework of the TF3D.

A problem associated with the original pseudo-compressibility method is the time-accuracy that is an essential requirement for the unsteady flow simulations. The pseudo-compressibility method in its original form is not time-accurate due to the introduction of the artificial sound wave and the pseudo-time marching process.

Physically valid solutions can be obtained only for steady state, where the pseudo-time derivative term reduces to be zero. For unsteady flow simulations, the time accuracy of the solutions must be recovered.

A clue for establishing the time accuracy with a pseudo-compressibility method was found in the dual-time stepping technique proposed by Jameson (1991). The basic idea of the method was to introduce pseudo-time derivatives in the flow governing equations in order to make use of the conventional, efficient multi-grid flow methods for the unsteady flow simulations. With this dual-time stepping technique, an unsteady flow problem reduces to effectively repetitive steady flow problems at successive discrete physical time steps. For steady flow computations, the time accuracy is not important. Therefore, the combination between the pseudo-compressibility method and the dual-time stepping technique enables the viscous incompressible unsteady flow computations.

The newly developed incompressible viscous flow method TF3D-M0 shares many features with the compressible flow methods TF3D that is presented in Chapter 3. Thus, in this chapter, some common features that were described already are omitted for brevity.

## 6.2. Governing Equations

The flow method solves the three-dimensional time-dependent incompressible thin-layer Navier-Stokes equations defined in the absolute cylindrical co-ordinate for the convenience of simulating flows in multiple blade row turbomachinery. The flow governing equations in the integral form are,

$$\frac{\partial}{\partial t} \iiint_{\Delta V} \tilde{\Theta} dV + \iint_A [Fn_x + (G - U\omega r)n_\theta + Hn_r] \cdot dA - \iiint_{\Delta V} (S_i + S_v) dV = 0 \quad \text{eq. 6-1}$$

where

$$\tilde{\Theta} = \begin{pmatrix} 0 \\ \rho u \\ \rho v \\ \rho w \end{pmatrix} F = \begin{pmatrix} \rho u \\ \rho u u + p \\ \rho u v r \\ \rho u w \end{pmatrix} G = \begin{pmatrix} \rho v \\ \rho u v \\ (\rho v v + p)r \\ \rho v w \end{pmatrix} H = \begin{pmatrix} \rho w \\ \rho u w \\ \rho v w r \\ \rho w w + p \end{pmatrix} S_i = \begin{pmatrix} 0 \\ 0 \\ 0 \\ -(p + \rho v v)/r \end{pmatrix} \quad \text{eq.6-2}$$

The source term  $S_v$  accounts for the flow viscous terms. An important difference from the original compressible flow method is that the incompressible flow governing equations do not have an energy equation that decouples from the other equations under the incompressible assumption.

### 6.3. Dual-Time Integration Scheme

The time-dependent terms in the unsteady flow governing equations are discretised in the physical time in a second order implicit form as,

$$\frac{\partial}{\partial t} \iiint_{\Delta V} \tilde{\Theta} \cdot dV = \frac{1}{2} \frac{\Delta V}{\Delta t} (3\tilde{\Theta}^{n+1} - 4\tilde{\Theta}^n + \tilde{\Theta}^{n-1}) \quad \text{eq. 6-3}$$

where superscript  $n$  denotes the discrete time level in the physical time.

In the dual-time stepping technique, the pseudo-time derivative terms of the flow variables are added in the unsteady flow governing equations and they may look like,

$$\frac{\partial}{\partial \tilde{t}} \iiint_{\Delta V} \tilde{\Theta} \cdot dV + \frac{\partial}{\partial t} \iiint_{\Delta V} \tilde{\Theta} \cdot dV + R = 0 \quad \text{eq. 6-4}$$

and

$$R = \iint_A [F n_x + (G - U \omega r) n_\theta + H n_r] \cdot dA - \iiint_{\Delta V} (S_i + S_v) dV \quad \text{eq. 6-5}$$

where the parameters  $\tilde{t}$  denotes the pseudo-time and superscript  $m$  will be used to describe their discrete pseudo-time level in the following argument.

In the equations with the dual-time domain, unsteady problems in the physical time domain can be regarded as steady problems in the pseudo-time domain with a modified form of net flux terms (second and third terms in eq. 6-4). In the dual-time stepping technique, the flow governing equations are integrated in the pseudo-time to seek a steady state, where the first pseudo-time derivative term reduces to be zero to satisfy the unsteady flow governing equations. At the steady state in the pseudo-time, the



values of  $\tilde{\Theta}$  at the next physical time level  $n+1$  are obtained. Likewise, the solutions are marched in the physical time to give unsteady solutions.

In order to solve the incompressible flow problems using time-marching method, the pseudo-compressibility was added in the continuity equation and the equation 6-4 was rewritten as,

$$\frac{\partial}{\partial \tilde{t}} \iiint_{\Delta V} \Theta \cdot dV + \frac{\partial}{\partial t} \iiint_{\Delta V} \tilde{\Theta} \cdot dV + R = 0 \quad \text{eq. 6-6}$$

and

$$\Theta = \begin{pmatrix} p/\beta^2 \\ \rho u \\ \rho v r \\ \rho w \end{pmatrix} \quad \text{eq. 6-7}$$

The term  $p/\beta^2$  accounts for the pseudo-compressibility in the modified flow governing equations. The parameter  $\beta$  stands for the specified acoustic speed. The convergence rate and stability of the method are strongly dependent on the value of  $\beta$  chosen. In the method, the value of  $\beta$  is decided by the following formula (Farmer et al. 1994):

$$\beta = c \sqrt{(u^2 + v^2 + w^2)_{\max}} \quad \text{eq. 6-8}$$

where  $c$  is a constant taking in the order of unity.

In the developed flow method, the initial values of the variables at the beginning of the pseudo-time iterations (at  $m = 0$ ) are taken directly from the previous physical time step that yield the zero order interpolation. This choice comes from the observation of the numerical experiment through the unsteady boundary layer computations where zero, first and second order extrapolation were compared in terms of the required time steps to achieve the same error level at each physical time step. It was found that the zero order extrapolation outperformed other treatments.

The flow governing equations with the modified net flux terms are integrated in the pseudo-time using the four-stage Runge-Kutta scheme. The discretised form of the equations are:

$$\Theta^{m+\frac{1}{4}} = \Theta^m - \frac{1}{4} \frac{\Delta \tilde{t}}{\Delta V} (\tilde{R}^m - D^m) \quad \text{eq. 6-9a}$$

$$\Theta^{m+\frac{1}{3}} = \Theta^m - \frac{1}{3} \frac{\Delta \tilde{t}}{\Delta V} (\tilde{R}^{m+\frac{1}{4}} - D^m) \quad \text{eq. 6-9b}$$

$$\Theta^{m+\frac{1}{2}} = \Theta^m - \frac{1}{2} \frac{\Delta \tilde{t}}{\Delta V} (\tilde{R}^{m+\frac{1}{3}} - D^{m+\frac{1}{3}}) \quad \text{eq. 6-9c}$$

$$\Theta^{m+1} = \Theta^m - \frac{\Delta \tilde{t}}{\Delta V} (\tilde{R}^{m+\frac{1}{2}} - D^{m+\frac{1}{3}}) \quad \text{eq. 6-9d}$$

where

$$\tilde{R} = \sum_{\text{sides}} (F + (G - U\omega r) + H) \cdot \Delta A - (S_i + S_v) \Delta V + \frac{1}{2\Delta t} (3\tilde{\Theta}^{n+1} - 4\tilde{\Theta}^n + \tilde{\Theta}^{n-1}) \quad \text{eq. 6-10}$$

and  $D$  is the artificial damping terms. Through the course of the pseudo-time marching computations, the convergence of the solutions is greatly accelerated by using the multi-grid technique. In the multi-grid method, redistribution of the net flux into successive coarser grid was performed in terms of the modified form of the net flux including the physical time-dependent terms. With this dual-time stepping technique, although several inner iterations are needed at every physical time step, the scale of the physical time step is not restricted by the CFL conditions.

The convergence of the pseudo-time iterations is determined by monitoring the maximum static pressure change in the computational domain. This is normalised by the dynamic head defined with a reference velocity, which is normally taken as the inlet flow velocity or the rotor peripheral speed.

$$\varepsilon = \frac{p^{m+1} - p^m}{\frac{1}{2} \rho V_{\text{ref}}^2} \quad \text{eq. 6-11}$$

In the flow method, the local iterations are continued until either the maximum allowable error level is satisfied or the iteration number reaches a certain specified number.

#### 6.4. Eigen-Value Scaled Numerical Damping

The current numerical scheme with a central difference discretisation permits the odd-even decoupling at adjacent grids that may cause oscillatory solutions. For smooth and stable computations, fourth order numerical damping terms are explicitly added in the governing equations. They are:

$$D_{ijk} = \left( d_{i,j+\frac{1}{2},k} - d_{i,j-\frac{1}{2},k} \right)_x + \left( d_{i+\frac{1}{2},j,k} - d_{i-\frac{1}{2},j,k} \right)_y + \left( d_{i,j,k+\frac{1}{2}} - d_{i,j,k-\frac{1}{2}} \right)_z \quad \text{eq. 6-12}$$

and

$$d_{i+\frac{1}{2},j,k} = -\varepsilon_i (U_{i+2,j,k} - 3U_{i+1,j,k} + 3U_{i,j,k} - U_{i-1,j,k}) \quad \text{eq. 6-13a}$$

$$d_{i,j+\frac{1}{2},k} = -\varepsilon_j (U_{i,j+2,k} - 3U_{i,j+1,k} + 3U_{i,j,k} - U_{i,j-1,k}) \quad \text{eq. 6-13b}$$

$$d_{i,j,k+\frac{1}{2}} = -\varepsilon_k (U_{i,j,k+2} - 3U_{i,j,k+1} + 3U_{i,j,k} - U_{i,j,k-1}) \quad \text{eq. 6-13c}$$

In equation 6-13, the dissipation coefficient  $\varepsilon$  is scaled in such a way that the conservation form of the system of equations is preserved (Farmer et al. 1994, Arnone 1994). The local numerical damping terms are defined with respect to the local wave speeds as,

$$\varepsilon_i = \alpha \Phi_i \lambda_i \quad \text{eq. 6-14a}$$

$$\varepsilon_j = \alpha \Phi_j \lambda_j \quad \text{eq. 6-14b}$$

$$\varepsilon_k = \alpha \Phi_k \lambda_k \quad \text{eq. 6-14c}$$

where

$$\lambda_i = |\text{SIU}| + \beta \sqrt{\text{SI}_x^2 + \text{SI}_\theta^2 + \text{SI}_r^2} \quad \text{eq. 6-15a}$$

$$\lambda_j = |\text{SJU}| + \beta \sqrt{\text{SJ}_x^2 + \text{SJ}_\theta^2 + \text{SJ}_r^2} \quad \text{eq. 6-15b}$$

$$\lambda_k = |\text{SKU}| + \beta \sqrt{\text{SK}_x^2 + \text{SK}_\theta^2 + \text{SK}_r^2} \quad \text{eq. 6-15c}$$

with

$$|\text{SIU}| = u\text{SI}_x + v\text{SI}_\theta + w\text{SI}_r \quad \text{eq. 6-16a}$$

$$|\text{SJU}| = u\text{SJ}_x + v\text{SJ}_\theta + w\text{SJ}_r \quad \text{eq. 6-16b}$$

$$|\text{SKU}| = u\text{SK}_x + v\text{SK}_\theta + w\text{SK}_r \quad \text{eq. 6-16c}$$

where the  $\text{SI}_x$ ,  $\text{SI}_\theta$  and  $\text{SI}_r$  are the directed face areas in the  $i$  direction with respect to the directions in the subscript. In equation 6-14,  $\alpha$  is used to manually control the amount of damping and the coefficients  $\Phi$  are defined as

$$\Phi_i = 1 + \left(\frac{\lambda_j}{\lambda_i}\right)^{0.4} + \left(\frac{\lambda_k}{\lambda_i}\right)^{0.4} \quad \text{eq. 6-17a}$$

$$\Phi_j = 1 + \left(\frac{\lambda_i}{\lambda_j}\right)^{0.4} + \left(\frac{\lambda_k}{\lambda_j}\right)^{0.4} \quad \text{eq. 6-17b}$$

$$\Phi_k = 1 + \left(\frac{\lambda_i}{\lambda_k}\right)^{0.4} + \left(\frac{\lambda_j}{\lambda_k}\right)^{0.4} \quad \text{eq. 6-17c}$$

Despite the cost for calculating the scaling coefficients for the numerical damping terms, the conservative nature will be beneficial in terms of the accuracy as well as the stability when the mesh aspect ratios become larger.

## 6.5. Boundary Conditions

In the developed flow method, the boundary conditions are applied using the primitive flow variables at the inlet and exit boundaries. At the inlet, total pressure and pitch and yaw angles of flow are specified while static pressure is specified at the exit boundary. For the axial exit flows as in the radial turbines, the value of the static pressure at either the hub or the casing is specified and the spanwise pressure distribution is calculated with the radial equilibrium condition. The derivation of a mathematically solid non-reflecting boundary formulation for the pseudo-compressibility equations is beyond the scope of the current research. Therefore, a conventional reflective boundary condition is applied both at the inlet and exit boundaries. This requires sufficiently long inlet and exit computational domains to avoid the harmful effect of the unphysical reflection of the waves on the final solutions.

## 6.6. Multi-Grid Solution Acceleration Techniques

For the acceleration of the convergence, the multi-grid method is the most commonly used with the explicit time-marching methods. In the current study, two types of multi-grid techniques were implemented. The first method was the multi-grid method adopted in the TF3D (He 1996), which is an extension of the conventional approach (Denton 1982) that redistributes the residuals defined in the fine grid to successive coarser grids. The second method was the non-linear multi-grid method (Hirsch 1989) where both the flow variables and the residuals are calculated in the multi-grid procedure.

The basic procedure for the non-linear multi-grid used in the flow method utilises the auxiliary coarser grids introduced by doubling the grid spacing with the flow variables and net fluxes being transferred through the following rules,

$$U_{2h}^{(0)} = \frac{\sum_{2h} \Delta V_h U_h}{\sum_{2h} \Delta V_h} \quad \text{eq. 6-18}$$

$$R_{2h} = \sum_{2h} R_h(U_h) \quad \text{eq. 6-19}$$

where the subscripts  $h$  and  $2h$  denote the grid spacing parameters for the finest and coarser grids (i.e.  $4h$ ,  $8h$  are successively coarser grids). The flow variables on the finer grids are volume-averaged to calculate the flow variables defined in the coarser grid. Then the flow variables in the coarser grid are updated with a larger time step defined at the same grid as,

$$U_{2h}^{(+)} = U_{2h}^{(0)} - \Delta t^* R_{2h} \quad \text{eq. 6-20}$$

The results on the  $U_{2h}^{(+)}$  provide the data for the next grid level and so on. Once the coarsest grid level is reached, the coarsest grid data are redistributed to the finer grids as,

$$U_h^{(++)} = U_h^{(+)} + \frac{\Delta V_h}{\Delta V_{2h}} (U_{2h}^{(+)} - U_{2h}^{(0)}) \quad \text{eq. 6-21}$$

The operations continue up to the finest grid level. This method has been utilised with the two-level multi-grid method and the local time stepping technique in order to accelerate the convergence further. The local time step are defined as,

$$\Delta t = \frac{\Delta V}{\lambda_i + \lambda_j + \lambda_k} \quad \text{eq. 6-22}$$

A series of test computations has been carried out to test the performance of the multi-grid acceleration techniques. The comparison of the efficiency of the methods was made for the linear turbine cascade case. The detail of the case is described in the following chapter. The numerical test was conducted on a two-dimensional mesh with 5355 grid points (105x51 in the streamwise and pitchwise directions) for 5000 iterations. For the non-linear multi-grid method, five-level multi-grid was used while the maximum CFL number was specified to be 40 for the original multi-grid method. The maximum and averaged residuals in the pressure are shown in figure 6-1.

Both multi-grid methods show stable reduction of residuals with marginally better convergence history from the non-linear multi-grid method toward the end of the computations. However, the convergence rate for both methods in terms of maximum error is almost the same until the order of residuals at minus three and the convergence is monitored by the maximum error in the current flow method. Although the non-linear

multi-grid seems to have an advantage in the convergence history, an additional computational cost makes the method more expensive than the original multi-grid method in terms of the total computational time (1.5~2 times). Consequently the final form of the numerical method adopted the multi-grid method utilised in the original TF3D compressible flow method.

## 6.7. Issues on Cavitation

For hydraulic machines, cavitation is an important problem since its effects are detrimental for fluid dynamic, structural and environmental performances (Kato 1998). In fact, for most hydraulic applications, the onset of cavitation itself is not acceptable because of those harmful effects. Usually the onset of cavitation is described in terms of the net positive suction head (NPSH) that is defined as,

$$\text{NPSH} = h_s - h_v \quad \text{eq. 6-23}$$

where  $h_s$  and  $h_v$  are the absolute stagnation pressure head at the pump inlet or at the turbine exit and the vapour pressure head, respectively. This parameter states the pressure margin between local pressure and vapour pressure. A higher value of NPSH reduces the likelihood of cavitation.

When the local pressure drop is more than the value given from the NPSH condition due to the acceleration of the flow, cavity bubbles start to grow. These cavity bubbles are convected downstream and collapse violently on the blade surfaces. This causes serious erosion of the material and noises. The process is highly complicated and it does not permit a simple modelling of the phenomena that are useful for practical applications. Although there are some analytical studies applied for the blade cascade (Pilipenko and Semenov 1998), assumptions made in the analysis are usually case-specific for a simplified test case. Careful judgements are then required when they are applied to flows of practical interest.

For many numerical studies of hydraulic machines, the cavitation effect is normally completely neglected (Miner et al. 1992, Qian and Arakawa 1998, Sedlar and Mensik 1999). Nevertheless, for the design of hydraulic machines, the CFD technique made a remarkable contribution to the performance gain (Drtina and Sallaberger 1999).

This is achieved by the optimization of the pressure distribution on the blade to avoid the area of excessively high relative velocity and resultant low static pressure that induces the cavitation bubbles. In the developed numerical flow method, the effects of cavitation are not taken into account. However, it is believed that the unsteady flow method will become a useful tool for predicting the onset of cavitation.

## 6.8. Parallel Computing

Recent dramatic growth of computing capability is not only due to the increasing computing power of the individual processor but also due to parallel computing. In the University of Durham, a multiple-processor server SGI Power Challenge with 16 R10000 processors has been utilised for the floating-point intensive numerical computations since 1996. To take the full advantage of the available computer resources, the numerical flow method developed was optimised for parallel computations.

The parallel programming may be realised through two different approaches. The first approach is to parallelise only certain do-loops based upon the OMP (Open Multiple Processing) standard. In this approach, the compiler splits the do-loops in the program into concurrently executing pieces thereby decreasing the computational time (not the CPU time). This approach requires additional overheads to find the multiple processes through the computations. However, the computer source code is compatible in any platform and the compiled code can run with any number of processors by simply specifying it before running. Another approach is to divide the calculation domain and allocate processors for those domains. This method requires the computer source code to be case specific and hence is less flexible. For the current research, only the first approach has been utilised to sustain the compatibility of the source code.

The source code is modified with special care to sustain the independence of the data inside the do-loops where the parallel directives are coded, such that the solutions computed with any number of processors become identical.



### Performance gain

Numerical tests were conducted in order to measure the performance advantage of the parallel computing. The test was carried out with the Durham linear turbine cascade case. The computational grid used consisted of 246330 grid points. In order to measure the pure computational time excluding the time for the initial setting as well as io-operations, measurements were made using following procedure.

Step 1 : Measure the computational time for the 10 iterations, T1

Step 2 : Measure the computational time for the 110 iterations, T2

Step 3 : Subtract T1 from T2 to obtain the computational time for 100 iterations

This test has been carried out with 1, 2, 3, 4 and 8 processors and the performance gain were measured comparing the total wall-clock run time. The results of the test are summarised in table 6-1.

The results show a disproportional increase of performance with increasing number of CPU used. This is because the parallel computations require some overheads to create multiple-threads through the course of the computations. Therefore the do-loops must contain sufficient amount of work-load that compensates for these overheads to justify the parallel computing.

For the linear turbine cascade flow computations, the performance gain by the parallel computing is reasonable, given a reasonable amount of work-load with sufficient number of grid points. For the dual-processor computation, nearly 80 percent of performance gain was obtained. With the increase of the processor number and with the decrease of the work-load allocated to each CPU, the performance gain by the parallel computing reduces significantly. The performance gain using 8 processors was less than 300 percent.

No. of CPU	110 steps	10 steps	100 steps	Time ratio	Gain	Work/CPU
1	977 [s]	116 [s]	861 [s]	1.0000	1.0000	1.0000
2	560 [s]	76 [s]	484 [s]	0.5621	1.7790	0.8895
3	418 [s]	62 [s]	356 [s]	0.4135	2.4184	0.8061
4	357 [s]	57 [s]	300 [s]	0.3484	2.8703	0.7176
8	271 [s]	49 [s]	222 [s]	0.2578	3.8790	0.4849

Table 6-1 Computational times

# 7. VALIDATION OF THE INCOMPRESSIBLE FLOW METHOD

## 7.1. Introduction

The unsteady incompressible viscous flow method described in the previous chapter was validated for several test flow cases.

The validations of the flow method were carried out to investigate two important aspects. The first is the reliability of the steady viscous turbomachinery flow solutions. In the dual-time stepping technique, unsteady flows are computed by solving successive steady flow solutions in the discretised time steps. Therefore, the validity of the steady flow solutions is an essential requirement. For the validation, a flow in a linear turbine cascade was chosen as a test case for which extensive flow measurements through the passage were performed experimentally. The complex three-dimensional secondary flow in the linear turbine provided a formidable validation for the steady flow method.

Secondly, the newly developed unsteady incompressible method that combines the dual-time stepping technique and the pseudo-compressibility method must be validated. Although a similar approach has been studied and validated by other researchers (Belov et al 1994) including the method based upon the implicit iteration scheme (Roger and Kwak 1990), the method combining the multi-grid technique and the pseudo-compressibility method for viscous turbomachinery flow computations has not been reported. For validation purposes, two unsteady cases have been investigated.

The first unsteady case was a laminar boundary layer with sinusoidal free-stream velocity fluctuation. This basic flow model has been investigated by many researchers analytically and numerically, and well-established flow solutions are available. This flow model can be considered as a simplified example of the boundary layer flow behaviour under blade row interaction, which is represented by periodic flow disturbances.

The second unsteady validation was performed for an unsteady turbomachinery flow case in a radial configuration. In this flow model, flow unsteadiness is generated through actual blade row interaction in the stage configuration. The time-averaged and instantaneous data given from the experiment were compared with the numerical solutions in order to assess the applicability of the developed flow method for actual turbomachines.

## **7.2. Durham Linear Turbine Cascade**

### **7.2.1. Linear turbine blading**

The test linear turbine cascade presents a typical geometry of a high-pressure axial flow turbine rotor blade with inlet and exit flow angles of 42.75 and -67.8 degree respectively. This high flow turning induces strong cross passage vortices in a three-dimensional manner. Extensive measurements of the secondary flow development through this linear turbine cascade have been conducted by Gregory-Smith et al. (1982, 1987) and the experimental data have been released through the ERCOFTAC workshop. The experiments were operated at the inlet free-stream velocity of 19.1 m/s with the flow velocity inside the passage reaching a maximum of about 42 m/s. The flow passage was traversed at 11 axial positions with the hot wire and the five hole probes that provided detailed information of the various flow quantities (velocity, pressure, loss, etc).

### **7.2.2. Numerical condition**

In the flow simulations of this linear turbine case, only steady solutions were of interest. The flow governing equations with pseudo-compressibility were solved only in the pseudo-time while the dual-time stepping routine was set idle. In order to realise the numerical conditions as closest possible to the experiment, the pressure difference between the inlet and exit flow boundaries were carefully adjusted by controlling the exit static pressure. The inlet velocity variation due to the boundary layer profile was implemented by specifying the total pressure variation as the inlet boundary condition.

Flow calculations were conducted on a mesh (figure 7-1) that consisted of 246330 points in total (51x105x46 in the pitchwise, streamwise and spanwise directions)

in which only half passage was included in the computational domain due to the symmetric configuration. Numerical solutions were compared with the experimental data mainly at a section that located 28 percent axial chord downstream from the trailing edge of the blade, where most detailed traverse flow data were available.

For the assessment of mesh density dependency, two other meshes with different numbers of total grid points have also been used for flow simulations with the results being compared. The number of grid points for the computational meshes utilised is listed in table 7-1.

	<b>Total grid points</b>	<b>Pitchwise direction</b>	<b>Streamwise direction</b>	<b>Spanwise direction</b>
Mesh C	62790	26	105	23
Mesh M	128520	36	105	34
Mesh F	246330	51	105	46

Table 7-1 Computational meshes

### 7.2.3. Blade static pressure distribution

Figure 7-2 shows the static pressure coefficient distribution on the blade surfaces at different spanwise positions. The pressure distribution on the blade surface given by the numerical simulation shows quite a similar distribution to the experimental data. Most importantly, the local peaks of the distributions in the aft part of the suction surface near the end wall sections, which is due to the passage of the leading edge vortex from the adjacent blade, seems to be captured correctly.

### 7.2.4. Downstream section

Figure 7-3 shows the secondary flow vectors at the downstream section from both the calculation and the experiment. A pair of counter-rotating vortices is clearly captured in the numerical solution, which is also present in the experiment. Figure 7-4 is the total pressure loss contours at the same section. Two areas of distinct loss are reproduced in the calculation, which overlap the vortex centres in the previous figure.

The magnitude of loss in the blade wake is overestimated. This is explained by the fact that the actual boundary layer on the blade surface was largely laminar (Cleak and Gregory-Smith 1992) while turbulent boundary was specified in the current flow simulations. The pitch and yaw flow angles at the same section are also compared and show good agreement with the experiment (figure 7-5, 7-6).

Figure 7-7 shows the pitchwise-averaged yaw angle distribution. The numerical solution captures the qualitative trend in the experiment.

#### 7.2.5. Mesh dependency

Figure 7-8 shows the comparison of the static pressure coefficient distributions given from the different meshes. In this figure, a comparison is made at a near wall section (6% span) where the viscous effect influences the pressure distributions and at the mid-span where the inviscid flow properties dominates. The comparison shows good agreement, with marginally better comparison for the solutions with finer meshes. In fact, the viscous effect on the suction surface pressure distribution near the endwall seems to be correctly captured even by the solution with the coarsest mesh.

Despite the relatively small grid dependence of the blade surface pressure distribution, discrepancy of the calculated loss distribution is obvious in the downstream section in figure 7-9. The solution from the coarse mesh C is smeared out at this section while mesh M is able to capture the two loss core regions clearly.

### 7.3. Unsteady Laminar Boundary Layer

#### 7.3.1. Boundary layer flow under free-stream fluctuation

This test case concerns unsteady response of a laminar boundary layer under a free-stream sinusoidal fluctuation. This flow model was originally studied analytically by Lighthill (1954). In the model problem, an unsteady motion of the incompressible laminar boundary layer is introduced by a small periodic fluctuation of the main stream flow velocity about a constant mean value as,

$$u = U_{\infty} (1 + \epsilon e^{i\omega t}) \quad \text{eq. 7-1}$$

where  $U_{\infty}$  is the mean velocity of the main stream and  $\epsilon$  and  $\omega$  are the normalised amplitude and the angular frequency of the flow fluctuation. In the analysis, the value of  $\epsilon$  is usually specified to be much smaller than unity so that linearity of the model problem is sustained. The same model problem was later studied by Ackerberg and Phillips (1972) with semi-analytical approach and then by Cebeci (1977) with numerical approach by solving the unsteady boundary layer differential equations.

#### 7.3.2. Numerical condition

Consider a laminar boundary layer on a semi-infinite flat plate. In this study, a channel flow with a length of about 4 times the half channel height was used. The difference in the flow conditions would appear as an acceleration of the main flow due to the displacement thickness of the laminar boundary layer. However, the influence of the different flow condition on the flow solution is expected to be small given the calculated displacement thickness of less than 2 percent of the channel height.

Due to symmetric geometry, only half of the channel height was used for the calculations. A two-dimensional mesh with 3300 grid points (66x50: streamwise x cross passage) was used. The mesh was refined near the wall surface so that approximately 30 grid points were allocated across the boundary layer near the channel exit.

The flow simulations were conducted at a very low speed with a time-averaged free-stream velocity of about 5.6 m/s. The Reynolds number based upon the free stream velocity and the channel length was  $2 \times 10^5$ . A periodic fluctuation of the free-stream flow

was realised by applying a sinusoidal exit static pressure fluctuation. The amplitude of the freestream velocity fluctuation was taken to be very small (about 0.53 percent of the mean velocity) to ensure a linear behaviour of the unsteady flow. The number of physical time steps in one period was specified as 50 in the calculations, which proved to be sufficient from numerical sensitivity tests. The calculations was started from an initial flow field, and well-defined periodic solutions were obtained within 3 to 5 periods (Figure 7-10).

### 7.3.3. Steady flow solutions

Firstly, a steady flow calculation with fixed boundary conditions was conducted and the result was then compared with the Blasius analytical solution. Figure 7-11 shows the comparison of the velocity profiles against the boundary layer co-ordinate and the skin-friction coefficient  $c_f$  against the non-dimensionalised streamwise co-ordinate from the leading edge. The results show that the steady laminar boundary layer is well resolved by the current flow method.

### 7.3.4. Unsteady flow solutions

Three unsteady parameters were calculated from the unsteady laminar boundary layer solution, and they were compared with the analytical solutions. The unsteady comparison is made for the phase angle between the free-stream flow fluctuation and the wall shear stress. The phase angle is plotted against the reduced frequency that is defined in this specific case as,

$$k = \frac{\omega x}{U_{\infty}} \quad \text{eq. 7-2}$$

where  $\omega$  is the angular frequency of the free-stream fluctuation,  $x$  is the distance from the inlet of the channel, and  $U_{\infty}$  is the free-stream velocity. The results are shown in figure 7-12a. The numerical result shows good agreement with the analytical solutions by Lighthill (1956) for both low and high frequency regions. The result is also compared with well-established numerical solutions by Cebeci (1977) and shows good agreement. The unsteady wall shear stress divided by the product of the Blasius wall shear and the



normalised velocity amplitude is also compared and shows good agreement (figure 7-12b).

The unsteady velocity profile across the laminar boundary layer was transformed into in-phase and out-phase components, and they are compared with semi-analytical solutions by Ackerberg and Phillips (1972) in figure 7-13 at four different reduced frequencies. The numerical solutions show excellent agreement with the semi-analytical solutions, demonstrating the validity of the developed numerical method.

### 7.3.5. Numerical parametric study

In the developed flow method, there are several numerical parameters that need to be specified for the flow calculations and that may have influences on the accuracy of the solutions as well as on the convergence. In this section, a series of numerical tests was carried out on those parameters to examine their significance.

#### Coarse grid scale in the multi-grid technique

In terms of the convergence rate of the solutions, it is preferable to specify as large a scale of coarse grid as possible since it decides the propagation speed of the information that governs the convergence rate. However, the accuracy of the solutions should not be sacrificed. In the first numerical experiment, several different scales of coarse grids were specified in the steady laminar boundary layer flow simulations and their influence on the convergence rate, and solution accuracy was examined. Table 7-2 shows the comparison of the convergence rate with respect to the differences in scales of the coarse and fine grids. For the flow calculations, the multi-grid levels were taken as many as possible inside the coarsest grids and the calculations were terminated either when the maximum residual became smaller than 0.0001 percent or when the time steps reached 5000. For this test, a maximum coarse grid ratio of up to 1000 was tested, which was larger than the quarter of the channel height. As expected, the larger scale of the coarse grid tended to give better convergence. In figure 7-14, the flow profile in the boundary layer and the wall skin friction coefficient are compared. The scale of coarse grid does not affect the accuracy of the numerical solutions.

$\Delta x_{max}/\Delta x_{min}$	Levels of MG	Time steps	E <sub>max</sub>
50	4	5000	0.0001
100	5	5000	0.0075
200	6	5000	0.0081
500	6	3472	0.0001
1000	7	3351	0.0001

Table 7-2 Comparison of the convergence with different multi-grid scale ratio

Maximum allowable error level

For the unsteady time-marching simulations based upon the dual-time stepping technique, the error level in the local pseudo-time iteration must be kept sufficiently small to guarantee the accuracy of the solutions. In the numerical flow method, the duration of the local time iteration is controlled with three input parameters: the maximum allowable error, the maximum and minimum iteration numbers. In this numerical experiment, the dependency of the solution on the maximum allowable error level was investigated. Figure 7-15 and table 7-3 show the results of the numerical tests.

Limit value of error	Pseudo-time iterations (averaged)	Max iterations	Min iterations
0.001 [%]	110	-	-
0.0005 [%]	150	-	-
0.0001 [%]	306	430	107
0.00005 [%]	398	530	148

Table 7-3 Comparison of the time steps with different error levels

The comparison of the velocity profile inside the laminar boundary layer (figure 7-15) shows little difference on the solutions among those calculated in the numerical tests. This result seems to indicate that the error level of 0.001 percent is sufficiently

small to obtain satisfactory solutions for this boundary layer test case. It must be mentioned that this requirement of small error level only applies to this specific case where small-scale flow motion inside the boundary layer is of interest. For blade row interaction problems in turbomachines where length scale of unsteadiness is much larger, the calculations may permit larger error to obtain adequate unsteady solutions.

The number of physical time steps in a period

The time resolution of the unsteady solutions improves when a larger number of time steps per period is used. In reality, the number must be restricted in terms of the computational cost. For the test calculations, 50, 100 and 150 of time steps were specified in one period and the numerical solutions are compared in figure 7-16a and table 7-4. The maximum allowable error was fixed to be less than 0.0005 percent. The velocity profiles shows little difference, suggesting that the number of time steps of 50 is sufficient. A number as small as 5 was attempted and it also successfully captured the qualitative trend (figure 7-16b).

Physical time steps per period	Averaged pseudo-time iterations (max:specified min)	Total iterations per period	$\Delta x_{\max} / \Delta x_{\min}$ (maximum)
50	173 (227:100)	8668	700
100	136 (182:100)	13594	700
150	126 (168:100)	18893	300

Table 7-4 Number of physical time steps per period

The total number of pseudo-time iterations per period is not proportional to the number of physical time steps per period. When a smaller number of physical time steps is used in one period, more pseudo-time iterations must be performed to sustain the same error level.

## 7.4. Centrifugal Pump with Vaned Diffuser

<b>Impeller</b>			
Inlet blade diameter	$D_1$	=	240 mm
Outlet diameter	$D_2$	=	420 mm
Blade span		=	40 mm
Number of blades		=	7
<b>Diffuser</b>			
Inlet vane diameter	$D_3$	=	444 mm
Outlet diameter	$D_4$	=	664 mm
Vane span		=	40 mm
Number of vanes		=	12
<b>Operating conditions</b>			
Rotational speed		=	2000 rpm
Flow rate coefficient	$\varphi$	=	0.048
Total pressure rise coefficient	$\Psi$	=	0.65
Reynolds number	$Re$	=	$6.5 \times 10^5$

Table 7-5 Parameters of Centrifugal Compressor Case

### 7.4.1. Centrifugal pump with a vaned diffuser

The final case for the validation is the turbomachinery flow in a centrifugal pump stage for which detailed time-averaged and unsteady data were available (Ubaldi et al. 1996). The model pump system consists of a centrifugal impeller with 7 unshrouded blades and a radial diffuser with 12 vanes. It was operated with air as working fluid, and the centrifugal impeller was operated in a low speed region with a peripheral velocity of 44 m/s. In the experiment, instantaneous and time-average velocity distributions were

measured at an impeller outflow section (4 mm downstream from the trailing edge of the impeller) using the hot wire with phase-lock sampling and ensemble-average techniques. The static pressure distributions on the casing surface were measured by high-response pressure transducers, and the instantaneous and time-average data were obtained using the same technique as for the velocity profile. Basic dimensions of the system and operating conditions are shown in table 7-5.

#### 7.4.2. Numerical condition

The pump system has 7 impeller blades and 12 diffuser vanes. To realise the experimental flow condition without modifying the configuration and to carry out a direct comparison of the unsteady data, the entire annulus must be included in the computational domain. For the flow simulations, an H-type mesh that consisted of 874000 nodal points (7 passages with 50x58x20 in the pitchwise, streamwise, spanwise directions per each passage for the first row and 12 passages with 30x65x20 per each passage for the second row) was used. A three-dimensional view of the computational mesh is shown in figure 7-17 for 3 impeller and 6 diffuser passages. One grid point was allocated inside the impeller tip clearance.

The whole annular flow simulation was started with an initial flow field given from the stage solution with a modified stage configuration (7 impeller blades and 14 diffuser vanes). Then the unsteady calculation was performed for 24 diffuser vane-passing periods where one period was discretised into 70 time steps. The first 12 periods in the unsteady calculation was performed with 40 pseudo-time iterations at each time step. Then the number of pseudo-time iterations was increased to a minimum of 50 to further reduce the error in the pressure field. The maximum error at each physical time step was kept smaller than 0.05 percent throughout the calculation. Figure 7-18 shows the histories of the blade forces acting on the impeller and the diffuser in the tangential direction. The histories show distinct changes in the pattern when the number of the pseudo-time iterations is increased after 12 diffuser vane passing period (840 time steps).

The boundary conditions specified in the simulations were total pressure, yaw and pitch flow angles at the inlet boundary, and static pressure at the exit boundary. The exit static pressure was carefully adjusted such that the mass flow rate was the same as the experiment. At a converged periodic state in the unsteady simulation, the time-

averaged flow rate coefficient of 0.048 was obtained. At this condition, the total pressure rise coefficient measured at the exit of the computational domain was 0.69.

#### 7.4.3. Comparison of the time-averaged data

The predicted time-averaged impeller discharged flow profiles at the mid-span position were compared with the experimental data. Figure 7-19 shows the radial velocity profile against the circumferential co-ordinate in the impeller relative frame. The circumferential velocity distribution is correctly captured in the calculation although the velocity level is underestimated compared to the experiment. This is partly attributed to the relatively coarse mesh in the spanwise direction that did not resolve the endwall boundary layers satisfactorily.

The relative tangential velocity distributions are compared in figure 7-20. They show reasonable agreement. However, a local velocity peak located near the mid-passage toward the pressure side is not captured in the numerical solutions. In the experimental study by Ubaldi et al. (1996), the cause of this velocity deficit was attributed to the tip clearance flow action that was known to convey the high loss fluid toward the pressure surface. In the flow method, the tip clearance flow was implemented by allowing the flux balance between neighbouring passages in the circumferential direction. In this simplified tip clearance model, the blade thickness was not taken into account. A numerical simulation without applying the tip clearance flow was also attempted, and the comparison of the results showed little difference as this local velocity deficit is concerned, suggesting that the current simple model did not adequately reproduce the tip leakage effect. More sophisticated tip clearance modelling should improve the numerical prediction.

#### 7.4.4. Comparison of Instantaneous unsteady data

Figure 7-21 shows the comparison of the unsteady radial velocity profiles between the experiment and the calculations at four instantaneous positions. The relative positions of the impeller blades and the diffuser vanes are indicated on the top and the bottom of the figures respectively. An interesting feature of blade row interaction is observed in the radial velocity distribution as a couple of local minima generated after

the passage of the impeller blade at the diffuser vane leading edge. One of the minimum velocity peaks corresponds to the diffuser leading edge that moves with the diffuser position. The other minimum peak, which locates between the impeller and diffuser positions, lags behind the diffuser leading edge peak and gradually reduces in amplitude with time.

A physical explanation is made for the second minimum here through the careful observation of the flow solutions. A diffuser vane leading edge perceives an impeller wake as a jet toward the pressure surface. A sudden change of the flow angle induces an inwardly oriented flow observed in the flow vector map (figure 7-22) and the absolute velocity contour map (figure 7-23). As a consequence, a relatively large radial velocity deficit is generated where the deflected wake fluid and the diffuser leading edge locate closely in circumferential position.

The wake fluid is gradually separated away from the diffuser vane through convection while keeping its inward orientation. The wake fluid and the diffuser vane in different circumferential locations form a couple of distinct valleys in the radial velocity profile that is seen in position A1 in figure 7-21. Through the course of time, the wake fluid regains radial momentum through mixing with the main flow as the distance from the diffuser vane increases (B1, C1 and D1).

The instantaneous relative tangential velocity profiles, corresponding to the radial velocity profiles in figure 7-21, are shown in figure 7-24. In the figure, the flow velocity is defined positive in the direction of the shaft rotation so that an impeller wake corresponds to the maximum velocity point near the impeller trailing edge position. Near the impeller trailing edge, the blade row interaction effect is overestimated due to a larger impeller blade wake in the numerical simulation. Nevertheless, the trend in the experimental data is correctly captured.

#### 7.4.5. Numerical parametric study

Several numerical parameters in the flow method have been tested for this turbomachinery flow case. The parameters investigated were the mesh density, the physical time resolution and the pseudo-time iteration numbers. The results of the numerical parametric study will serve to suggest typical value ranges of the parameters

when the flow method is applied to other turbomachinery flow simulations. The results will also give some idea about the sensitivity of the unsteady flow solutions for the centrifugal pump case presented.

The numerical tests have been performed with a modified stage configuration with 7 impeller blades and 14 diffuser vanes in order to avoid the excessive computational cost of the whole annular simulations. In this configuration, only 1 impeller passage and 2 diffuser passages were required to apply a direct periodicity at the outer-most periodic boundaries. The modified configuration made it difficult to compare the instantaneous numerical solutions with the unsteady experimental data that served as reference. Consequently, the comparison was made on the time-averaged solutions.

Mesh density dependency

In this mesh density dependency study, three sets of computational meshes refined in pitchwise (mesh A), spanwise (mesh B) and in both directions (mesh C) were used for the unsteady flow simulations. The dimensions of the meshes are listed in table 7-6.

	Total grid points	Impeller frame	Diffuser frame
Mesh A	136000	50x58x20	30x65x20
Mesh B	162300	35x58x30	26x65x30
Mesh C	238000	50x58x35	30x65x35

Table 7-6 Computational meshes

The comparison of the time-averaged data does not show marked difference among these meshes. Some differences are observed in the time-averaged relative tangential velocity distributions at the impeller outlet (figure 7-25) that correspond to the ensemble-averaged data presented earlier. Some differences are partly attributed to the different levels of the flow rate coefficient for those cases (0.0478, 0.0458, 0.0455 for mesh A, B and C respectively). Overall the results from all these meshes show a consistent trend suggesting relatively small grid dependency of this model flow case. In



the following parametric study, mesh A is used.

#### Number of Physical time steps per period

This parameter governs the time resolution relative to the time scale of blade row interaction. Unlike the unsteady laminar boundary layer flows, this model pump case involves higher order harmonic components in a period and it is necessary to resolve those with significant impact. For the test simulations, a diffuser vane passing period was divided into 30, 50, 70 and 100 time steps and the solutions for these cases were compared. A minimum of 40 pseudo-time iterations was performed at each physical time step, while the maximum error of less than 0.1 % was guaranteed for all the simulations.

Figure 7-26 shows the comparison of the predicted time-averaged relative tangential velocity and radial velocity profiles. The basic trend in the experiment is correctly captured with various time resolutions, although a noticeable difference is still present in the impeller wake regions implying the significance of the higher harmonic components. The time-step independent solutions seem to be obtained at the time steps of more than 70 in a period where little difference is observed in the velocity distribution.

This observation is further substantiated with the comparison of the time-averaged stator-generated unsteadiness that is defined as the normalised unsteady perturbations of the relative velocity about the time-averaged velocity profiles in the impeller relative frame (figure 7-27). The stator-generated unsteadiness is defined as,

$$\frac{\overline{W}}{U_2} = \frac{1}{N} \sum_{n=1}^N |W^n - W_{avg}| / U_2 \quad \text{eq. 7-3}$$

where  $W$  and  $W_{avg}$  are the instantaneous and time-averaged relative velocities in the impeller frame and  $U_2$  is the impeller peripheral velocity. Superscript  $n$  denotes the instantaneous time step and  $N$  is the number of time steps in one period. This stator-generated unsteadiness quantifies the perturbations from the diffuser vanes observed in the impeller frame and is expected to be a strong indication of the unsteady blade row interaction effects. From the comparison, it is apparent that a time-step convergent solution is obtained with 70 time steps in a period.

In the unsteady laminar boundary layer simulations, it has been demonstrated that a

single harmonic component can be captured using a much smaller number of time steps with reasonable accuracy. The results imply the significance of the higher harmonic unsteadiness on the time-averaged solutions in this centrifugal pump flows.

#### Number of pseudo-time iterations

The number of pseudo-time iterations at each physical time steps was found to affect both accuracy and convergence. Generally, the number of pseudo-time iterations needs to be increased with increasing mesh density or with decreasing number of physical time steps per period. In the unsteady flow simulations, the periodicity of flow variables was monitored throughout the computations as an indication of convergence. It is important to recognise that the inviscid part of the flow will converge at a very different rate compared to that of the near wall viscous flow owing to the different speeds of information propagation. A sufficient number of pseudo-time iterations has to be performed so that the viscous as well as the inviscid parts of the flow field are fully converged at each physical time step. It was found that if the number of pseudo-time iterations at each physical time step was not sufficient, accumulation of errors could lead to a stability problem. Figure 7-28a shows an example of such a case. In this viscous flow simulation, 20 pseudo-time iterations were performed at each physical time step. The history of the blade forces indicated periodic behaviour for a while before an oscillatory pattern started to grow at about 800 physical time steps. The solution eventually became divergent. For the same case, a converged solution was obtained when the number of pseudo-time iterations was increased to 30 or more.

For the centrifugal pump simulations, 30 pseudo-time iterations at each physical time step seem to achieve a sufficient accuracy of the solutions (Figure 7-28b).

### **7.5. Summary**

The unsteady incompressible flow method described in Chapter 6 has been tested with several validation cases in order to demonstrate that the method combining the dual-time stepping technique and the pseudo-compressibility method was correctly and effectively implemented.

A low speed flow in a linear turbine cascade has been calculated and the numerical results were compared with the experimental data. The comparison showed good agreement, demonstrating the applicability of the flow method to steady incompressible viscous turbomachinery flow calculations.

A laminar boundary layer flow with free-stream fluctuation was calculated and excellent agreement between the numerical solutions and analytical data was obtained, validating the numerical method for the basic unsteady incompressible flow calculations.

The flow method was also applied to a centrifugal pump with a vaned diffuser and the numerical solutions were compared with the unsteady experimental data. The solutions show satisfactory agreement with the experimental data, validating the applications to the unsteady incompressible turbomachinery flows.

Through the course of validation for the pump flow case, some attempts were made to interpret the observation of the blade row interaction phenomena in the instantaneous velocity profiles both from the experiment and the numerical simulations. In fact, those flow phenomena were recognised and pointed out by experimenters (Ubaldi et al. 1996), but clear explanations were not made due to a lack of detailed flow data. A numerical simulation reveals a clear picture of the flow mechanism, demonstrating the usefulness of the numerical techniques in the flow analysis.

A series of numerical tests investigating the dependency of the flow solutions on several input parameters were conducted for the unsteady flow cases, and the results provided some useful guideline about the flow method for other applications.

# 8. ANALYSIS OF HYDRAULIC TURBINE STAGES

## 8.1. Introduction

In Chapter 5, the flows in high-speed centrifugal compressor stages with three settings of radial gap were calculated, and the levels of the efficiency among different radial gap configurations were compared. The results revealed a strong dependency of the stage efficiency on the radial gap, suggesting a substantial influence of blade row interaction.

In this chapter, the main concern is the effects of radial gap and the blade row interaction on radial turbine stages. In turbines, the flow is of an accelerating nature so that the development of the boundary layers on the blade surface is less significant than in compressors. Consequently, the unsteady flow disturbances by the wake flows in turbine stages are relatively smaller compared to those in compressors. On the other hand, the potential flow effect that is essentially an inviscid flow phenomenon will have a similar magnitude for both turbines and compressors. Therefore, the potential flow interaction will be relatively significant for radial turbine stages.

Meanwhile, in hydraulic machines, the pressure gradient induced around a blading becomes much larger than that in an aerofoil due to a large density of water. Consequently, the potential flow interaction in hydraulic machines may have significant effects on the stage performance.

In order to investigate the effect of radial gap on the performances of radial turbine stages, a generic Francis turbine wheel was combined with nozzle vane stages with different radial gaps and unsteady flow simulations were carried out using the dual-time stepping incompressible flow method extensively validated in Chapter 7.

## 8.2. Francis Turbine Flows with Blade Row Interaction

### 8.2.1. Generic Francis turbine stage

The model turbine rotor has 18 shrouded-blades with a constant inlet diameter of 0.85 m and an outlet tip diameter of 0.685 m. At a nominal operating point of 500 rpm shaft speed, the turbine rotor accommodates the volume flow rate of about 15 [m<sup>3</sup>/s] with a head of 170 [m]. The specific speed of the turbine at this flow condition is 0.77.

The nozzle blade profile was taken from the NACA0012 airfoil. Three settings of nozzle configurations with different radial gaps of 5%, 10% and 15 % of rotor inlet radius (hereafter they will be referred to as 5%, 10% and 15% gap cases, respectively) were adopted. The number of nozzle vanes was taken to be 18. The nozzle vane was scaled to keep a constant solidity of 1.15 defined at the trailing edge position and the vane angle was fixed at 79 degrees.

### 8.2.2. Numerical condition

Unsteady flow simulations were carried out with a nozzle and a rotor passage. For all the radial gap configurations, the meridional length of the computational domains was kept the same that starts from a constant radius inlet to an axial exit. A constant total pressure and yaw and pitch flow angles were specified at the inlet boundary while a constant static pressure on the crown side was specified and the static pressure variation were calculated to satisfy the radial equilibrium condition at the exit boundary. With the boundary conditions specified, the differences in the volume flow rate among different radial gap configurations were found to be small within a range of less than 1.5 percent when they were compared among the solutions with the same mesh density.

Three sets of meshes with different mesh densities in the streamwise sections were used to calculate each radial gap case in order to obtain a mesh independent trend. The fine, medium and coarse meshes are denoted as mesh F, mesh M and mesh C, and the flow solutions from mesh M are used as references in the following discussions. The details of the computational meshes in the numerical experiments are shown in table 8-1 and a three-dimensional view of the Francis turbine stage is shown in figure 8-1.

The unsteady flow simulations were started using mesh C and the flow solutions

were interpolated to generate initial flow fields for successive finer meshes. In order to establish a perfect periodicity of the flow solutions, at least 35 periods in total were calculated from the initial flow field for the calculations with mesh F. Throughout the calculations, the number of physical time steps per blade passing period was specified to be 70. For all the unsteady flow simulations, the maximum allowable error in the pseudo-time iteration was specified to be 0.01 percent.

	Mesh density	Grid points	Nozzle frame	Rotor frame
F - 5% gap	fine	269500	50x61x35	50x93x35
F - 10% gap	fine	287000	50x84x35	50x93x35
F - 15% gap	fine	315000	50x87x35	50x93x35
M - 5% gap	medium	161700	35x61x30	35x93x30
M - 10% gap	medium	172200	35x84x30	35x93x30
M - 15% gap	medium	189000	35x87x30	35x93x30
C - 5% gap	coarse	77000	25x61x20	25x93x20
C - 10% gap	coarse	82000	25x84x20	25x93x20
C - 15% gap	coarse	90000	25x87x20	25x93x20

Table 8-1 Computational meshes

### 8.2.3. Performance map

Two different definitions of the turbine efficiency were used to evaluate the performance of the hydraulic turbines. The first definition  $\eta_1$  is based upon the specific entropy change as (Denton 1993),

$$\eta_1 = \frac{h_{inlet} - h_{exit}}{h_{inlet} - h_{exit} + T_{exit} (s_{exit} - s_{inlet})} \quad \text{eq. 8-1}$$

The enthalpy and the entropy change between the inlet and exit can be estimated by calculating the mass-averaged rothalpy defined in individual relative frames

(Appendix 4). The inlet static temperature was taken as the ambient temperature.

Alternatively, the ratio of the power to the shaft to the change in the head available in the water can be used to define efficiency  $\eta_2$  as (Drtna and Sallaberger 1999),

$$\eta_2 = \frac{T\omega}{P_{t,inlet} - P_{t,exit}} = \frac{U_3 W_{\theta 3} - U_4 W_{\theta 4}}{P_{t,inlet} - P_{t,exit}} \quad \text{eq. 8-2}$$

where subscripts 3 and 4 indicate the leading edge and trailing edge of the rotor blades and  $U$  and  $W_\theta$  are the blade rotation speed and the relative velocity component in the circumferential direction, respectively.

	Volume flow [m <sup>3</sup> /s]	Efficiency $\eta_1$	Efficiency $\eta_2$
F – 5% gap	15.36	0.9296	0.9311
F – 10% gap	15.15	0.9302	0.9339
F – 15% gap	15.15	0.9313	0.9358
M – 5% gap	14.95	0.9301	0.9341
M – 10% gap	14.96	0.9303	0.9340
M – 15% gap	14.98	0.9305	0.9354
C – 5% gap	15.49	0.9218	0.9258
C – 10% gap	15.59	0.9218	0.9269
C – 15% gap	15.41	0.9226	0.9278

Table 8-2 Entropy rise in the stage configurations

Both definitions were used to calculate the stage efficiency, and they are tabulated with the volume flow rate in table 8-2. They present a consistent trend that has the highest efficiency with the 15% gap, and the efficiency reduces as the radial gap decreases. The definition  $\eta_2$  tends to give higher values than the definition  $\eta_1$ .

Although the same boundary conditions were applied, there were small differences in flow rate among the solutions from different mesh densities. The solutions

with mesh C predicted a marginally higher mass flow level compared to those with mesh M and mesh F. The difference is probably attributed to the fact that the coarse mesh C does not have spatial resolutions near the wall to resolve the boundary layers. Therefore, the predicted mass flow rate is increased for mesh C solutions. It is also noticeable that the solutions with mesh C predicted a lower efficiency level. However, the reason for the difference is still not clear.

Figure 8-2 shows the comparison of the efficiency  $\eta_2$  among different radial gap configurations. Although there are slight differences in the efficiency levels, the solutions show a mesh independent trend. However, the differences are very small among different radial gap configurations, suggesting a relatively small influence of the radial gap on the stage performance.

Figure 8-3 shows the development of entropy along the streamwise direction calculated with the mass-flow-averaged rothalpy loss in the streamwise sections. Although only the results from mesh M are shown, the results from mesh F and mesh C show a similar trend. Small oscillatory motions in the vicinity of the blade leading and trailing edges are probably due to numerical errors.

In the figure, the leading edge and trailing edge positions of the nozzle vanes are indicated by solid triangles and squares and the values listed between them suggest the entropy rise in the nozzle passage. It is obvious that the differences in entropy generation in the nozzle passages largely contribute to the difference in total entropy generation.

After the trailing edge of the nozzle, the entropy continues to increase gradually in the vaneless space and through the rotor passages until a rapid increase near the rotor trailing edge.

In the following sections, the mechanisms of the entropy rise that causes the differences in efficiency among different radial gap configurations are examined by dividing the flow passage into the nozzle passage, the vaneless space and the rotor passage.

#### 8.2.4. Nozzle passage

In radial configurations, any change in the radial gap between the nozzle vanes



and the rotor results in changes in the velocity level as well as in the width of the nozzle passage. This is quite a contrast to the axial flow turbine stages where they are usually independent of the blade row spacing. If the number of nozzle vanes is kept constant, the reduction of the radial gap increases the velocity level. The losses generated in the boundary layers and through the wake flow mixing are known to increase with increasing flow velocity (Denton 1993). Figure 8-4 shows the comparison of the time-averaged and mass-averaged flow velocity distribution against meridional distance among different radial gap configurations. The leading edge and trailing edge of the nozzle vanes are indicated with solid triangles and squares. The difference in the flow velocity at the trailing edge reaches about 3 m/s between the 5% and 15% gap configurations. Through the nozzle vane passage, the flow velocity increases steadily (figure 8-4) and the gradient of the entropy rise also increases as the boundary layer loss increases in figure 8-3. Therefore, the configuration with a smallest radial gap (5% gap) has the highest entropy rise, and increasing the radial gap results in a reduction of entropy rise.

Figure 8-5 shows the comparison of the unsteady velocity disturbances in the nozzle passages at midspan among three radial gap configurations. The potential flow disturbances from the turbine rotor blade cause a velocity fluctuation in the nozzle passages, and they become stronger with a smaller radial gap. Although the magnitude of the velocity fluctuation is small, the unsteady flow is expected to have some effect to enhance the mixing of the flow non-uniformity that will increase the loss generation.

#### 8.2.5. Vaneless space

For radial turbines, a wake line shed from the upstream nozzle vanes is aligned to the flow direction in the vaneless space. The flow in the vaneless space is accelerating due to the reduction of the passage area so that the wake will be stretched, and the wake segment is lengthened toward downstream. This effect is illustrated in figure 8-6 in the two-dimensional convergent duct model. This wake stretching phenomenon is analogous to the wake stretching model by Smith (1966) and is expected to benefit efficiency. However, the amount of wake recovery is not significant, given a relatively small velocity change in the vaneless space (13% increase in velocity for 15% gap case).

Flow speed reaches its highest level in the vaneless spaces (figure 8-4) and the entropy generation by the endwall boundary layers may become a considerable amount.

Therefore, at first sight, it may seem that a small radial gap is preferable as it reduces the length of the flow passage and, effectively, the loss due to the endwall boundary layers. However, as seen in figure 8-3, the configurations with smaller radial gap have consistently higher entropy at the leading edge of the rotor blade, suggesting a relatively small impact of the endwall boundary layer loss in the vaneless space compared to the losses generated in the nozzle vane passage.

### 8.2.6. Rotor passage

In figure 8-3, the entropy rises moderately in the fore part of the rotor passage and rapidly increases near the trailing edge, which is caused by the increasing relative flow velocity that produces higher boundary layer loss and wake flow mixing loss at the trailing edge. The difference in the entropy level at the rotor leading edge position was reduced slightly at the trailing edge, suggesting a lower entropy rise for a smaller radial gap case.

For the current sets of Francis turbine stages, wake chopping and subsequent wake stretching occur in the rotor passage, which are clearly seen in the vorticity contour maps on the mid-span in figure 8-7. It should be noted that the wakes shed from the nozzle vanes are also influenced by the meridional flow velocity difference between the hub and casing so that the wake stretching occurs in a three-dimensional manner. Figure 8-8 shows the relative velocity contours in the meridional sections near the suction surface of the rotor blade for 5% radial gap configuration. In the figure, the wakes shed from the nozzle vanes are indicated with successive horizontal lines, which gradually incline through the rotor passage. Since the wake stretching process reduces the flow mixing loss, part of the wake flow mixing loss originated from the nozzle vanes can be recovered to reduce the difference in the entropy levels among different radial gap configurations.

Another contributing factor for a larger entropy rise for a larger radial gap is the flow incidence at the rotor leading edge. Despite the two-dimensional configuration of the nozzle and vaneless space, the potential flow field generated by the turbine rotor makes the flow to be non-uniform in the spanwise direction. Figure 8-9 shows a static pressure distribution on meridional surface in the middle passage of the nozzle vanes. A positive pressure gradient from the casing toward the hub, which is generated by the

rotor blades, is seen for all the radial gap configurations. This pressure gradient causes the migration of fluid toward the casing that is observed in figure 8-10 in the axial (in the spanwise direction) flow velocity contours, where a positive value suggests that the flow is oriented toward the casing. The flow velocity vectors in figure 8-10 also confirm the migration of flow toward the casing.

The comparison of the pressure contours (figure 8-9) among different radial gap configurations shows that this spanwise pressure gradient is observed further upstream for a larger radial gap configuration, suggesting an interaction between the nozzle vanes and the rotor potential flow field. Therefore, the flow goes through a cross-flow pressure gradient longer for a larger radial gap configuration that promotes the flow migration toward the casing. Figure 8-11a shows the comparison of the pitchwise-averaged meridional flow velocity distribution along the span immediately upstream from the rotor. The flow migration results in an accelerated flow on the casing side and it is further pronounced when the radial gap is larger (figure 8-11a). This flow migration also causes a variation in the relative pitchwise flow angle among different radial gaps (figure 8-11b), which is expected to be responsible for the higher loss levels for larger radial gap configurations. The rotor blade angle at the leading edge varies from about 43 degrees at the hub to 30 degrees at the casing so that the inflow has negative incidence over the span (figure 8-11b). Although a certain level of negative incidence is usually preferable, an excessive negative incidence for 15% gap configuration appears to cause loss in figure 8-7 where regions of high vorticity that correspond to the high shear stress are found on the pressure surface of the rotor while it is less clear for 5% and 10 % radial gap configurations. Consequently, the entropy rise in the rotor passage with 15% gap is the highest and it decreases with decreasing the radial gap. The results suggest that the optimum radial gap exists in terms of the flow incidence effect.

The wake/boundary layer interaction on the blade surface does not appear to have great impact on the entropy generation. This is because the flow in the turbine rotor is accelerating and the blade surface boundary layers are relatively thin, which are less influenced by the flow disturbances due to upstream wakes.

### 8.2.7. Blade forces

The fluctuation of the blade loading due to blade row interaction is a great

concern in structural design of hydraulic machines. In order to observe the effects of the different radial gap on the blade loading, the blade forces that represent the blade loading are calculated by integrating the pressure forces on the nozzle vane and rotor blade surfaces.

Figure 8-12 shows the histories of forces on the nozzle vanes in the tangential and radial directions. As expected, a configuration with a smaller radial gap tended to have a larger blade force fluctuation due to stronger blade row interaction. It was also found that the mean values of the forces tend to increase in absolute magnitude with decreasing radial gap. This can be explained by the different flow velocities around the vanes among different radial gap configurations, which alter the magnitude of the loading.

Similarly, the histories of blade forces on the rotor blade in the tangential directions are shown in figure 8-13a. The fluctuation of the blade force for 5% radial gap configuration has an amplitude of more than 7 percent of the mean value, and the unsteadiness is concentrated near the leading edge as seen in figure 8-13b, which shows the tangential blade force distributions divided into four meridional sections. The results suggest that blade row interaction manifest itself the high blade loading fluctuation near the leading edge of the rotor blades that may become detrimental in terms of structural performance if blade rows are too closely located.

### **8.3. Summary**

Series of numerical experiment of generic Francis turbine stages has been performed in order to examine the impact of the different radial gaps on the hydraulic performances.

The numerical performance predictions showed a consistent trend from different sets of meshes where the maximum efficiency was achieved when the radial gap was the largest, and efficiency was decreased as the radial gap was decreased. However, the differences in the calculated efficiency turned out to be small.

In the nozzle and the vaneless space, the differences in the loss levels were partly attributed to the boundary layer loss and the flow mixing loss: the loss through

both mechanisms increases when the flow velocity around the blade increases. Since the flow velocity tends to increase with decreasing the radial gap, the loss generation in the nozzle vane and vaneless space increases accordingly.

The potential flow field generated by the turbine rotor influences the spanwise distribution of flow at the inlet of the rotor itself that changed the flow incidence angle. The extent of the spanwise flow variation also depended on the radial gap where the variation was amplified for a larger radial gap configuration. For the current test turbine configurations, a large radial gap increased the relative flow angle, causing an excessively negative incidence that generated loss in the rotor passage. Consequently, the difference in the total loss after the rotor trailing edge became smaller than that measured at the rotor leading edge.

The wake recovery through the wake stretching existed in both the vaneless space and the rotor passage of the radial turbine stage. The wake stretching in the rotor occurred in a three-dimensional manner due to the differences in the flow velocities in both pitchwise and spanwise directions.

## 9. CONCLUSIONS AND RECOMMENDATIONS

The principal aim of this dissertation was to investigate the blade row interaction effects in radial turbomachines in subsonic or incompressible flow ranges. The intensity of the blade row interaction is directly related with the radial gap between blade rows, and it was one of the main concerns in the current research. A high-speed centrifugal compressor stage and a hydraulic turbine stage were chosen as test cases and the unsteady flows were investigated through numerical simulations. A three-dimensional unsteady Navier-Stokes time-marching method developed by He (1996c) was utilised for the compressible centrifugal compressor flow simulations. For the hydraulic turbine flow simulations, a new three-dimensional Navier-Stokes time-marching method based upon the dual-time stepping technique and the pseudo-compressibility has been developed through the course of the research and was validated and applied to the unsteady flow simulations with blade row interactions.

The developments of the loss along the flow paths were traced and compared among radial turbomachines with different settings of radial gap, and the differences in the loss generations were examined through detailed analyses of the unsteady flow solutions. The results from the unsteady numerical flow calculations provided, to the author's knowledge, a first of the kind database for the blade row interaction effects on the performance of radial turbomachines.

### 9.1. Numerical Method

For the analysis of centrifugal compressor flows, an efficient time-marching method with the time-consistent multi-grid method (He 1996c) was adopted. For the validation purpose, the flow method was applied to a steady centrifugal impeller flow and the numerical solutions agreed well with experimental data, reproducing the development of the viscous flows through the passage correctly.

For the hydraulic turbine flow calculations where the time-consistent flow method was not applicable, a new unsteady incompressible flow method was proposed

and implemented into a numerical code.

The incompressibility of the flows is treated by introducing the pseudo-compressibility (Chorin 1967) to recover a time-dependent form of the flow governing equations, which is expected to have an advantage over the pressure based methods in terms of the convergence speed. The accuracy in the physical time, which is an essential property for the unsteady flow calculations, is guaranteed by adopting the dual-time stepping technique (Jameson 1991) with a second order implicit discretisation of the flow governing equations in the physical time. At each discrete physical time step, the incompressible flow governing equations with the pseudo-compressibility term are solved in the pseudo-time domain using the four-stage Runge-Kutta time integration method and the convergence of the solutions is greatly accelerated with the multi-grid method. The unsteady incompressible flow governing equations are discretised in the finite volume form with variables stored at the cell centres. The flux terms at cell surfaces are evaluated by a linear interpolation between adjacent cells and this in turn constructs the scheme equivalent to the second order central difference scheme in the finite difference discretisation. Fourth order numerical damping terms are added in the governing equations to suppress the odd-even decoupling of the flow variables. The scaling operator of Arnore (1994) is used to avoid the unnecessary numerical damping in the shear layer.

The newly developed method for the unsteady incompressible flow calculations has been validated against a range of test cases.

A series of steady, three-dimensional, viscous flow calculations in a low-speed linear turbine cascade was conducted. The predicted static pressure coefficient distributions on the blade surface compared very well with the experimental data. The development of the streamwise vortices due to viscous shear layer observed in the experiment was correctly captured in the numerical solutions, validating the treatment of the viscous terms including the turbulence model currently adopted.

The method was tested with two unsteady viscous flow calculations. First, the prediction of the low speed laminar boundary layer with a sinusoidal free-stream fluctuation showed excellent agreement with the theoretical solutions, validating the time integration scheme based upon the dual-time stepping technique. Second, an unsteady radial turbomachinery flow with blade row interaction was calculated and the results

were compared with the unsteady experimental data. For the direct comparison of the unsteady flow data, whole annular was included in the calculation domain. Despite a relatively coarse computational mesh used for the calculations, the comparison of the unsteady data was encouraging. Moreover, some details of the blade row interaction phenomena were clearly captured in the numerical flow prediction that compared well with the experimental data.

For unsteady test flow cases, some numerical tests were conducted to examine the dependency of the flow solutions on the mesh density, the physical time resolution for unsteady flow simulations, and other several numerical parameters. The results served to justify the sensitivity of the numerical solutions and they also provided useful references of the parameters when the method was applied to other flow calculations.

## **9.2. Flows in Centrifugal Compressors**

Centrifugal compressor stage flows with three settings of radial gap were calculated to investigate the effects of blade row interaction on the stage performance. The centrifugal compressor stages were configured with a backward sweep impeller combined with a generic diffuser. The vaneless space had a profile of a constant area diffuser to yield the same level of flow velocity at the diffuser inlet.

The numerical flow predictions suggested that the stage efficiency was decreased if the radial gap was decreased to intensify the blade row interaction effects.

The potential flow disturbances from the diffuser vanes had an effect to increase the loss generation in the impeller passage, which would become significant when the radial gap was relatively small. An enhanced mixing of the flow non-uniformity by the flow unsteadiness seemed responsible for the additional loss generation.

The impeller wake/diffuser vane boundary layers interaction also deteriorated the efficiency by increasing the loss generation through the mixing of the boundary layer flow with the main flow.

The implication of the wake chopping by the diffuser vanes depends on stage configurations, which is governed by the angle  $\sigma$  between the diffuser vane suction



surface and the wake line at the leading edge (figure 5-10). If  $\sigma$  is larger than 90 degrees, the wake will be stretched through the diffuser passage to recover wake flow mixing loss. On the other hand, if  $\sigma$  is smaller than 90 degrees, which is common for centrifugal compressors with a impeller backward sweep, the wake will be compressed through the diffuser passage and subsequent dissipation of wake flow will increase the mixing loss. Therefore, a closer radial gap in stage centrifugal compressors is detrimental as far as the wake chopping effect is concerned since the presence of the diffuser vanes compresses the wake to generate more mixing losses, which would be otherwise recovered through the wake stretching in the vaneless space.

### 9.3. Flows in Radial Turbines

A series of numerical simulations of hydraulic turbine stages has been performed to examine the impact of the radial gap and the blade row interaction effects on hydraulic performance. The radial turbine stages with three settings of radial gap were configured with a generic Francis turbine and a nozzle stage. The angle of the nozzle vane trailing edge was fixed to a constant value for all the settings of radial gap to produce the same flow swirling angle at the rotor leading edge.

The numerical predictions of efficiency in radial turbine stages with three settings of radial gap, using computational meshes with different mesh density, showed a subtle but consistent variation. The highest efficiency was obtained in the setting of largest radial gap, and the efficiency decreased with the reduction in the radial gap, although the difference was very small among different settings of radial gap.

The loss in the nozzle passage due to the surface boundary layers and the wake flow mixing was increased when the radial gap was decreased. Although the increase of loss was identified to be mainly due to a steady process through the nozzle vane surface boundary layers and the wake flow mixing, it also seemed to be influenced by the potential flow disturbances from the downstream turbine rotor.

The potential flow field produced by the turbine rotor influenced the flow velocity distribution in the vaneless space and, consequently, the spanwise relative flow angle distribution ahead of the rotor inlet. In the numerical simulations, the spanwise variation of the relative flow angle was enhanced when the radial gap was increased. If

the radial gap became larger than a certain level, the deviation from the design flow incidence angle at the rotor inlet was increased to deteriorate the efficiency. In the test hydraulic turbine stages, the large loss generation in the nozzle for a setting with a small radial gap was partly cancelled by the flow incidence loss.

The wakes generated in the nozzle vanes were attenuated reversibly through the flow acceleration in the vaneless space as well as through the rotor passage by the wake chopping and stretching effects. Therefore, a larger radial gap promoted the wake stretching effect and was expected to be beneficial as far as the wake stretching effect was concerned. The wake segments chopped by the rotor leading edges were stretched inside the turbine rotor not only in the pitchwise direction but also in the spanwise direction in a three-dimensional manner.

#### **9.4. Suggestions for Future Research**

With respect to the numerical method for unsteady flow simulations, the following suggestions for further work are made.

The current numerical method adopts a single block H-type computational mesh to discretise a flow passage and it occasionally requires some finite volume cells to be deformed locally near the blade leading edge or the trailing edge. Although the influence of the grid skewness was not tested, it is expected to cause interpolation errors in extreme cases. It is especially detrimental for certain hydraulic pump flow calculations, where the blade angle exceeds 80 degrees. To alleviate the problems associated with a single block H-type grid, it is desirable to extend the numerical method to deal with a multi-block grid system. If it is economically viable, the unstructured grid system is another possible alternative.

A central difference scheme adopted in the current numerical method permits an oscillatory solution so that it is necessary to apply a numerical damping to obtain stable solutions. However, controlling the amount of numerical damping requires some experience to generate accurate solutions. A higher order upwinding scheme that introduces the physical properties of the flow equations into the discretisation is, therefore, recommended since it guarantee a stable calculation without recourse to an explicit numerical damping. For high-speed flow calculations, some forms of limiting

functions for the flux evaluations must be applied in upwinding schemes in order to deal with the shockwaves.

An algebraic mixing-length turbulence model is employed in the current unsteady flow methods assuming that a typical length scale of turbulence is still much smaller than that of the physical periodic unsteadiness concerned. Although various types of turbulence modelling are widely used for unsteady flow simulations, there is still some uncertainty about the validity of representing the effect of turbulence, which is essentially unsteady, through a local time-averaging operation. If computer power is available in the future, more sophisticated but time-consuming treatments of turbulence should be applied (e.g. Large Eddy Simulation: LES, etc.)

With respect to the blade row interaction effects on the performance of radial turbomachines, the following suggestions are made.

The radial turbomachinery stages chosen as test cases in the current research are characterised with the configurations of those typical machines. The conclusions obtained through the current numerical experiments are, therefore, expected to apply to general radial stage turbomachines. However, this should be confirmed by calculating different stage configurations.

Quantitative contributions of the individual loss mechanisms to the efficiency must be tested and compared in order to give further insights into the turbomachinery design. Although the loss mechanisms are rarely independent, each loss mechanism should be treated separately, if possible, to evaluate the impact on the total performance. Some of the loss mechanisms are inherently of a three-dimensional nature and must be treated through the three-dimensional numerical methods. However, for those of a two-dimensional nature, two-dimensional approaches seem more appropriate for the purpose, given the time consuming nature of the unsteady flow simulations.

Finally in order to further substantiate the observation of the numerical simulations in the current research, experiments with actual radial turbomachines should be carried out. If the details of the flow field are to be measured in the experiment, it also serves to validate the numerical method. Moreover, the comparison of the results from both the calculations and the experiments will complement each other to provide further

insight into the mechanisms of flows with blade row interaction.

## REFERENCES

Ackerberg, R. C. and Phillips, J. H., (1972), "The Unsteady Laminar Boundary Layer on a Semi-Infinite Flat Plate due to Small Fluctuations in the Magnitude of the Free-Stream Velocity," *Journal of Fluid Mechanics*, Vol. 51, Part 1, pp. 137-157.

Adamczyk, J. J., (1985), "Model Equation for Simulating Flows in Multistage Turbomachinery," ASME Paper No. 85-GT-226.

Adamczyk, J. J., Mulac, R. A. and Celestina, M. L., (1986), "A Model for Closing the Inviscid Form of the Average-Passage Equation System," *ASME Journal of Turbomachinery*, Vol. 108, pp. 180-186.

Adamczyk, J. J., Celestina, M. L., Beach, T. A. and Barnett, M., (1990), "Simulation of Three-Dimensional Viscous Flow within a Multistage Turbine," *ASME Journal of Turbomachinery*, Vol. 112, pp. 370-376.

Adamczyk, J. J., (1996), "Wake Mixing in Axial Flow Compressors," ASME Paper No. 96-GT-29.

Addison, J. S. and Hodson, H. P., (1990), "Unsteady Transition in an Axial-Flow Turbine: Part 1 - Measurements on the Turbine Rotor," *ASME Journal of Turbomachinery*, Vol. 112, pp. 206-214.

Amineni, N. K., Engeda, A., Hohlweg, W., C. and Direnzi, G., (1996), "Performance of Low Solidity and Conventional Diffuser Systems for Centrifugal Compressors," ASME Paper 96-GT-155.

Arndt, N., Acosta, A. J., Brennen, C. E. and Caughey, T. K., (1989), "Rotor-Stator Interaction in a Diffuser Pump," *ASME Journal of Turbomachinery*, Vol. 111, pp. 213-221.

Arnone, A., (1994), "Viscous Analysis of Three-Dimensional Rotor Flow using a Multigrid Method," *ASME Journal of Turbomachinery*, Vol. 116, pp. 435-445.

Arnone, A., Pacciani, R. and Sestini, A., (1995), "Multigrid Computations of Unsteady Rotor-Stator Interaction using the Navier-Stokes Equations," *ASME Journal of Fluid Engineering*, Vol. 117, pp. 647-652.

Baines, N. C., (1996), "Flow Development in Radial Turbine Rotors," ASME Paper No. 96-GT-65.

Belov, A. A., Martinelli, L. and Jameson, A., (1994), "A Novel Fully Implicit Multigrid Driven Algorithm for Unsteady Incompressible Flow Calculations," In Proceedings, Second European CFD Conference ECCOMAS 94.

Benson, R. S., (1970), "A Review of Methods for assessing Loss Coefficients in Radial Gas Turbines," International Journal of Mechanical Sciences, Vol. 12, pp. 905-932.

Came, P. M. and Marsh, H., (1974), "Secondary Flow in Cascades: Two Simple Derivations for the Components of Vorticity," IMechE Journal Mechanical Engineering Science, Vol. 16, No. 6.

Came, P. M. and Robinson, C. J., (1999), "Centrifugal Compressor Design," IMechE Journal of Mechanical Engineering Science, Vol. 213, pp.139-155.

Casey, V. M., Dalbert, P. and Roth, P., (1992), "The Use of 3D Viscous Flow Calculations in the Design and Analysis of Industrial Centrifugal Compressors," ASME Journal of Turbomachinery, Vol. 114, pp. 27-37.

Cebeci, T., (1977), "Calculation of Unsteady Two-Dimensional Laminar and Turbulent Boundary Layers with Fluctuations in External Velocity," Proceeding of Royal Society (London) A. 355, pp. 225-238.

Chima, T. V., (1996), "Calculation of Tip Clearance Effects in a Transonic Compressor Rotor," ASME Paper No. 96-GT-114.

Choi, Y. H. and Merkle, C. L., (1993), "The Application of Preconditioning in Viscous Flows," Journal of Computational Physics, Vol. 105, pp. 207-223.

Chorin, A. J., (1967), "A Numerical Method for Solving Incompressible Viscous Flow Problems," Journal of Computational Physics, Vol. 2, pp. 12-26.

Chriss, R. M., Hathaway, M. D. and Wood, J. R., (1996), "Experimental and Computational Results from the NASA Lewis Low-Speed Centrifugal Impeller at Design and Part-Flow Condition," ASME Journal of Turbomachinery, Vol. 118, pp. 55-65.

Cleak, J. G. E. and Gregory-Smith, D. G., (1992), "Turbulence Modelling for Secondary Flow Prediction in a Turbine Cascade," ASME Journal of Turbomachinery, Vol. 114, pp. 590-598.

Copenhaver, W. W., Puterbaugh, S. L. and Hah, C., (1993), "Three-Dimensional Flow Analysis inside Turbomachinery Stages with Steady and Unsteady Navier-Stokes

Method," ISABE 93-7095.

Dawes, W. N., (1995), "A Simulation of the Unsteady Interaction of a Centrifugal Impeller With Its Vaned Diffuser: Flow analysis," ASME Journal of Turbomachinery, Vol. 117, pp. 213-222.

Dawes, B. and Denton, J., (1999), "CFD for Turbomachinery Design," Proceedings of the IMechE, Journal of Mechanical Engineering Science, Part C, Vol. 213, No. C2, pp. 109-124.

Dean, R. C. Jr., (1959), "On the Necessity of Unsteady Flow in Fluid Machines," Trans. ASME, Journal of Basic Engineering, Vol. 81, No.24.

Dean, R. C. and Senoo, Y., (1960), "Rotating Wakes in Vaneless Diffusers," Trans. ASME, Journal of Basic Engineering, Vol. 82, pp. 563-574.

Denton, J. D., (1982), "An Improved Time Marching Method for Turbomachinery Flow Calculation," Numerical Methods in Aeronautical Fluid Dynamics, ed. Roe, P. L., Academic Press, pp. 189-210.

Denton, J. D., (1992), "The Calculation of Three Dimensional Viscous Flow Through Multistage Turbomachines," ASME Journal of Turbomachinery, Vol. 114, pp. 18-26.

Denton, J. D., (1993), "Loss Mechanism in Turbomachines," ASME Journal of Turbomachinery, Vol. 115, pp. 621-656.

Drtina, P. and Sallaberger, M., (1999), "Hydraulic Turbines - Basic Principles and State-of-the-Art Computational Fluid Dynamics Applications," IMechE Journal of Mechanical Engineering Science, Vol. 213, pp. 85-102.

Eckardt, D., (1976), "Detailed Flow Investigations Within a High-Speed Centrifugal Compressor Impeller," ASME Journal of Fluid Engineering, pp. 390-402.

ErDOS, J., Alzner, E. and McNally, W., (1977), "Numerical Solution of Periodic Transonic Flow through a Fan Stage," AIAA Journal, Vol. 15, No. 11, pp. 1559-1568.

Farge, T. Z., Johnson, M. W. and Maksoud, T. M. A., (1989), "Tip Leakage in a Centrifugal Impeller," ASME Journal of Turbomachinery, Vol. 111, pp. 244-249.

Farmer, J., Martinelli, L. and Jameson, A., (1994), "Fast Multigrid Method for Solving Incompressible Hydrodynamic Problems with Free Surfaces," AIAA Journal, Volume 32, No. 6, pp. 1175-1182.



- Flaxington, D. and Swain, E., (1999), "Turbocharger Aerodynamic Design," IMechE Journal of Mechanical Engineering Science, Vol. 213, pp. 43-57.
- Fritsch, G. and Giles, M., (1995), "An Asymptotic Analysis of Mixing Loss," ASME Journal of Turbomachinery, Vol. 117, pp. 367-374.
- Giles, M. B., (1988), "Calculation of Unsteady Wake Rotor Interaction," AIAA Journal of Propulsion and Power, Vol. 4, No. 4.
- Giles, M., (1990), "Non-reflecting Boundary Conditions for Euler Equation Calculations," AIAA Journal, Vol. 28, No. 12, pp. 2050-2058.
- Glynn, D. R. and Marsh, H., (1980), "Secondary Flow in Annular Cascades," International Journal of Heat and Fluid Flow, Vol. 2, No. 1.
- Goto, A., Takemura, T. and Zangeneh, M., (1996), "Suppression of Secondary Flows in a Mixed-Flow Pump Impeller by Application of Three-Dimensional Inverse Design Method: Part 2 – Experimental Validation," ASME Journal of Turbomachinery, Vol. 118, pp. 544-551.
- Gregory-Smith, D. G., (1982), "Secondary Flows and Losses in Axial Flow Turbines," ASME Journal of Engineering for Power, Vol. 104, pp. 819-822.
- Gregory-Smith, D. G., Graves, C. P. and Walsh, J. A., (1987), "Growth of Secondary Losses and Vorticity in an Axial Turbine Cascade," ASME Paper No. 87-GT-114.
- Gulich, J. F., (1999), "Impact of Three-Dimensional Phenomena on the Design of rotordynamic pumps," IMechE Journal of Mechanical Engineering Science, Vol. 213, pp. 59-70.
- Hah, C. and Krain, H., (1990), "Secondary Flows and Vortex Motion in a High-Efficiency Backswept Impeller at Design and Off-Design Conditions," ASME Journal of Turbomachinery, Vol. 112, pp. 7-13.
- Hall, E., (1997), "Aerodynamic Modeling of Multistage Compressor Flowfields - Part 1: Analysis of Rotor/Stator/Rotor Aerodynamic Interaction," ASME Paper No. 97-GT-345.
- Hall, E., (1997), "Aerodynamic Modeling of Multistage Compressor Flowfields - Part 2: Modeling Deterministic Stresses," ASME Paper No. 97-GT-345.
- Harlow, F. H. and Welch, J. E., (1965), "Numerical Calculation of Time-



Dependent Viscous Incompressible Flow of Fluid with Free Surface," *Physics of Fluids*, Vol. 8, pp. 2182-2189.

Hashemi, S. G. R., Lemak, R. J. and Owczarek, J. A., (1984), "An Investigation of the Flow Characteristics and Losses in Radial Nozzle Cascades," *ASME Journal of Engineering for Gas Turbine and Power*, Vol. 106, pp. 502-510.

Hathaway, M. D., Wood, J. R. and Wasserbauer, C. A., (1992), "NASA Low-Speed Centrifugal Compressor for Three-Dimensional Viscous Code Assessment and Fundamental Flow Physics Research," *ASME Journal of Turbomachinery*, Vol. 114, pp. 295-303.

Hathaway, M. D., Chriss, R. M., Wood, J. R. and Strazisar, A. J., (1993), "Experimental and Computational Investigation of the NASA Low-Speed Centrifugal Compressor Flow Field," *ASME Journal of Turbomachinery*, Vol. 115, pp. 527-542.

Hathaway, M. D. and Wood, J. R., (1996), "Application of a Multi-Block Code to Investigate the Impact of Geometry Modelling on Centrifugal Compressor Flow Field Predictions," *ASME Paper No. 96-GT-372*.

Hayami, H., Senoo, Y. and Utsunomiya, K., (1990), "Application of a Low-Solidity Cascade Diffuser to Transonic Centrifugal Compressor," *ASME Journal of Turbomachinery*, Vol. 112, pp. 25-29.

He, L., (1990), "An Euler Solution for Unsteady Flows around Oscillating Blades," *ASME Journal of Turbomachinery*, Vol. 112, pp. 714-722.

He, L., (1993), "New Two-Grid Acceleration Methods for Unsteady Navier-Stokes Calculations," *AIAA Journal of Propulsion and Power*, Vol. 9, pp. 272-280.

He, L. and Denton, J. D., (1994), "Three-Dimensional Time-Marching Inviscid and Viscous Solutions for Unsteady Flows around Vibrating Blades," *ASME Journal of Turbomachinery*, Vol. 116, pp. 469-476.

He, L., (1996a), "Modelling Issues for Computation of Unsteady Turbomachinery Flows," VKI Lecture Series "Unsteady Flows in Turbomachines," March 11-15.

He, L., (1996b), "Time-Marching Calculations of Unsteady Flows, Blade Row Interaction and Blade Flutter," VKI Lecture Series "Unsteady Flows in Turbomachinery," March 11-15.

He, L., (1996c), "TF3D - A Program to Calculate Turbomachinery Flows in

Three-Dimensions (User's Guide, Version 1)."

He, L. and Ning, W., (1998), "Efficient Approach for Analysis of Unsteady Viscous Flows in Turbomachines," AIAA Journal, Vol. 36, No. 11, pp. 2005-2012.

He, L., (1999), "Three-Dimensional Unsteady Navier-Stokes Analysis of Stator-Rotor Interaction in Axial-Flow Turbines," IMechE Conference Transactions, 3rd European Conference on Turbomachinery Fluid Dynamics and Thermodynamics, Vol. A.

Hirsch, CH., (1989), "Numerical computation of Internal and External flows, Volume 1: Fundamentals of Numerical Discretization," John Wiley & Sons.

Hirsch, CH., Kang, S. and Pointel, G., (1996), "A Numerically Supported Investigation of the 3D Flow in Centrifugal Impellers, Part 1: validation base," ASME Paper No. 96-GT-151.

Hirsch, CH., Kang, S. and Pointel, G., (1996), "A Numerically Supported Investigation of the 3D Flow in Centrifugal Impellers, Part 2: Secondary Flow Structure," ASME Paper No. 96-GT-152.

Hodson, H. P., (1984), "Boundary Layer and Loss Measurements on the Rotor of an Axial-Flow Turbine," ASME Journal of Engineering for Gas Turbine and Power, Vol.106, pp. 391-399.

Huntsman, I., Hodson, H. P. and Hill, S. H., (1992), "The Design and Testing of a Radial Flow Turbine for Aerodynamic Research," ASME Journal of Turbomachinery, Vol. 114, pp. 411-418.

Huntsman, I., (1993), "An Investigation of Radial Inflow Turbine Aerodynamics," Ph.D. Thesis, Cambridge University, United Kingdom.

Inoue, M. and Cumpsty, N. A., (1984), "Experimental Study of Centrifugal Impeller Discharge Flow in Vaneless and Vaned Diffusers," ASME Journal of Engineering for Gas Turbines and Power, Vol. 106, pp. 455-467.

Issa, R. I. and Lockwood, F. C., (1977), "On the Prediction of Two-Dimensional Supersonic Viscous Interactions Near Walls," AIAA Journal, Vol. 15, No. 2, pp. 182-188.

Jameson, A., (1982), "Transonic Aerofoil Calculation using the Euler Equations," Numerical Methods in Aeronautical Fluid Dynamics, ed. Roe, P. L., Academic Press, pp.

Jameson, A., (1991), "Time Dependent Calculations Using Multigrid, with Applications to Unsteady Flows Past Airfoils and Wings," AIAA Paper No. 91-1596.

Johnson, M. W. and Moore, J., (1983), "Secondary Flow Mixing Losses in a Centrifugal Impeller," ASME Journal of Engineering for Power, Vol. 105, pp. 24-32.

Jung, A. R., Mayer, J. F. and Stetter, H., (1997), "Prediction of 3D Unsteady Flow in an Air Turbine and a Transonic Compressor Including Blade Gap Flow and Blade Row Interaction," ASME Paper 97-GT-94.

Kato, H., (1998), "Complex Structure of Sheet-Cloud Cavitation," Proceedings of Third International Conference on Pumps and Fans, Beijing.

Koya, M. and Kotake, S., (1985), "Numerical Analysis of Fully Three-Dimensional Periodic Flows through a Turbine Stage," ASME Journal of Engineering for Gas Turbines and Power, Vol. 107, pp. 945-952.

Krain, H., (1984), "A CAD Method for Centrifugal Compressor Impellers," ASME Journal of Turbomachinery, Vol. 106, pp. 482-488.

Krain, H., (1988), "Swirling Impeller Flow," ASME Journal of Turbomachinery, Vol. 110, pp. 122-128.

Kwak, D., Chang, J. L., Shanks, S. P. and Chakravarthy, S., (1986), "A Three-Dimensional Incompressible Navier-Stokes Flow Solver Using Primitive Variables," AIAA Journal, Vol. 24, pp. 390-396 .

Lighthill, M. J., (1954), "The response of Laminar Skin Friction and Heat Transfer to Fluctuations in the Stream Velocity," Proceeding of the Royal Society (London), Vol. A224.

Miner, S. M., Flack, R. D. and Allaire, P. E., (1992), "Two-Dimensional Flow Analysis of a Laboratory Centrifugal Pump," ASME Journal of Turbomachinery, Vol. 114, pp. 333-339.

Moore, J., (1973), "A Wake and an Eddy in a Rotating, Radial flow Passage, Part 1: Experimental Observations," ASME Journal of Engineering for Power, pp. 205-212.

Moore, J., (1973), "A Wake and an Eddy in a Rotating, Radial flow Passage, Part 2: Flow Model," ASME Journal of Engineering for Power, pp. 213-219.

Morreti, G. and Abbet, M., (1966), "A Time-Dependent Computational Method

for Blunt Body Flows," AIAA Journal, Vol. 4, No. 12, pp. 2136-2141.

Okiishi, T. H., Hathaway, M. and Hansen, J., (1985), "A Note on Blade Wake Interaction Influence on Compressor Stator Row Aerodynamic Performance," ASME Journal of Engineering for Gas Turbines and Power, Vol. 107, pp. 549-551.

Patankar, S. V. and Spalding, D. B., (1972), "A Calculation Procedure for Heat, Mass and Momentum Transfer in Three-Dimensional Parabolic Flows," International Journal of Heat and Mass Transfer, Vol. 15, pp. 1787-1806.

Pilipenko, V. V. and Semenov, Y. A., (1998), "On Determination of the Transfer Matrix of a Cavitating Inducer Centrifugal Pump," Proceedings of Third International Conference on Pumps and Fans, Beijing.

Poensgen, C. and Gallus, H., (1991), "Three-Dimensional Wake Decay inside of a Compressor Cascade and its Influence on the Downstream Unsteady Flow Field: Part 1 - Wake Decay Characteristics in the Flow Passage," ASME Journal of Turbomachinery, Vol. 113, pp. 180-189.

Poensgen, C. and Gallus, H., (1991), "Three-Dimensional Wake Decay inside of a Compressor Cascade and its Influence on the Downstream Unsteady Flow Field: Part 2 - Unsteady Flow Field Downstream of the Stator," ASME Journal of Turbomachinery, Vol. 113, pp. 190-197.

Qian, Y. and Arakawa, C., (1998), "The Development of CFD Technology in Hydraulic Machinery," Proceedings of Third International Conference on Pumps and Fans, Beijing.

Rai, M. M., (1985), "Navier-Stokes Simulations of Rotor-Stator Interaction using Patched and Overlaid Grids," AIAA Paper No. 85-1519.

Rai, M. M., (1987), "Unsteady Three-Dimensional Navier-Stokes Simulations of Turbine Rotor-Stator Interaction," AIAA Paper No. 87-2058.

Rhie, C. M., Gleixner, A. J., Spear, D. A., Fischberg, C. J. and Zacharias, R. M., (1998), "Development and Application of a Multistage Navier-Stokes Solver: Part 1 - Multistage Modelling using Bodyforces and Deterministic Stresses," ASME Journal of Turbomachinery, Vol. 120, pp.205-214.

Rizzi, A. and Eriksson, L. F., (1985), "Computation of Inviscid Incompressible Flow with Rotation," Journal Fluid Mechanics, Vol. 153, pp. 275-312.

Rogers, S. E. and Kwak, D., (1990), "Upwind Differencing Scheme for the Time-Accurate Incompressible Navier-Stokes Equations," AIAA Journal, Vol. 28, No. 2, pp. 253-262.

Rogers, C., (1996), "Development of a High Specific Speed Centrifugal Compressor," ASME Paper 96-GT-353.

Sato, K. and He, L., (1999), "Effect of Rotor-Stator Interaction on Impeller Performance in Centrifugal Compressors," International Journal of Rotating Machinery, Vol. 5, No. 2.

Schulz, H. D., Gallus, H. E. and Lakshminarayana, B., (1990), "Three-Dimensional Separated Flow Field in the Endwall Region of an Annular Compressor Cascade in the Presence of Rotor-Stator Interaction: Part 1 - Quasi-Steady Flow Field and Comparison With Steady-State Data," ASME Journal of Turbomachinery, Vol. 112, pp.669-678.

Schulz, H. D., Gallus, H. E. and Lakshminarayana, B., (1990), "Three-Dimensional Separated Flow Field in the Endwall Region of an Annular Compressor Cascade in the Presence of Rotor-Stator Interaction: Part 2 - Unsteady Flow and Pressure Field," ASME Journal of Turbomachinery, Vol. 112, pp.679-690.

Sedlar, M. and Mensik, P., (1999), "Investigation of Rotor-Stator Interaction Influence on Flow Fields in Radial Flow Pumps," IMechE C557/083/99.

Smith, L. (1966), "Wake dispersion in turbomachines," Journal of Basic Engineering, ASME Transactions, Vol. 88, No. 3.

Smith, L. H., (1970), "Casing Boundary Layer in Multistage Axial-Flow Compressors," Flow Research on Blading, L.S. Dzung ed., Elsevier Publishing Company.

Shyy, W., Chen, M. and Sun, C., (1992), "Pressure-Based Multigrid Algorithm for Flow at All Speeds," AIAA Journal, Vol. 30, No. 11, pp. 2660-2669.

Sieverding, C. H., (1985), "Recent Progress in the Understanding of Basic Aspects of Secondary flows in Turbine Blade Passages," ASME Journal of Engineering for Gas Turbine and Power, Vol. 107, pp. 248-257.

Takemura, T. and Goto, A., (1996), "Experimental and Numerical study of Three-Dimensional Flows in a Mixed-Flow Pump Stage," ASME Journal of Turbomachinery, Vol.118, pp. 552-561.

Tamaki, H., Nakao, H. and Saito, M., (1999), "The Experimental Study of Matching Between Centrifugal Compressor Impeller and Diffuser," ASME Journal of Turbomachinery, Vol. 121, pp. 113-118.

Turkel, E., (1987), "Preconditioned Methods for Solving the Incompressible and Low Speed Compressible Equations," Journal of Computational Physics, Vol. 72, pp. 277-298.

Ubaldi, M., Zunino, P., Barigozzi, G. and Cattanei, A., (1996), "An Experimental Investigation of Stator Induced Unsteadiness on Centrifugal Impeller Outflow," ASME Journal of Turbomachinery, Vol. 118, pp. 41-54.

Valkov, T. V. and Tan, C. S., (1998), "Effect of Upstream Rotor Vortical Disturbances on the Time Averaged Performance of Axial Compressor Stators: Part 1 - Framework of Technical Approach and Wake-Stator Blade Interactions," ASME Paper No. 98-GT-312.

Valkov, T. V. and Tan, C. S., (1998), "Effect of Upstream Rotor Vortical Disturbances on the Time Averaged Performance of Axial Compressor Stators: Part 2 - Rotor Tip Vortex/Streamwise Vortex-Stator Blade Interactions," ASME Paper No. 98-GT-313.

Van Zante, D. E., Adamczyk, J. J. and Okiishi, T. H., (1997), "Wake Recovery Performance Benefit in a High-Speed Axial Compressor," ASME Paper No. 97-GT-535.

Vu, T. C. and Shyy, W., (1994), "Performance Prediction by Viscous Flow Analysis for Francis Turbine Runner," ASME Journal of Fluid Engineering, Vol. 116, pp. 116-120.

Walker, P. J. and Dawes, W. N., (1990), "The Extension and Application of Three-Dimensional Time-Marching Analyses to Incompressible Turbomachinery Flows," ASME Journal of Turbomachinery, Vol. 112, pp. 385-390.

Watanabe, I., Ariga, I. and Mashino, T., (1971), "Effect of Dimensional Parameters of Impellers on Performance Characteristics of a Radial Inflow Turbine," ASME Journal of Engineering for Power, Vol. 93, pp. 81-102.

Weiss, J. M. and Smith, W. A., (1995), "Preconditioning Applied to Variable and Constant Density Flows," AIAA Journal, Vol. 33, No. 11, pp. 2050-2057.

Whitfield, A. and Baines, N. C., (1990), "Design of Radial Turbomachines,"

Longman Scientific & Technical.

Yamaguchi, K. and Nagashima, T., (1996), "Experimental Study of Centrifugal Impeller/Diffuser Interaction for Transonic Discharge Rates," Proceedings of 3rd International Symposium on Aerothermodynamics of Internal Flows, Beijing.

Yamane, T. and Nagashima, T., (1998), "High Speed Centrifugal Impeller and Diffuser Interaction Near Stall Conditions," Proceedings of the 8th International Symposium on Unsteady Aerodynamics and Aeroelasticity of Turbomachines, Stockholm.

Zangeneh, M., (1994), "Inviscid-Viscous Interaction Method for Three-Dimensional Inverse Design of Centrifugal Impellers," ASME Journal of Turbomachinery, Vol. 116, pp. 280-290.

Zangeneh, M., Goto, A. and Takemura, T., (1996), "Suppression of Secondary Flows in a Mixed-Flow Pump Impeller by Application of Three-Dimensional Inverse Design Method: Part 1 – Design and Numerical Validation," ASME Journal of Turbomachinery, Vol. 118, pp. 536-543.

Zangeneh, M., Goto, A. and Harada, H., (1999), "On the Role of Three-Dimensional Inverse Design Methods in Turbomachinery Shape Optimization," IMechE Journal of Mechanical Engineering Science, Vol. 213, pp. 27-42.

## Appendix 1

### Absolute Flow Angle in Radial Passage

The purpose of this appendix is to provide an idea about the change in the absolute flow angle in the radial passage. Simplest form of approximated tangential velocity distribution in the radial direction is given by neglecting the viscous force and the flow non-uniformity (Whitfield and Baines 1990). From the conservation of the angular momentum, the tangential velocities in two different radial locations indicated by the number 1 and 2 are related with the following equation,

$$\dot{m}(r_2 C_{\theta 2} - r_1 C_{\theta 1}) = \tau = 0 \quad \text{eq. A1-1}$$

where  $r$  is the radial location,  $C_{\theta}$  is the tangential velocity and  $\tau$  denotes the torque exerted on the fluid between  $r_1$  and  $r_2$  which is zero in this case. The continuity equation in the radial configuration is described as,

$$\rho_1 C_{r1} \cdot 2\pi r_1 \cdot b_1 = \rho_2 C_{r2} \cdot 2\pi r_2 \cdot b_2 \quad \text{eq. A1-2}$$

where  $\rho$ ,  $C_r$ , and  $b$  are the density of fluid, the radial velocity component and the passage height at the radial location suggested by the subscript number. Combining these equations gives the relation of the velocity components as,

$$\frac{1}{\rho_1 b_1} \frac{C_{\theta 1}}{C_{r1}} = \frac{1}{\rho_2 b_2} \frac{C_{\theta 2}}{C_{r2}} \quad \text{eq. A1-3}$$

and this can be rewritten with respect to the absolute flow angles as

$$\tan \alpha_2 = \frac{\rho_2 b_2}{\rho_1 b_1} \tan \alpha_1 \quad \text{eq. A1-4}$$

Under the assumption of the incompressible flow in the parallel wall diffuser, equation A1-4 suggests that the flow angle remains constant and the flow particles follow logarithmic spiral. It is also known that density increase or diverged endwalls results in the increase of the flow angle toward downstream.



## Appendix 2

### Angle of Wake Lines in Radial Flow Passage

This appendix describes the movement of the wake fluid discharged from the centrifugal impeller in the radial vane-less diffuser passage. The flow angle between the impeller wake line and the radial direction is equivalent to the flow angle observed in the relatively rotating frame. Consequently, the change in the angle of the wake lines can be estimated by looking at the mass and angular momentum conservation as in Appendix 1.

From the angular momentum conservation,

$$\dot{m}(r_2 W_{\theta 2} - r_1 W_{\theta 1}) = \tau \quad \text{eq. A2-1}$$

where  $W_{\theta}$  is the relative tangential velocity in the rotating frame and  $\tau$  describes the torque exerted on the fluid through the transport from  $r_1$  to  $r_2$ . Due to the relative rotation of the impeller frame, the fluid is under the influence of the coriolis acceleration so that the angular momentum tends to increase in the direction opposite to the impeller rotation. The torque due to the coriolis acceleration between  $r_1$  and  $r_2$  is calculated as,

$$\tau_c = \int_{r_1}^{r_2} \dot{m}(r \cdot 2\omega W_r) \frac{\partial r}{W_r} = \dot{m} \cdot \omega (r_2^2 - r_1^2) \quad \text{eq. A2-2}$$

where  $\omega$  is the angular velocity of the rotation and  $W_r$  describes the radial velocity component of the relative flow. Under the inviscid flow assumption, the angular momentum equation is written as,

$$r_2 W_{\theta 2} - r_1 W_{\theta 1} = \omega (r_2^2 - r_1^2) \quad \text{eq. A2-3}$$

This equation gives the relative tangential velocity change in the radial diffuser.

Now let us look at the angle change of a wake line under the condition of the constant radial velocity component. Considering a infinitesimal radius change  $\delta r$  and the corresponding change in the wake line angle  $\delta\beta$ , and describing the relative tangential velocity as  $W_{\theta} = W_r \tan \beta$ , the equation is rewritten as,

$$(r + \delta r) W_r \tan(\beta + \delta\beta) - r W_r \tan(\beta) = \omega ((r + \delta r)^2 - r^2) \quad \text{eq. A2-4}$$

Under the assumption of ( $\delta\beta \ll \pi/2$ ), the equation yields,

$$\frac{\delta\beta}{\delta r} = \frac{2r \frac{\omega}{W_r} - \tan(\beta)}{r(1 + \tan^2(\beta))} = \frac{1}{r(1 + \tan^2(\beta))} \left( 2 \frac{r\omega}{W_r} - \frac{W_\theta}{W_r} \right) \quad \text{eq. A2-5}$$

The relative tangential velocity component is usually smaller than the speed of the impeller rotation so that the equation suggests that angle  $\beta$  will increase under the constant radial velocity condition.

## Appendix 3

### Wake Length in Radial Flow Passage

A radial flow passage inherently involves the passage expanding in the circumferential direction. This unique feature differentiates the mechanism of the wake flow attenuation in the diffuser of centrifugal compressors from its axial counterparts. This feature is illustrated in figure A3-1 of a radially discharged flow from a centrifugal impeller blade at a certain time instant  $t$  and a time after a small time interval  $\Delta t$ . The lines T1 and T2 indicate the trajectories of the fluid particles, and the distance AC is the wake segment bounded between them at time  $t$ . After time interval  $\Delta t$ , the wake fluid segment AC moves to A'C'. Generally, the length of the wake segment will not be conserved. The change in the wake length can be estimated with a geometric model described with two triangles as depicted in figure A3-1.

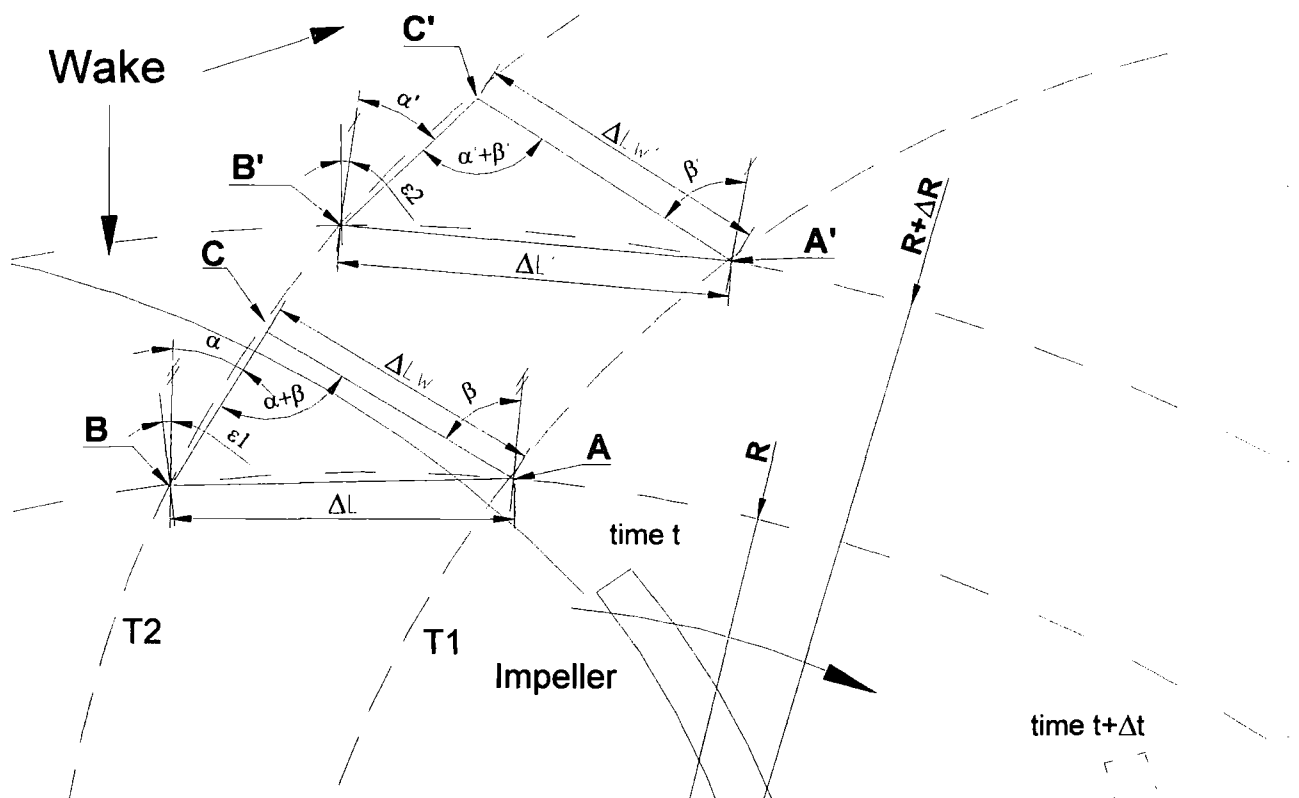


Figure A3-1 Schematic of a wake flow motion in a radial passage

Under the assumption that the distance between these flow paths T1 and T2 is sufficiently small, the length of the wake segment between AC can be approximated with a straight line  $\Delta L_w$ . The fluid particle at point B on the trajectory T2 is located at the

same radius  $R$  as point  $A$ , and distance  $AB$  is approximated as  $\Delta L$ . After the time interval of  $\Delta t$ , the fluid particles at points  $A$ ,  $B$  and  $C$  move to points  $A'$ ,  $B'$ , and  $C'$  where the lengths  $\Delta L_w'$  and  $\Delta L'$  are the distance  $A'C'$  and  $A'B'$ , respectively. The radial distance between  $A$  and  $A'$  is  $\Delta R$ . Here, it is assumed that the radius  $R$  is much larger than  $\Delta L$  so that radial lines are almost parallel ( $\epsilon_1, \epsilon_2 \approx 0$ ). Comparing the triangles formed by the points  $ABC$  and  $A'B'C'$ , and from the sine rule, the following relation is given,

$$\frac{\Delta L_w'}{\Delta L_w} = \frac{\Delta L' \sin(90 - \alpha') \sin(\alpha + \beta)}{\Delta L \sin(90 - \alpha) \sin(\alpha' + \beta')} \quad \text{eq. A3-1}$$

Since the length of the circumferential arc is inversely proportional to the radius, the equation can be rewritten as,

$$\frac{\Delta L_w'}{\Delta L_w} = \left(1 + \frac{\Delta R}{R}\right) \frac{\cos \alpha' \sin(\alpha + \beta)}{\cos \alpha \sin(\alpha' + \beta')} \quad \text{eq. A3-2}$$

Under the incompressible flow assumption in a parallel endwall diffuser, the fluid particles follow a logarithmic spiral trajectory with a constant flow angle  $\alpha$ . On the other hand, the angle of the wake tends to increase due to the coriolis acceleration in the relative frame. If the sum of the angles  $\alpha + \beta$  is greater than  $\pi/2$ , the equation A3-2 suggests that the wake segment will always be stretched. On the other hand, if the angle  $\alpha + \beta$  is less than  $\pi/2$ , whether the wake segment will be stretched or compressed is determined by the relative influences of the changes in the radius  $R$  and the flow angle  $\beta$ . For the current centrifugal compressors used, the effect of the density change is cancelled by the effect of the converging meridional profiles, and the flow angle  $\alpha$  is kept almost constant in the vaneless space. Therefore, it is possible to apply the equation A3-2 to the current configuration. Since the angle  $\alpha + \beta$  is greater than  $\pi/2$ , the wake line is stretched in the vaneless space.

## Appendix 4

### Entropy in Incompressible Substances

This appendix describes the definition of the entropy change for the incompressible substances adopted in the current research. The fundamental differential equation is,

$$T\Delta s = \Delta h - \frac{\Delta p}{\rho} \quad \text{eq. A4-1}$$

where  $s$ ,  $h$ ,  $T$  and  $p$  suggest the entropy, enthalpy, temperature and pressure of the fluid, respectively. Equation A4-1 states that the entropy change is evaluated by calculating the static enthalpy change and the static pressure change.

The static pressure change is given directly from the numerical flow solutions.

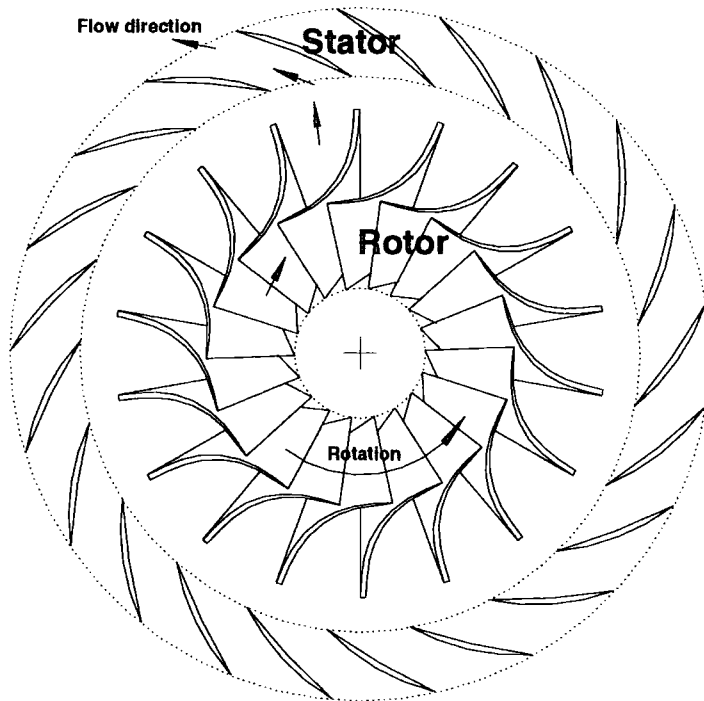
The static enthalpy change is estimated under the steady adiabatic flow assumption. The rothalpy (stagnation enthalpy for stationary components) is defined as,

$$I = h + \frac{1}{2}W^2 - \frac{1}{2}(r\omega)^2 \quad \text{eq. A4-2}$$

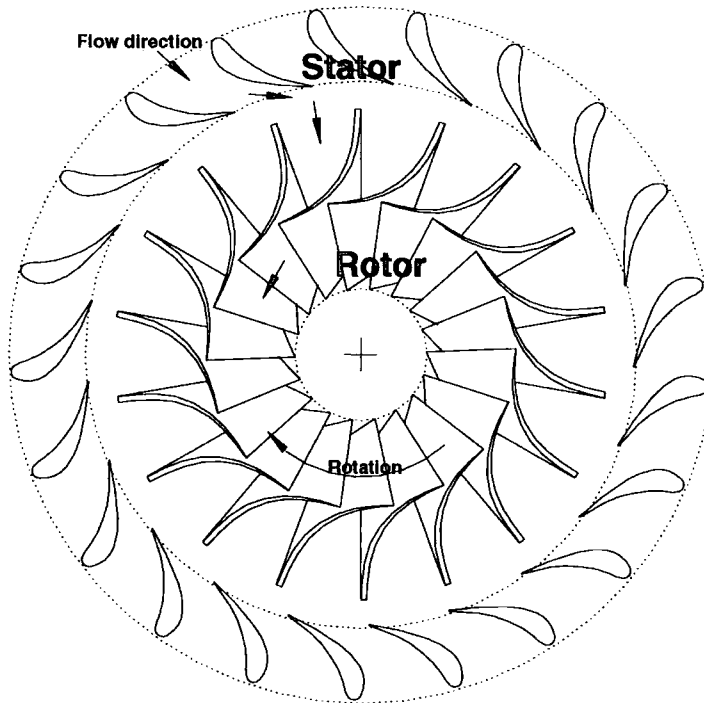
where  $W$  is the relative flow velocity and  $r$  and  $\omega$  denote the local radius and the rotation speed respectively. When  $\omega = 0$ , the definition of the rothalpy is equivalent to the relative stagnation enthalpy.

Since the rothalpy is conserved along the flow path, the static enthalpy change is calculated by taking the difference in the second and third terms on the right hand side in equation A4-2 as,

$$\Delta h = \Delta \left( \frac{1}{2}(r\omega)^2 - \frac{1}{2}W^2 \right) \quad \text{eq. A4-3}$$



(a) Compressor



(b) Turbine

**Figure 1-1 Radial turbomachine with stator**

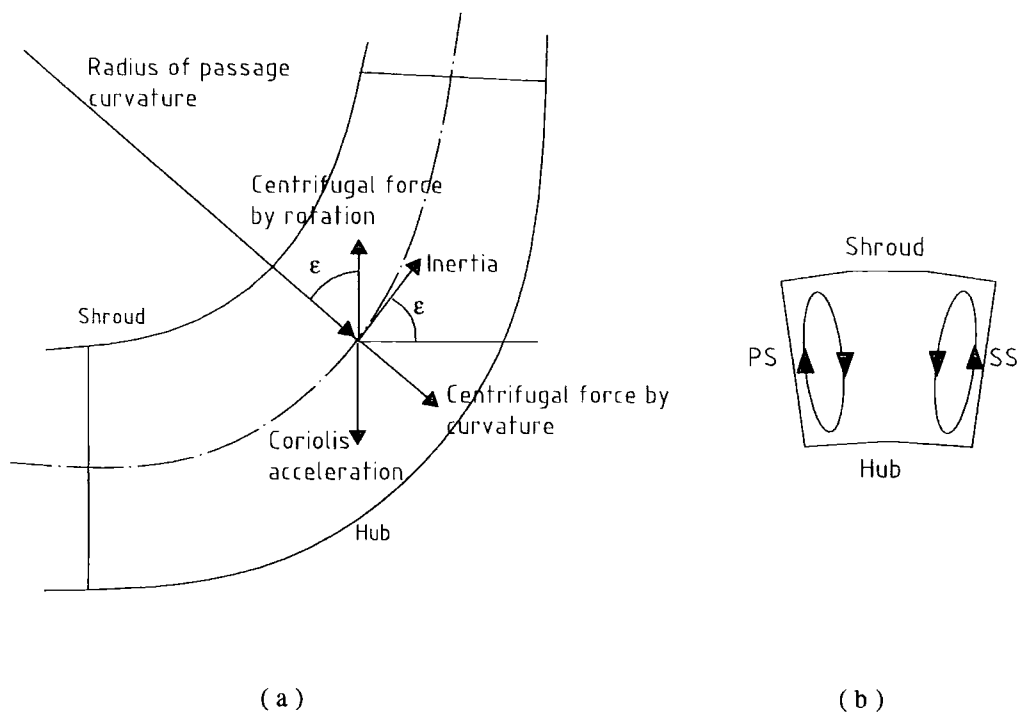


**Figure 1-2 Formation of streamwise vortices on blade surfaces**

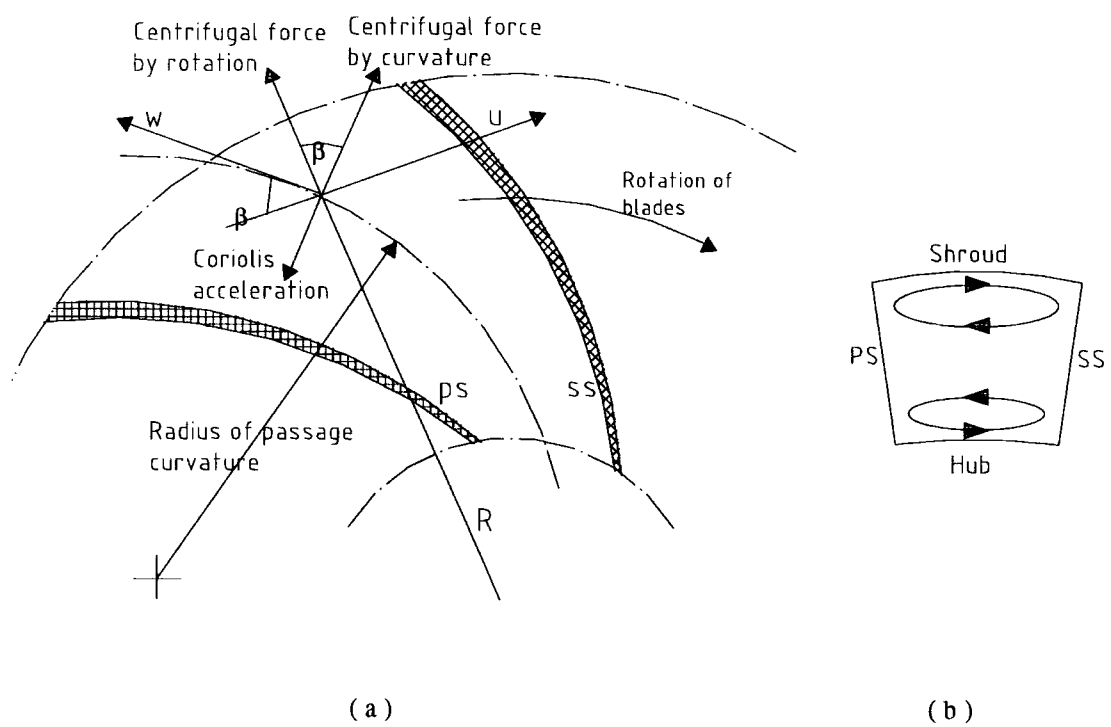
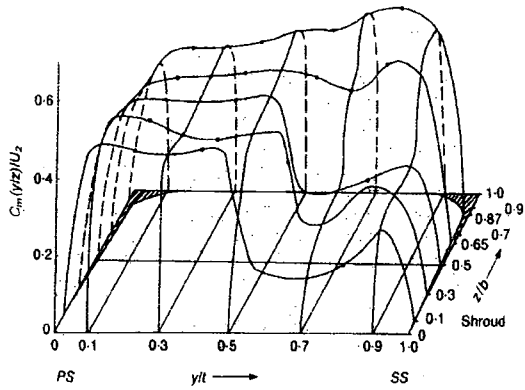
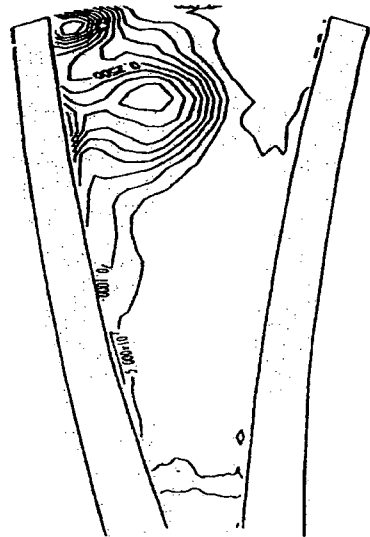


**Figure 1-3 Formation of streamwise vortices on endwalls**



(a)



(b)

**Figure 1-4 Flow non-uniformity in radial turbomachines  
(a: Eckardt 1976, b: Huntsman 1993)**

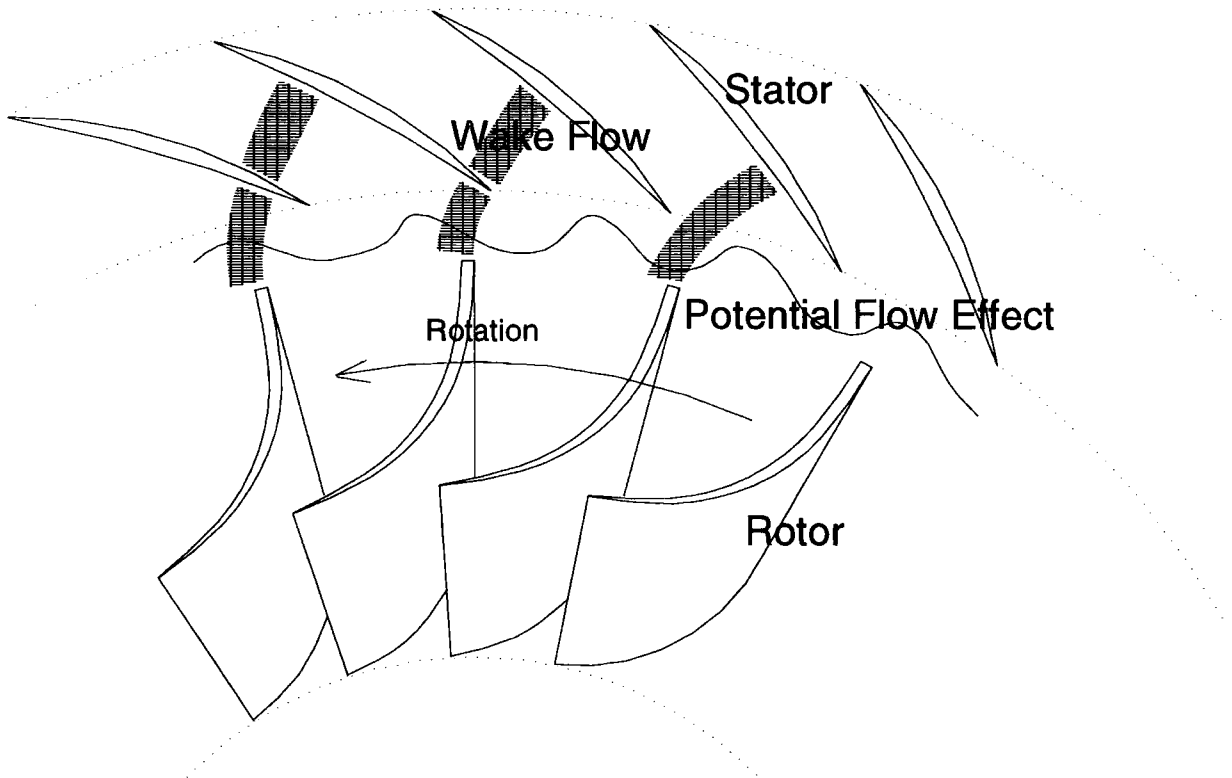


**Figure 1-5 Blade row interaction in turbomachines**



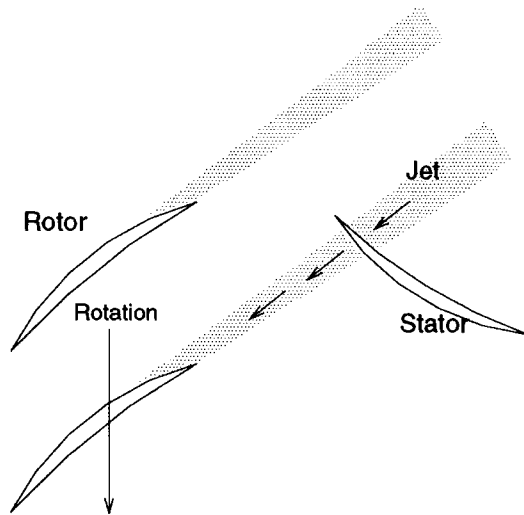


**Figure 2-1 Blade row interaction (wake and blade surface)**

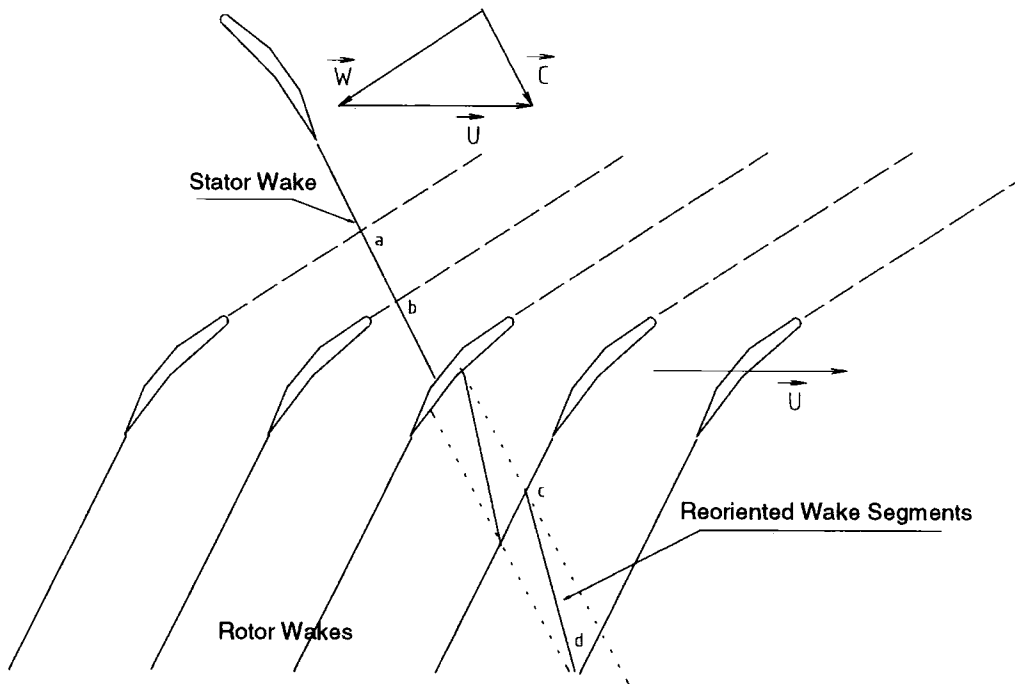


**Figure 2-2 Blade row interaction (wake chopping)**

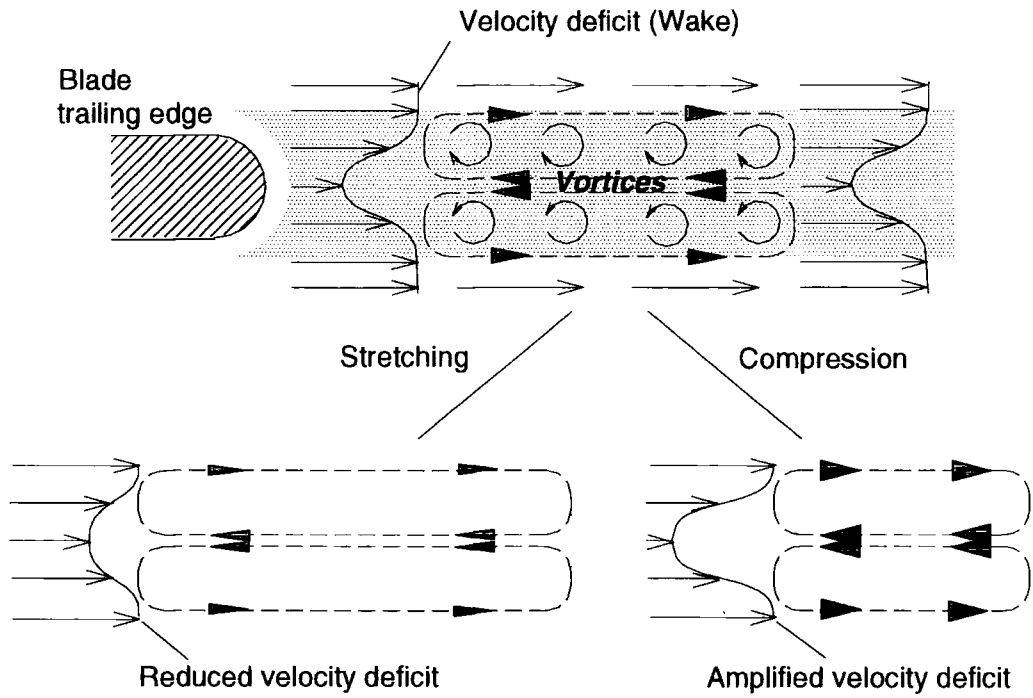


**Figure 2-3 Velocity deficit in wake flow (by Kelvin's theorem)**

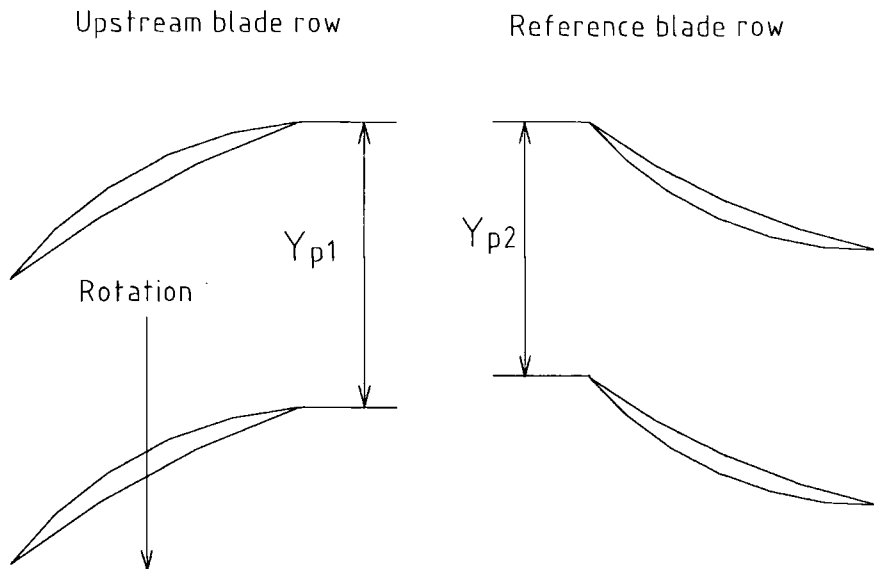


**Figure 2-4 Phase difference between neighbouring blades**

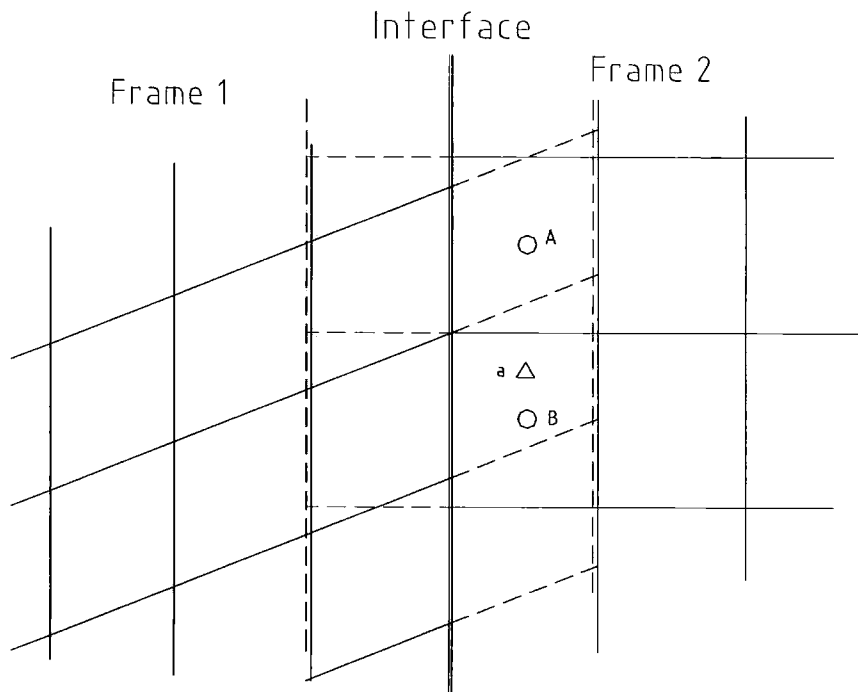


**Figure 3-1 Sliding interface treatment**

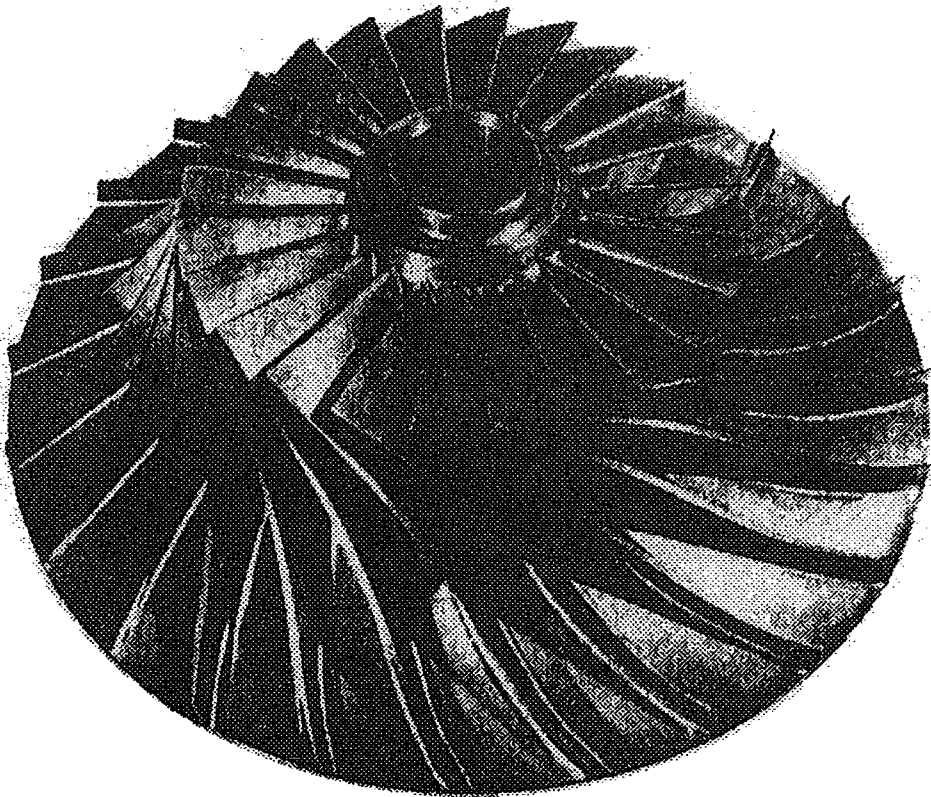


**Figure 4-1 Krain's centrifugal impeller**

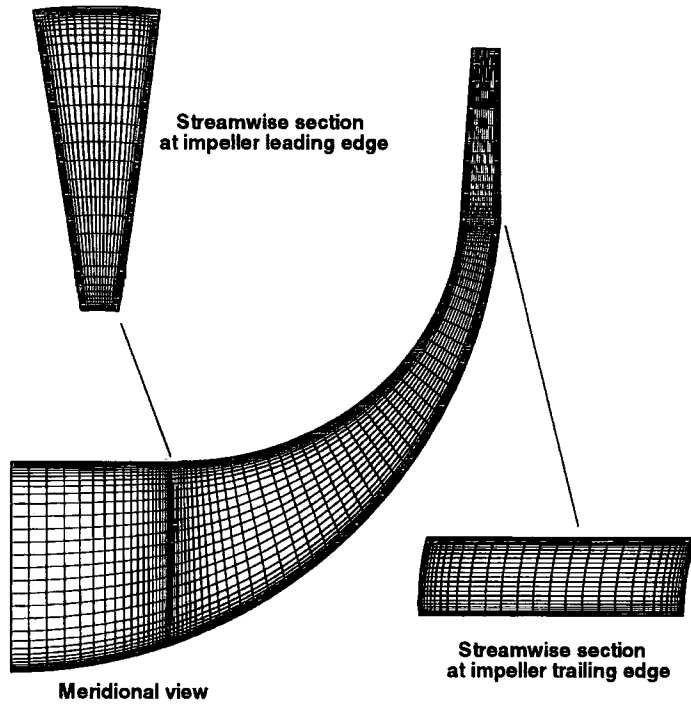


**Figure 4-2 Computational mesh F**

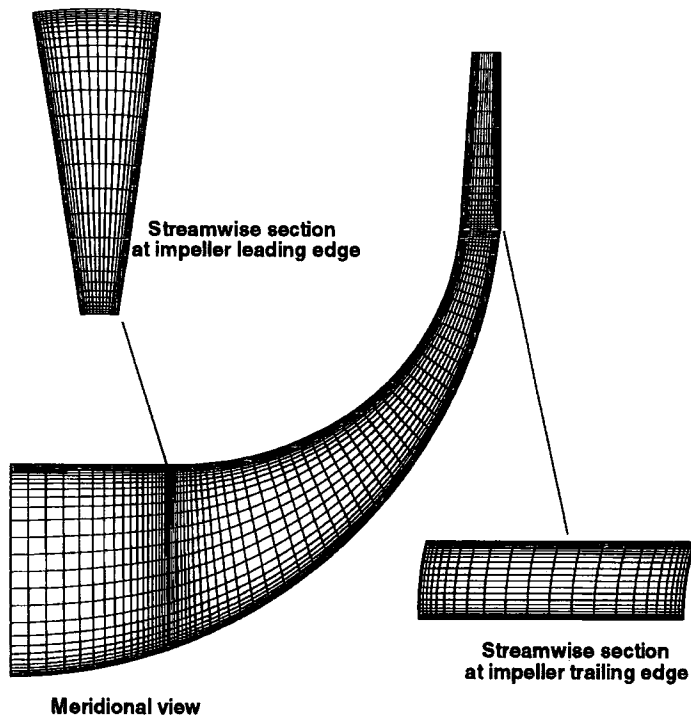


**Figure 4-3 Computational mesh C**

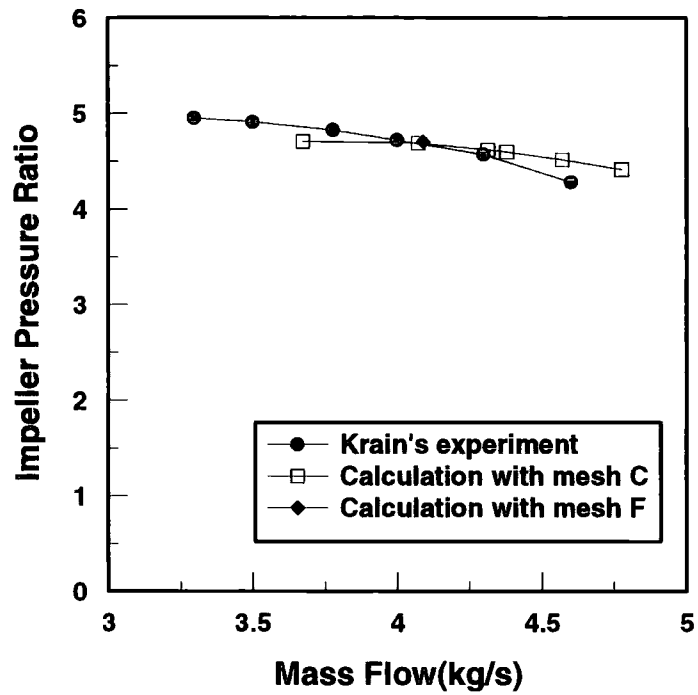


Figure 4-4 Comparison of calculated absolute pressure ratio with experimental data

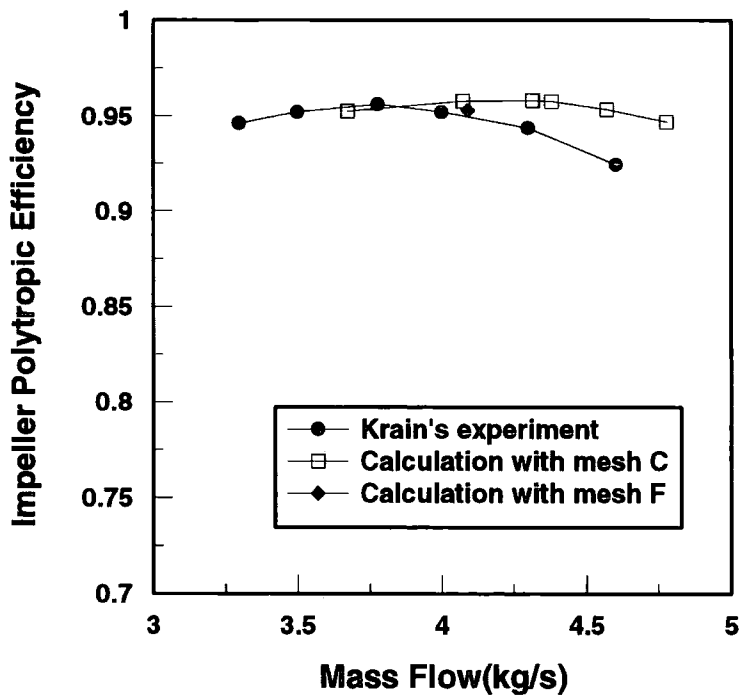


Figure 4-5 Comparison of calculated impeller polytopic efficiency with experimental data

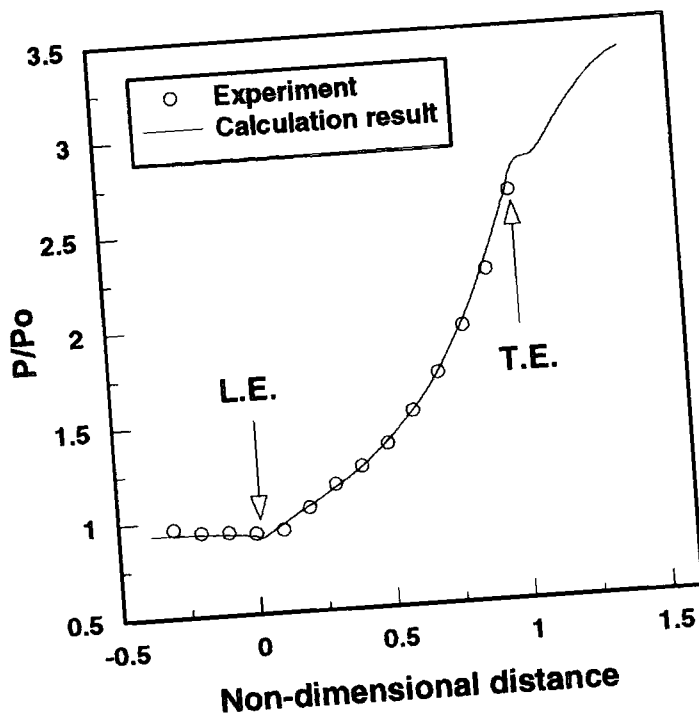


Figure 4-6 Comparison of calculated shroud static pressure distribution with experimental data

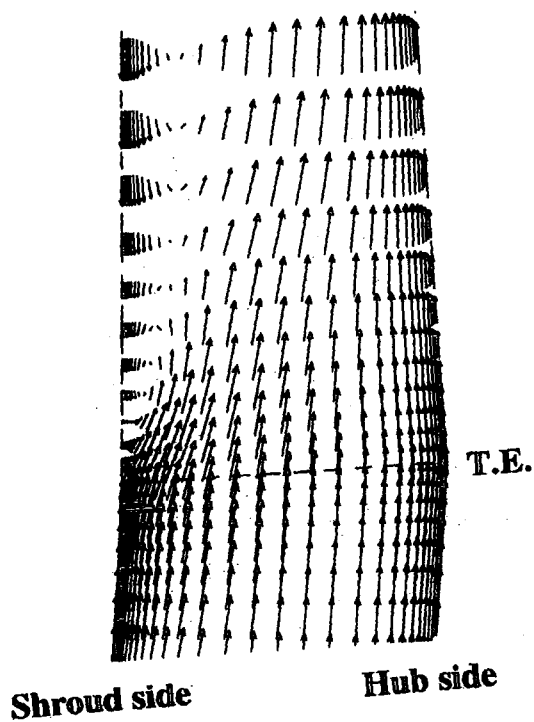
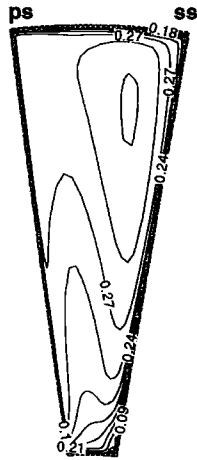
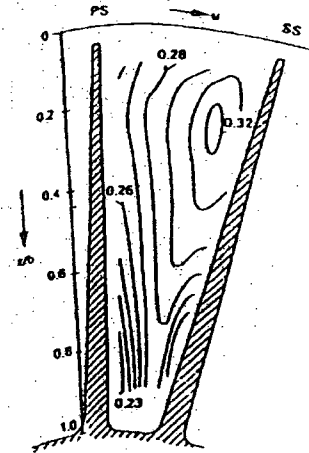


Figure 4-7 Flow vector map near the impeller trailing edge in a meridional section at mid span

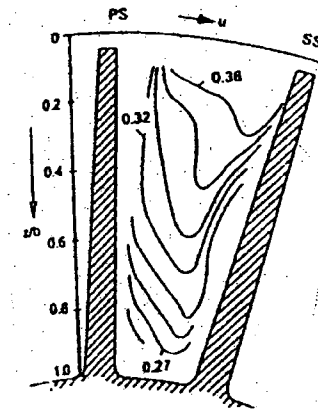
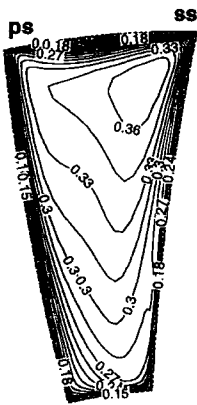
**Calculation**



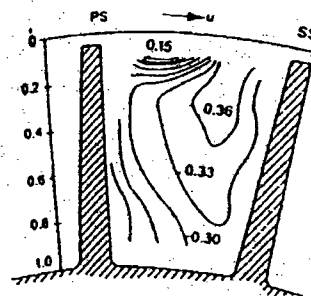
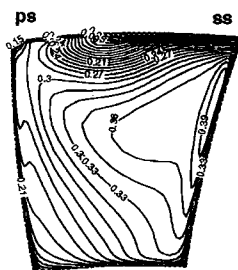
**Experiment**



0% chord section ( a )



20% chord section ( b )



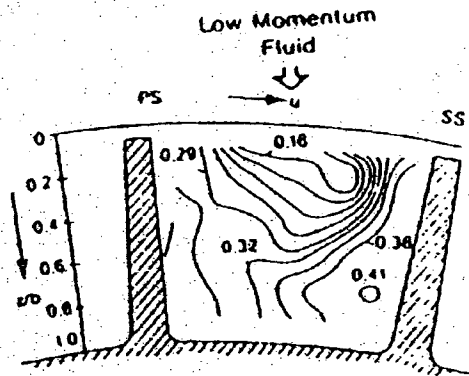
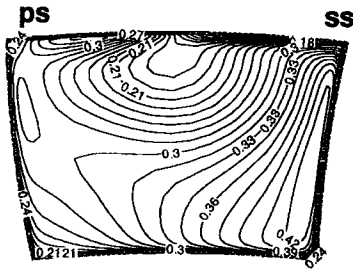
40% chord section ( c )

**Figure 4-8 Comparison of calculated meridional velocity contours with experimental data through the impeller passage**

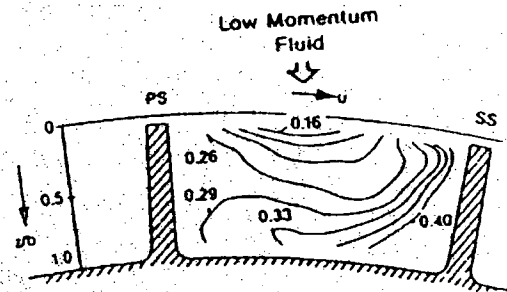
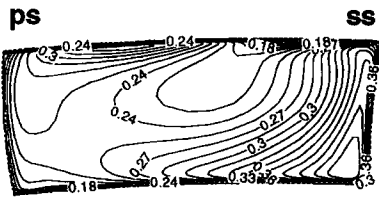


**Calculation**

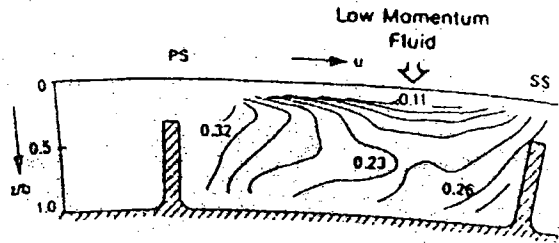
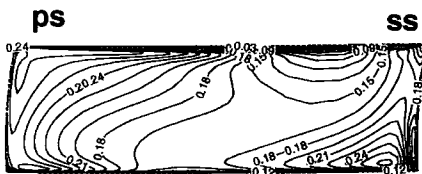
**Experiment**



60% chord section ( d )



80% chord section ( e )

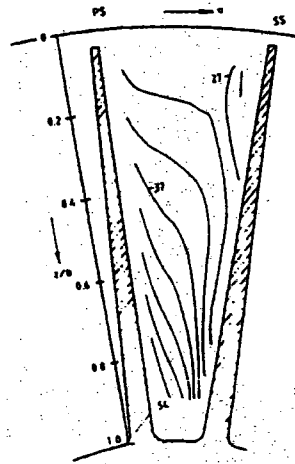
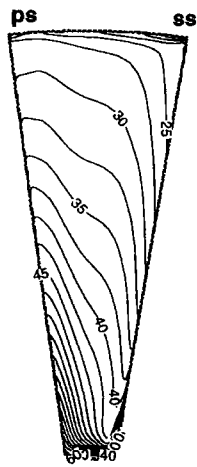


100% chord section ( f )

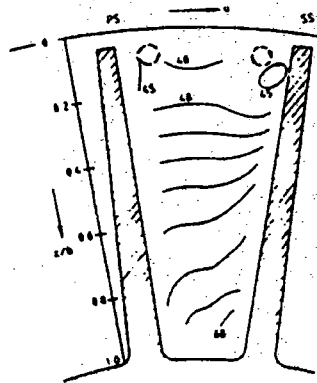
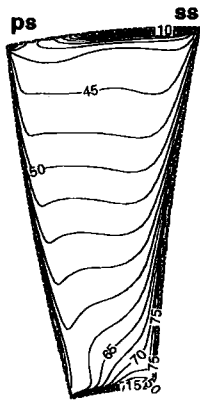
**Figure 4-8 Comparison of calculated meridional velocity contours with experimental data through the impeller passage (continue)**

**Calculation**

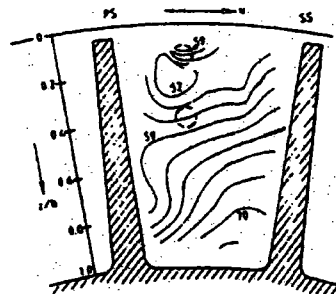
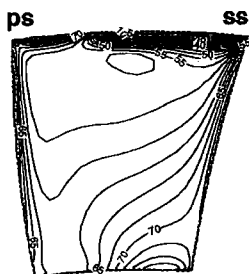
**Experiment**



0% chord section ( a )



20% chord section ( b )

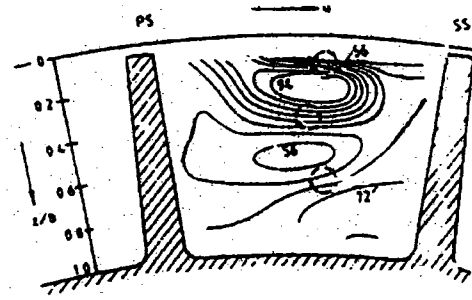
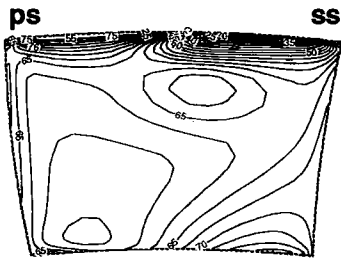


40% chord section ( c )

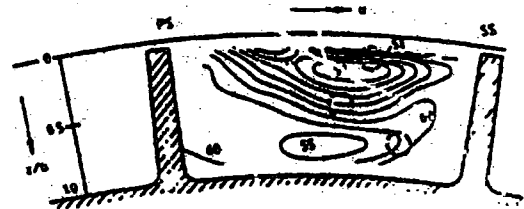
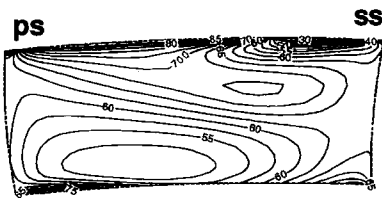
**Figure 4-9 Comparison of calculated pitchwise flow angle contours with experimental data through the impeller passage**

**Calculation**

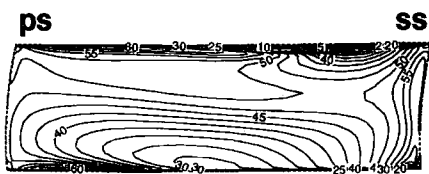
**Experiment**



60% chord section ( d )

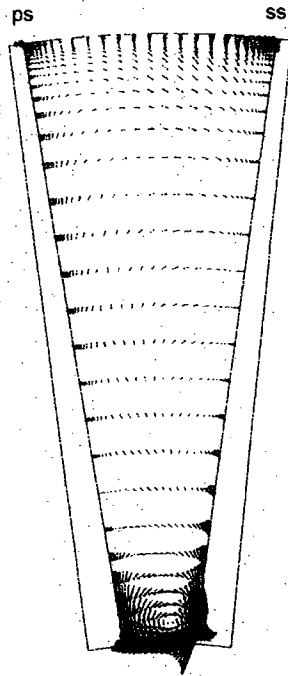


80% chord section ( e )

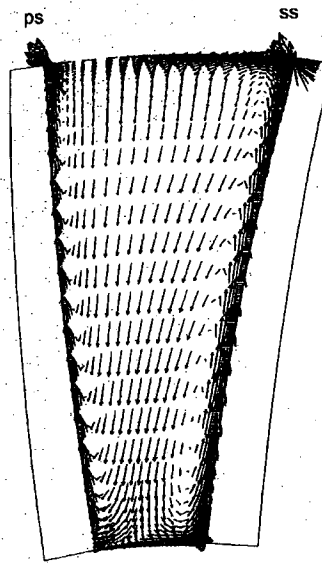


100% chord section ( f )

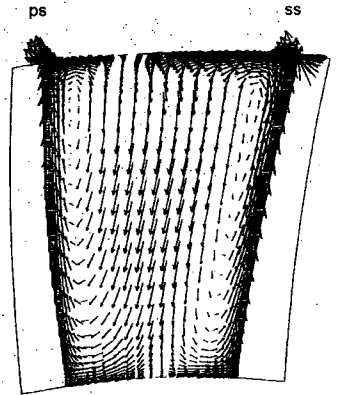
**Figure 4-9 Comparison of calculated pitchwise flow angle contours with experimental data through the impeller passage (continue)**



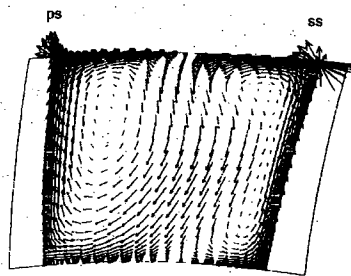
0% section ( a )



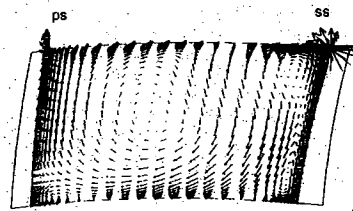
20% section ( b )



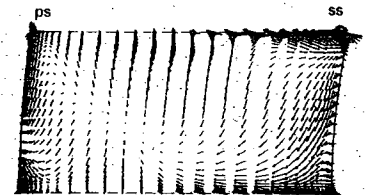
40% section ( c )



60% section ( d )

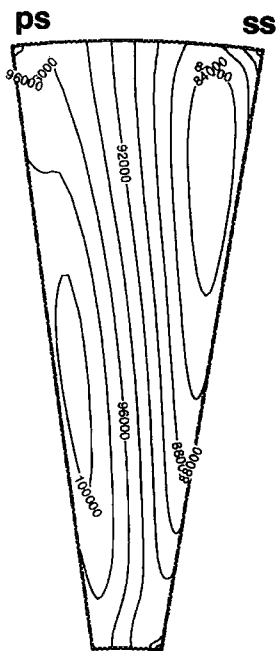


80% section ( e )

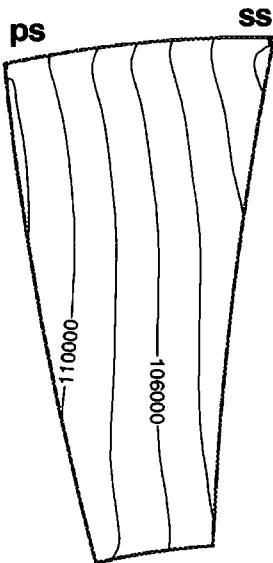


100% section ( f )

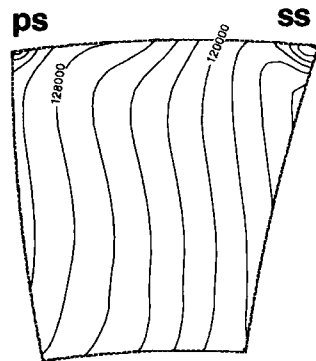
**Figure 4-10 Calculated secondary flow vectors through the impeller passage**



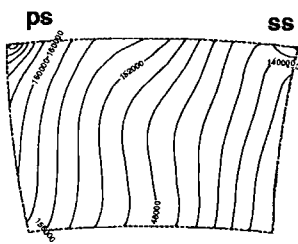
0% section ( a )



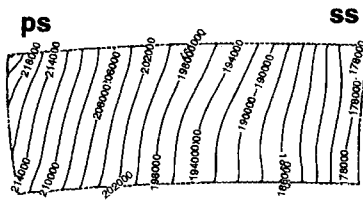
20% section ( b )



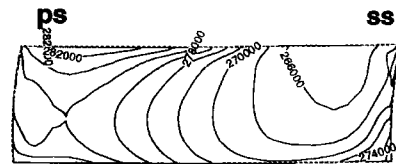
40% section ( c )



60% section ( d )



80% section ( e )



100% section ( f )

**Figure 4-11 Calculated static pressure contours through the impeller passage**



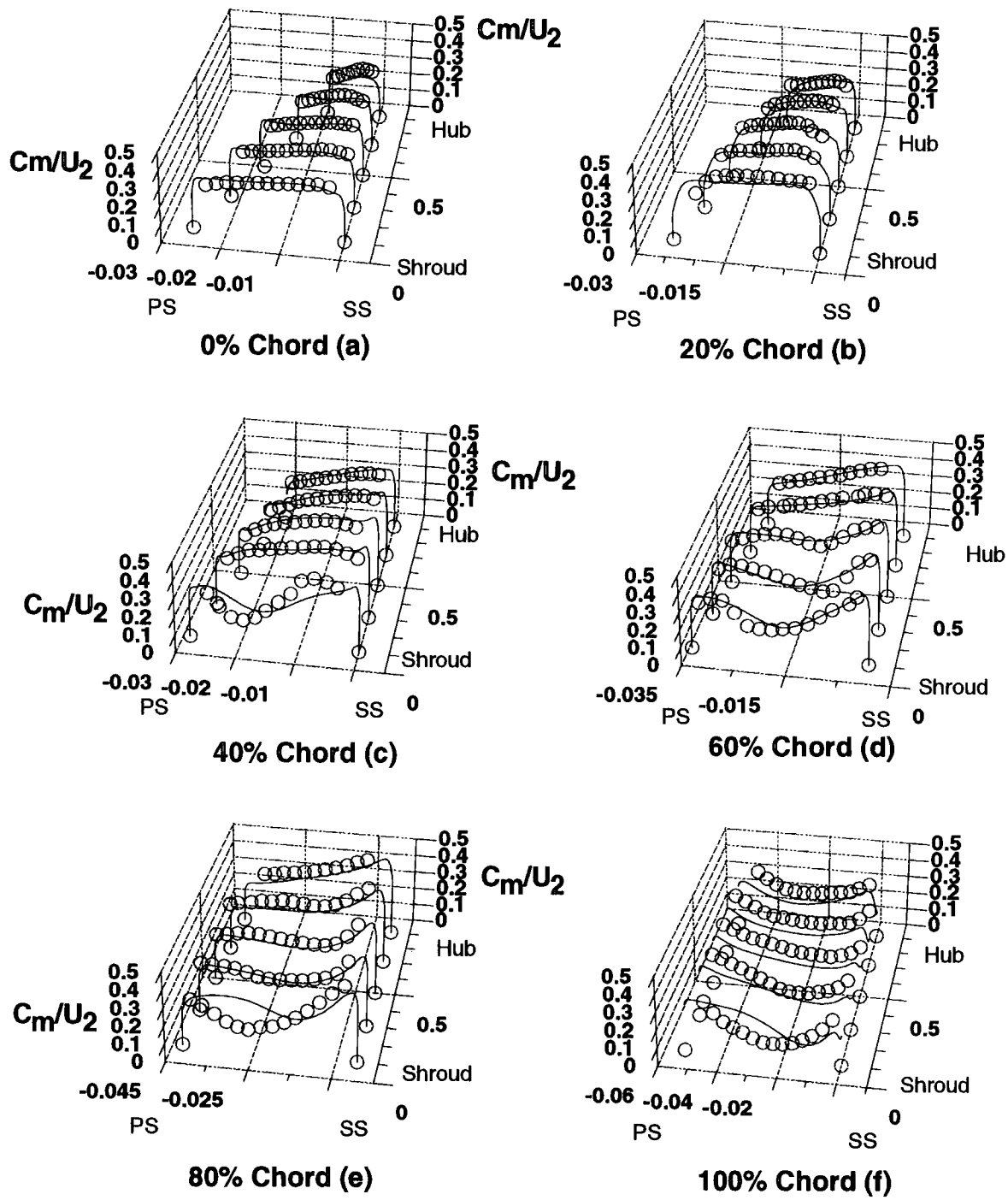


Figure 4-13 Comparison of meridional velocity profiles through the impeller passage (lines: computation, circles: experiment)

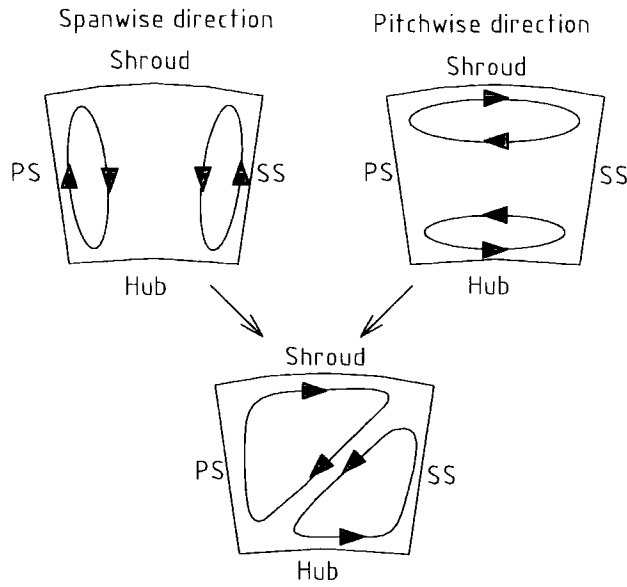


Figure 4-14 Model of streamwise vortices (Gülich 1999)

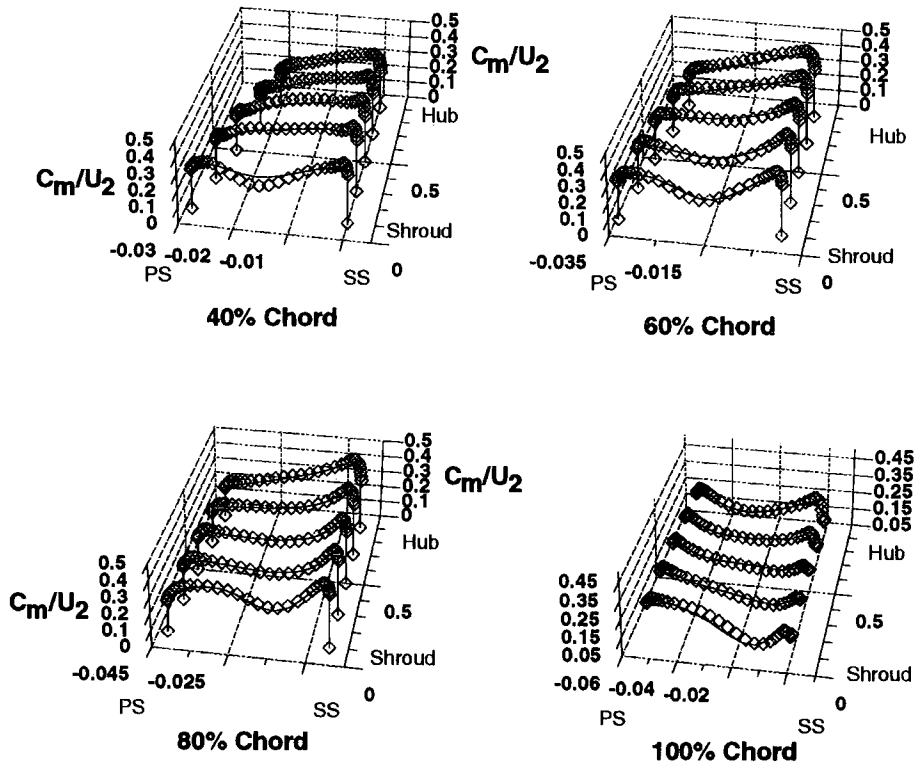


Figure 4-15 Comparison of meridional velocity profiles between the mesh F (square symbols) and the mesh C (solid lines)



1% tip gap (reference)

No tip gap

3% tip gap

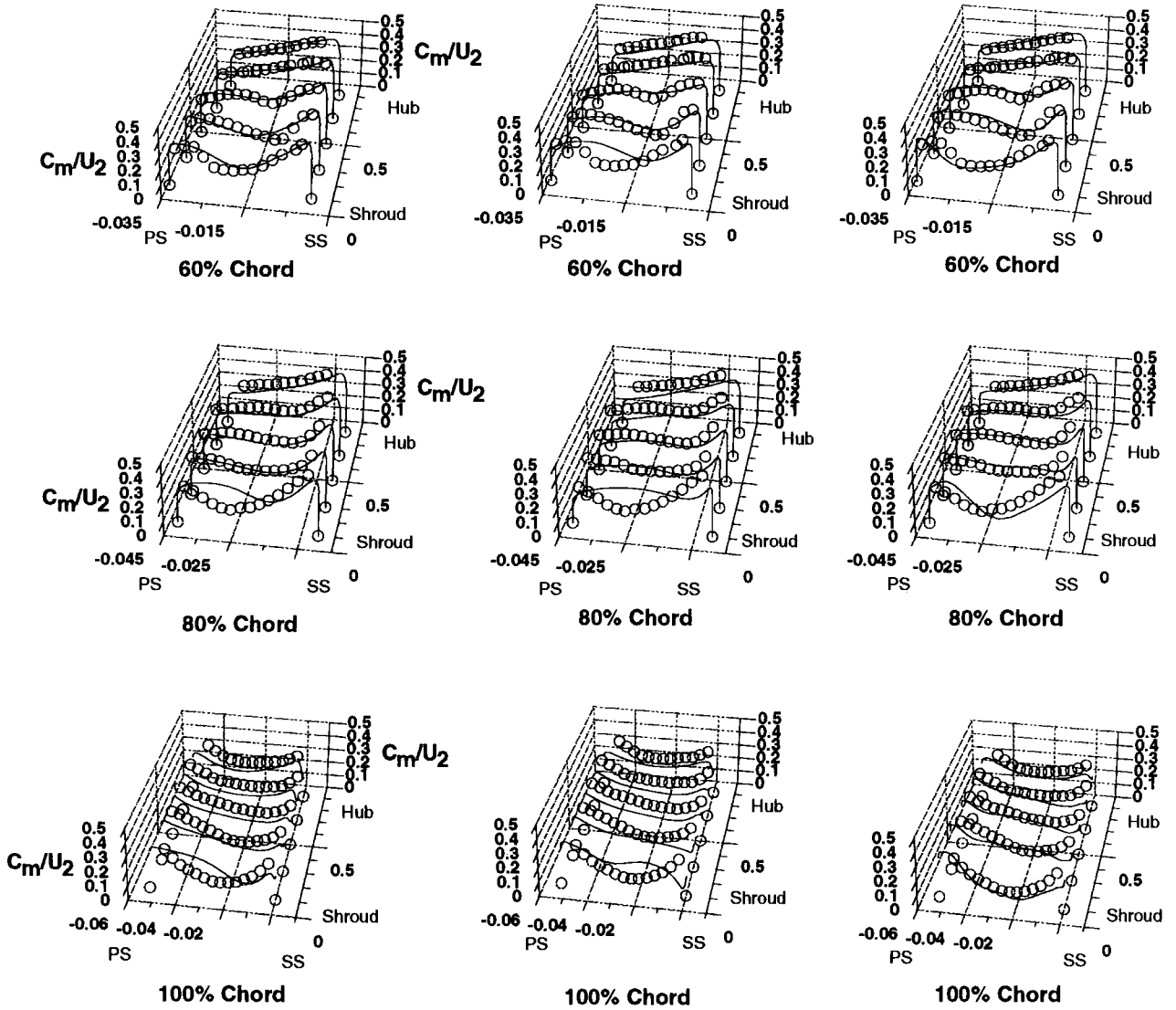
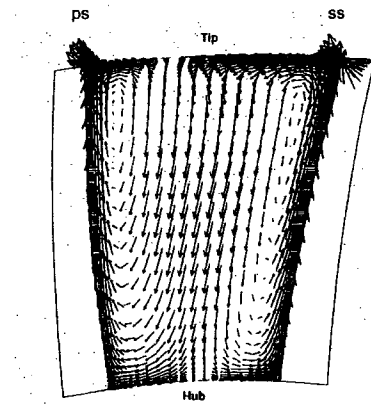


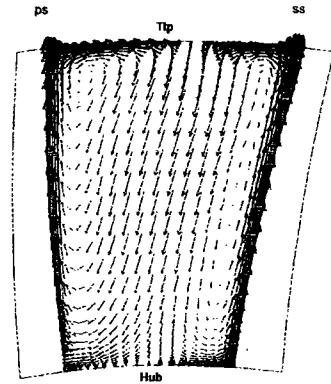
Figure 4-16 Comparison of calculated meridional velocity profiles with different tip gaps (lines: calculations, circles: experimental data with fixed tip gap for reference)

1% tip gap (reference)

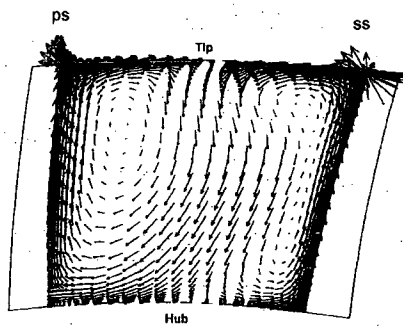
No tip gap



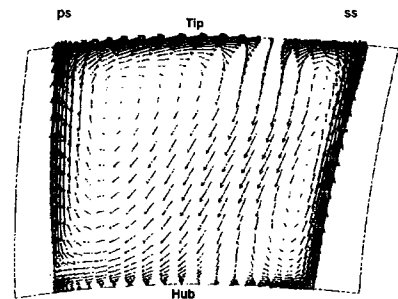
40% section



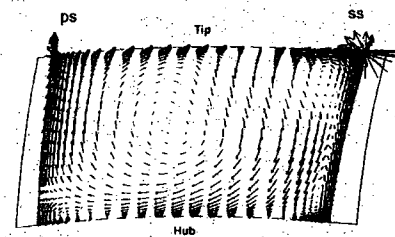
40% section



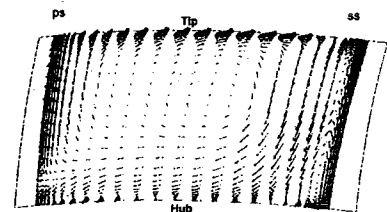
60% section



60% section



80% section



80% section

**Figure 4-17 Comparison of calculated secondary velocity vectors between 1% tip gap case and no tip gap case**

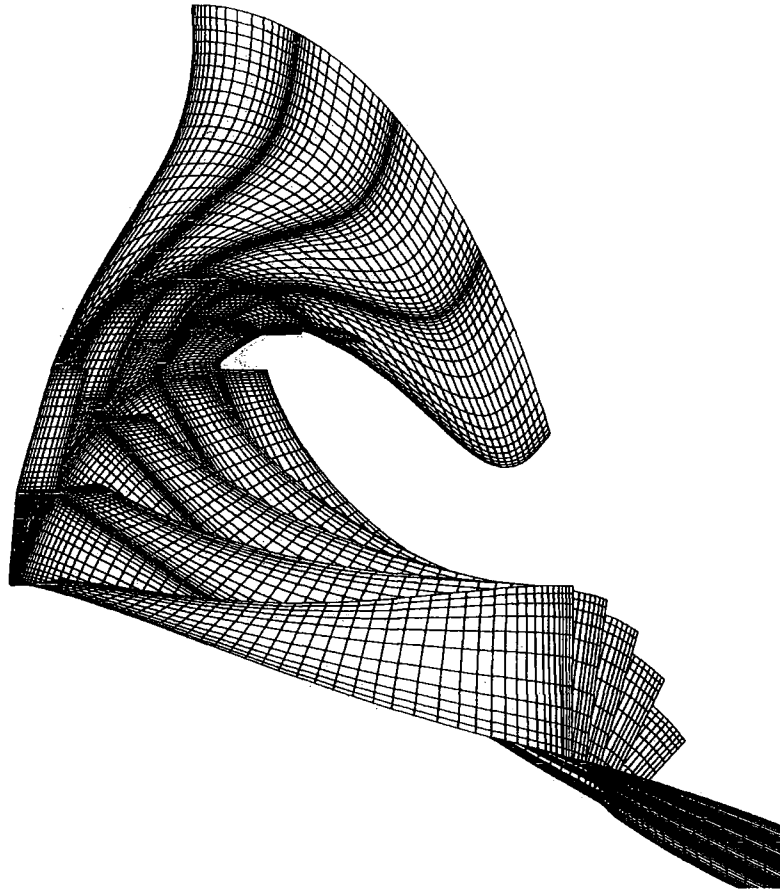


Figure 5-1 Three-dimensional view of computational mesh for the compressor stage

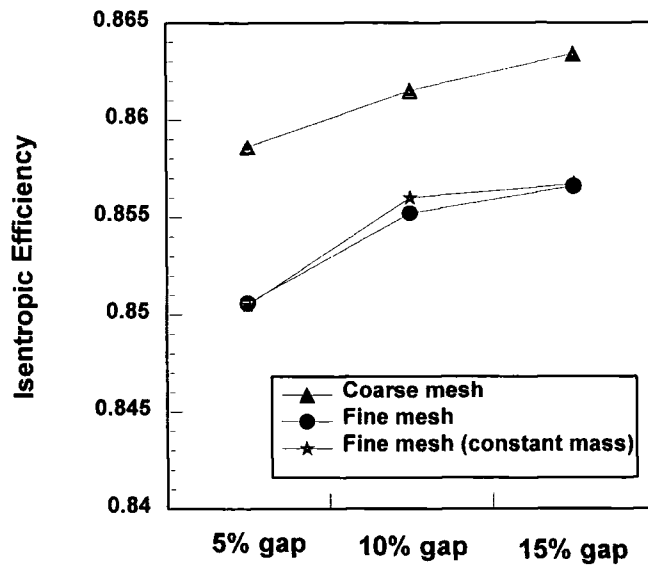


Figure 5-2 Comparison of calculated isentropic efficiency among three radial gap configurations

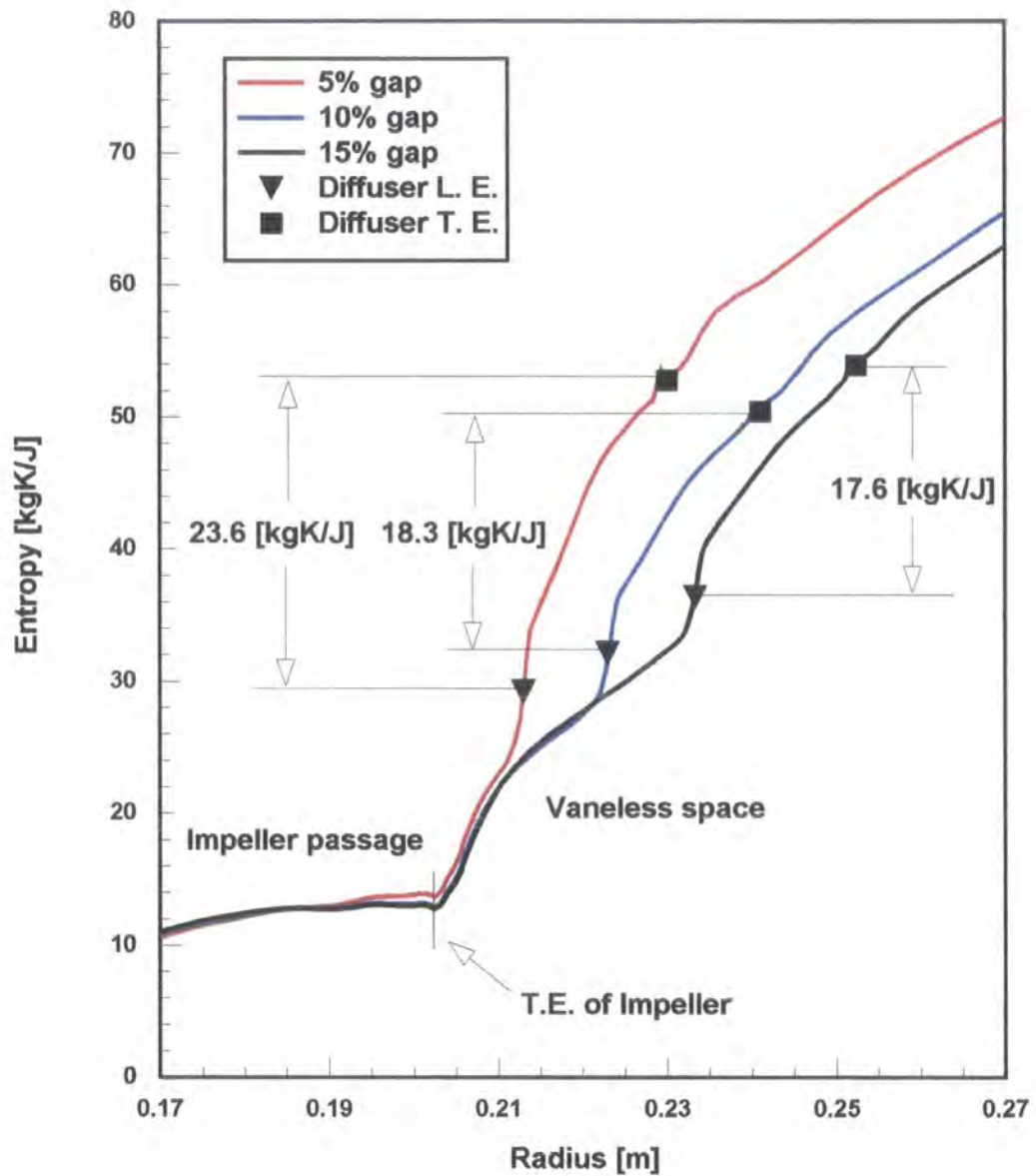


Figure 5-3 Comparison of entropy generations among three radial gap configurations in radial direction (at same mass flow rate)

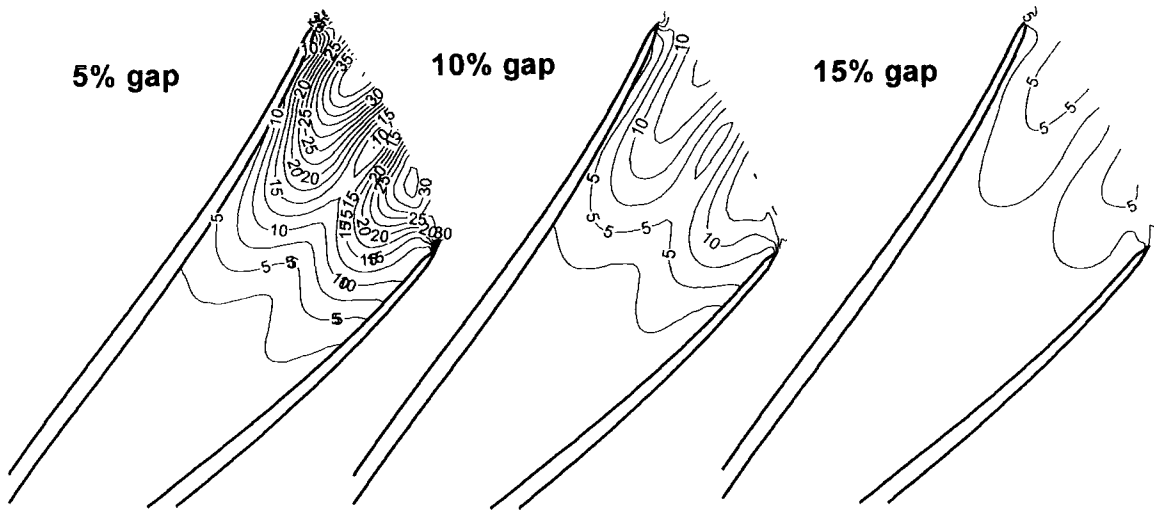


Figure 5-4 Comparison of calculated unsteadiness of relative velocity near the impeller exit at mid span

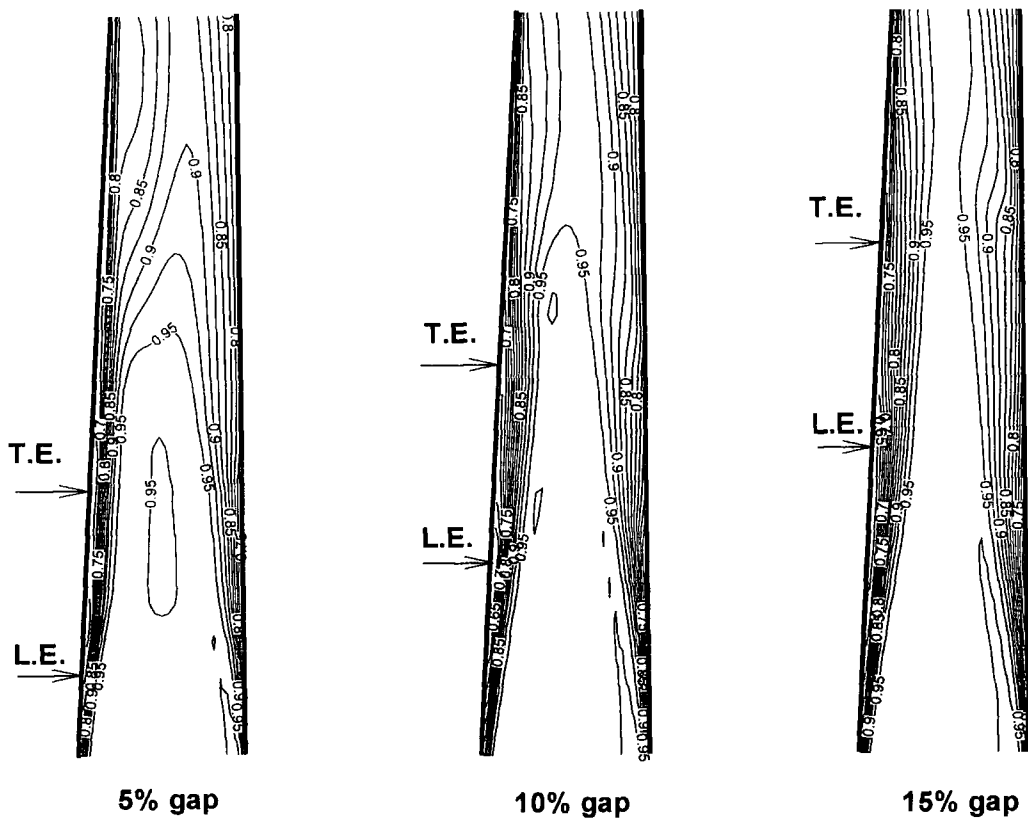


Figure 5-5 Comparison of calculated time-averaged loss contours in the diffusers in a meridional section at mid pitch



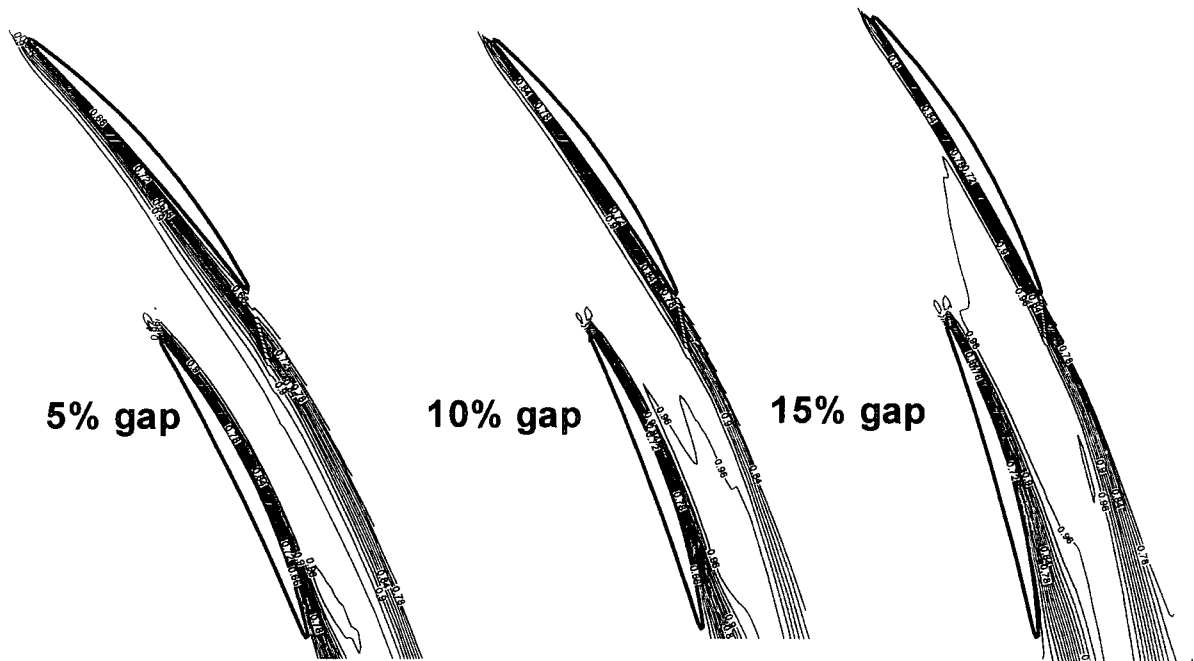


Figure 5-8 Comparison of calculated time-averaged entropy contours in the diffuser passage at mid-span

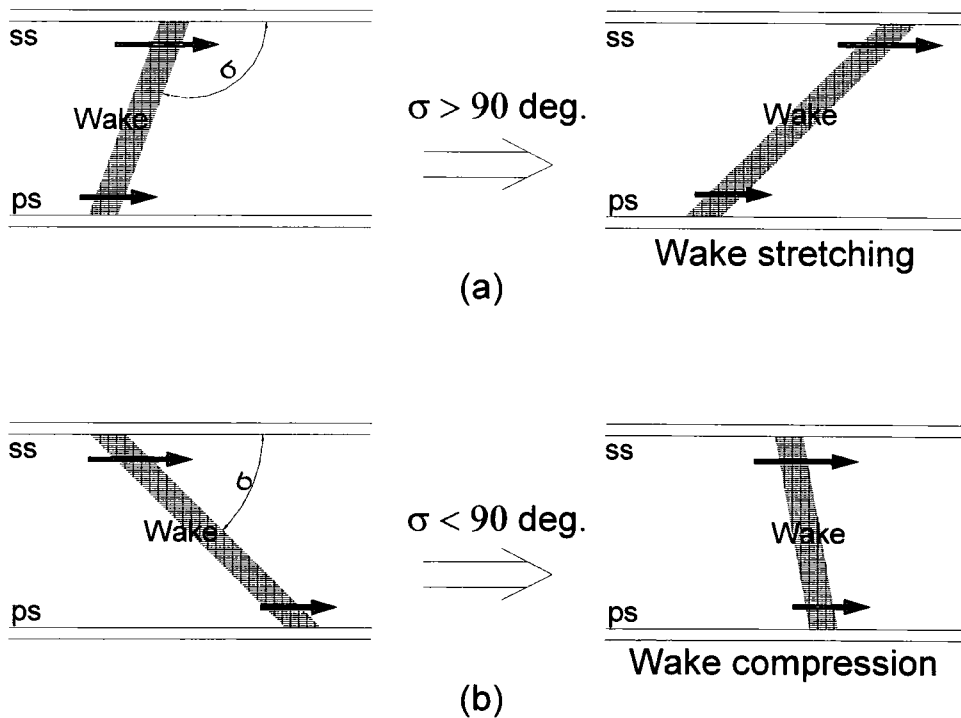
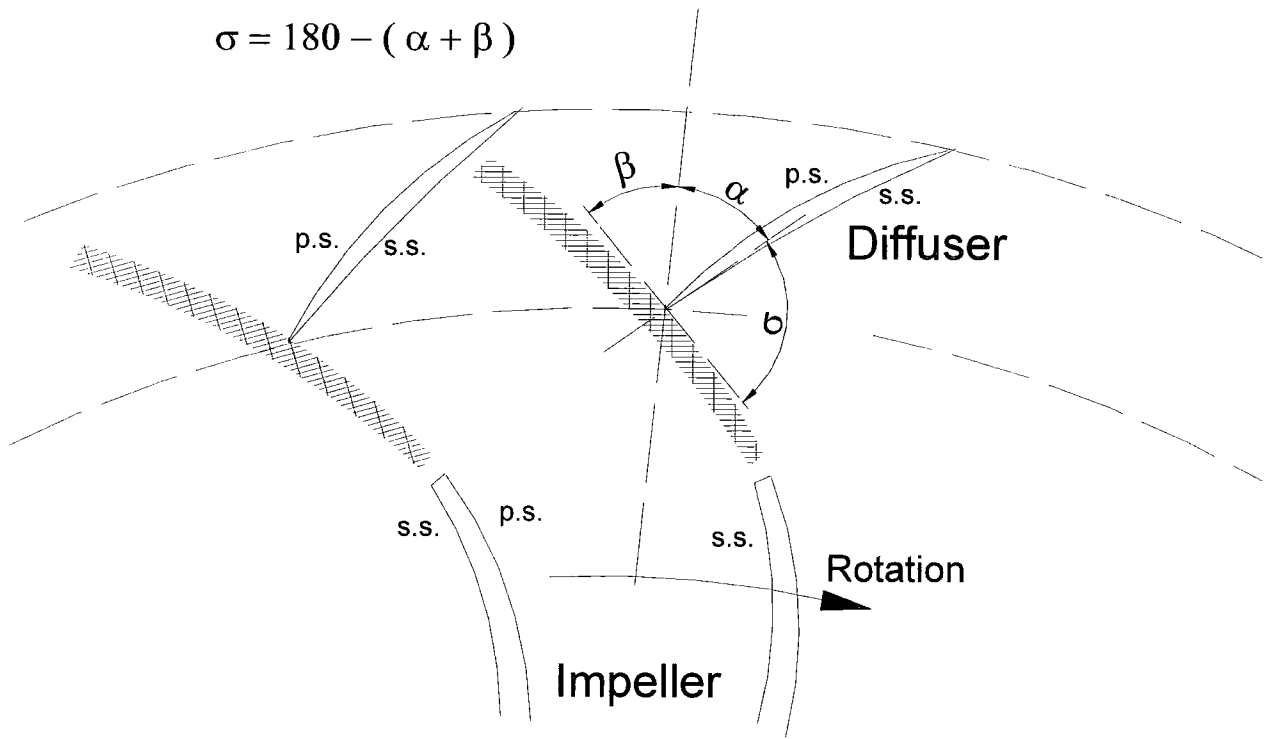
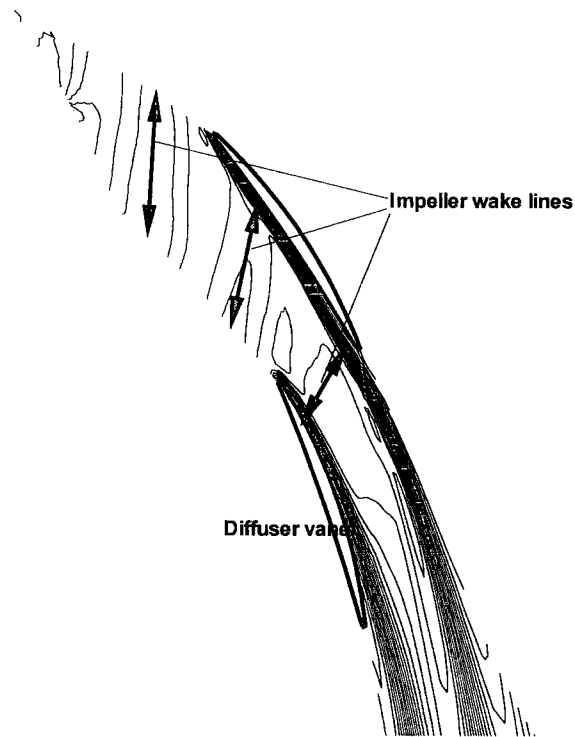


Figure 5-9 Schematic of wake motion through a blade cascade

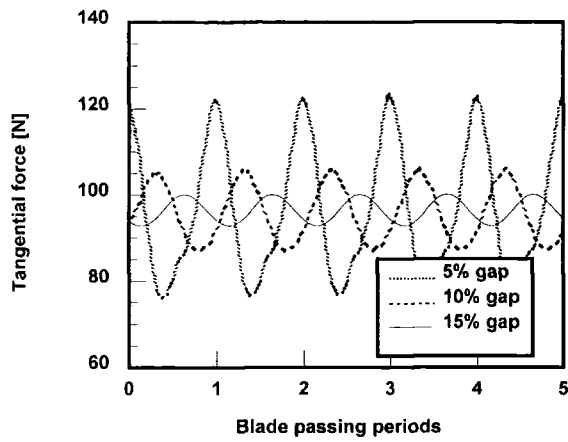


**Figure 5-10 Schematic of wake chopping in a centrifugal compressor stage**

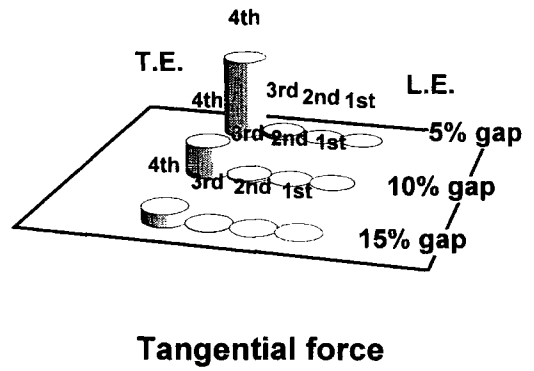


**Figure 5-11 Wake compression in a radial diffuser vane passage  
(calculated loss contours)**



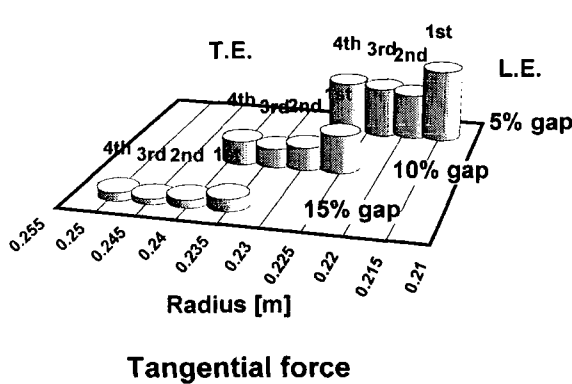


( a )

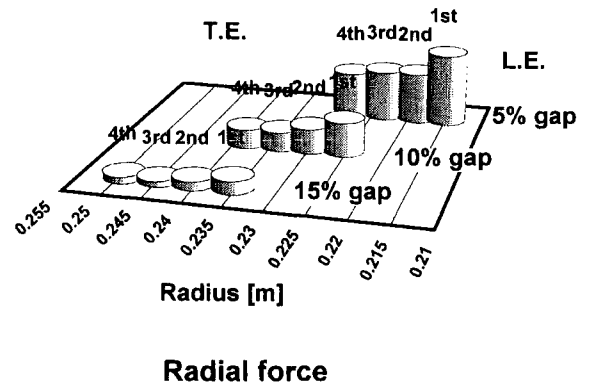


( b )

**Figure 5-12 Comparison of calculated tangential blade forces on the impeller blades among three radial gap configurations**



**Tangential force**



**Radial force**

**Figure 5-13 Comparison of calculated amplitudes of blade force fluctuations on the diffuser vanes among three radial gap configurations**

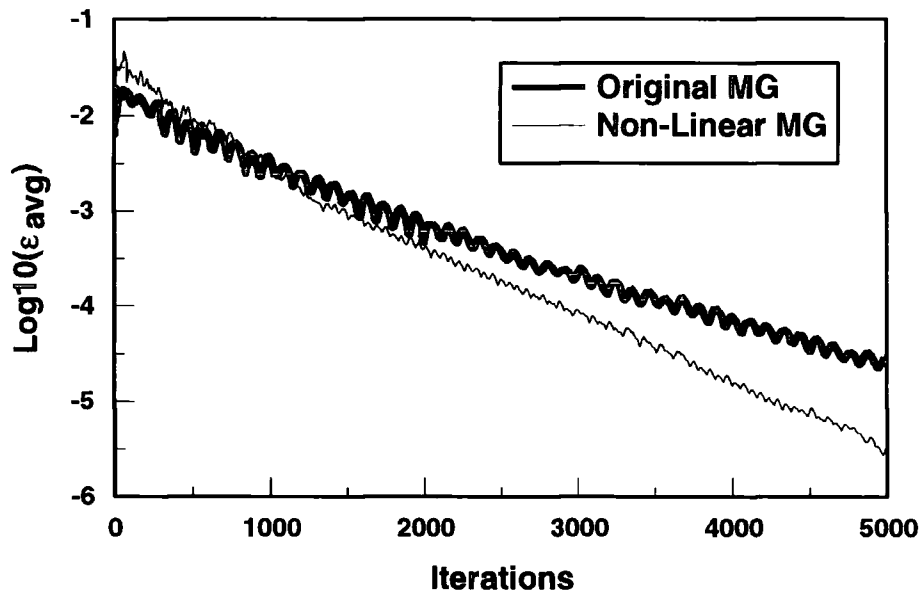
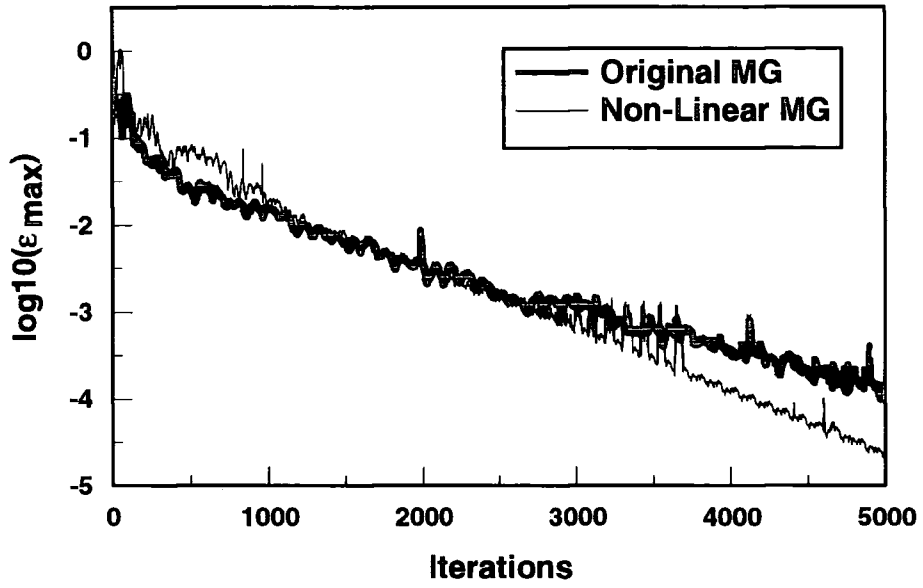


Figure 6-1 Comparison of convergence histories between the different multi-grid methods

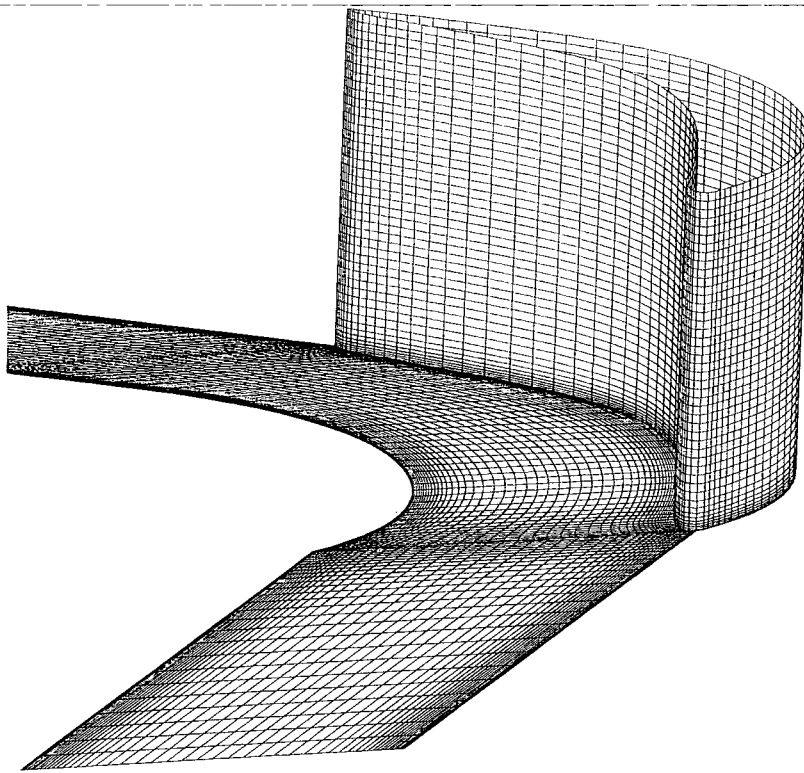


Figure 7-1 Numerical mesh for the Durham turbine cascade

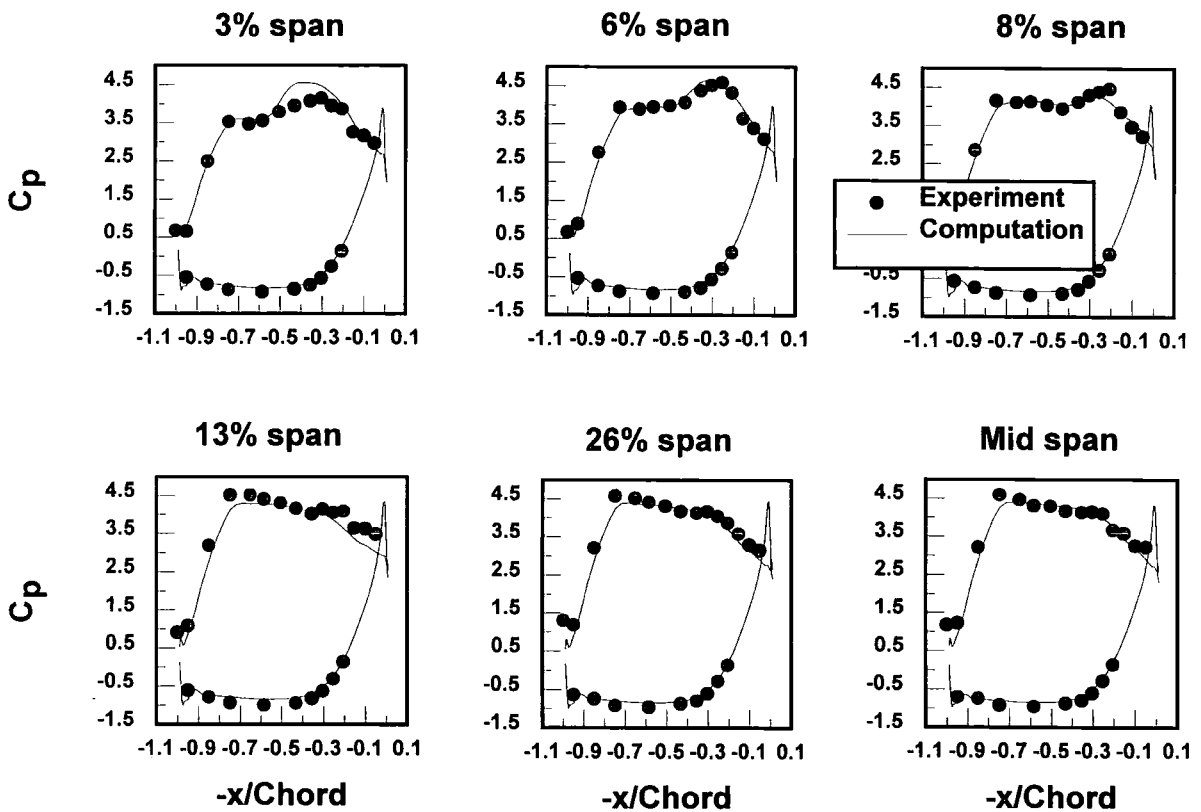
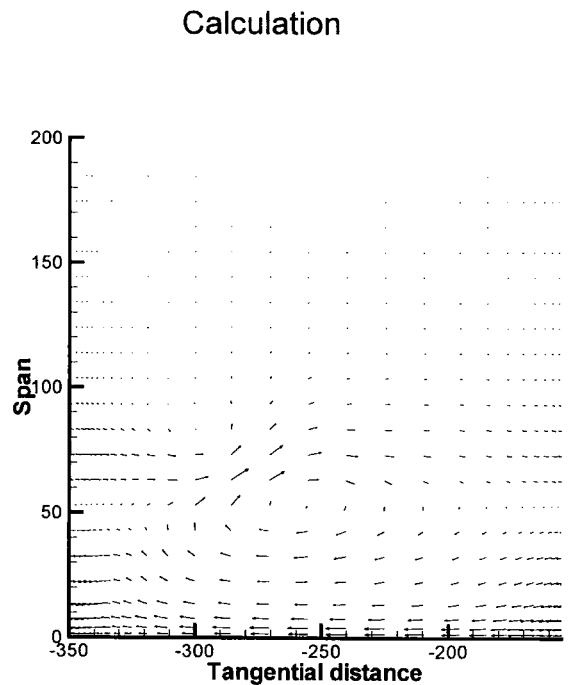
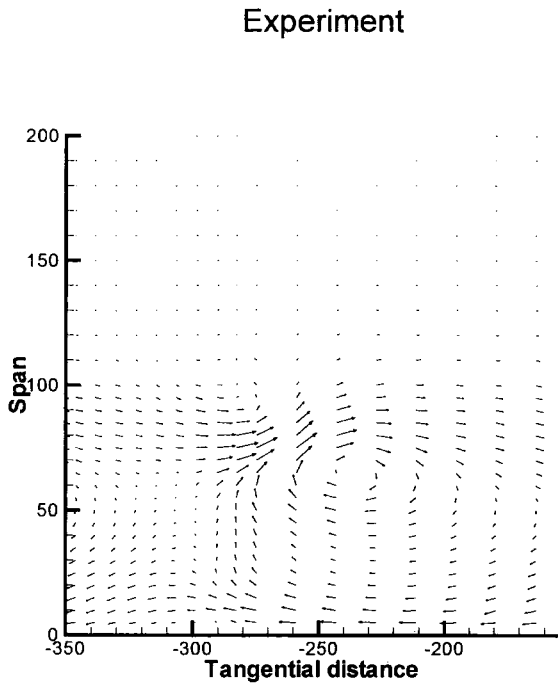
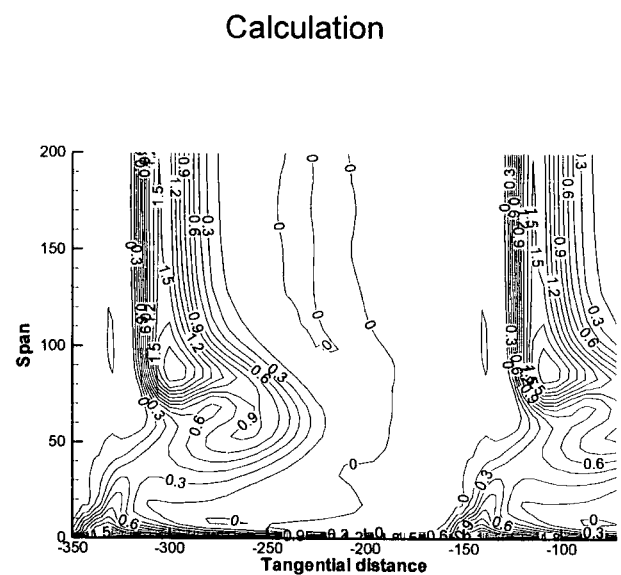
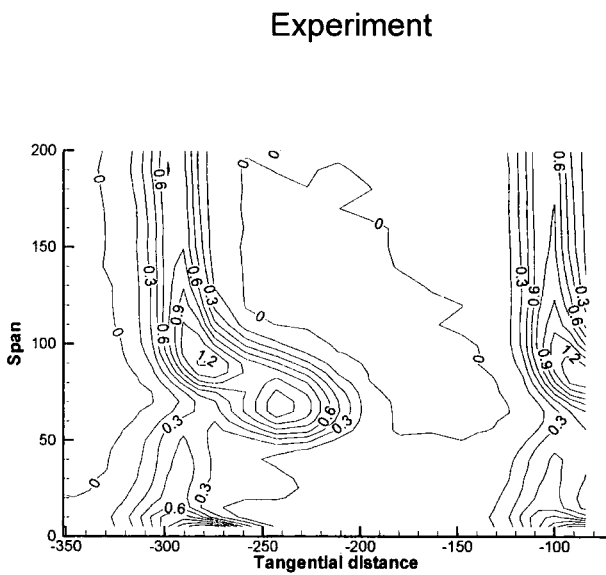


Figure 7-2 Comparison of calculated and measured pressure coefficient distribution



**Figure 7-3 Comparison of calculated and measured secondary flow vectors at 28 percent axial chord downstream section**



**Figure 7-4 Comparison of the total pressure loss coefficient at 28 percent axial chord downstream section**

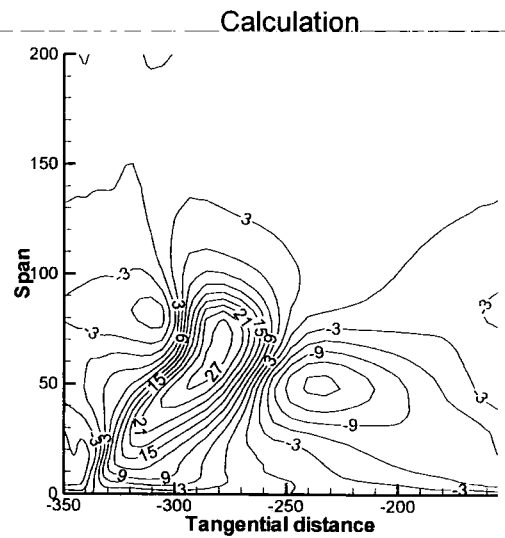
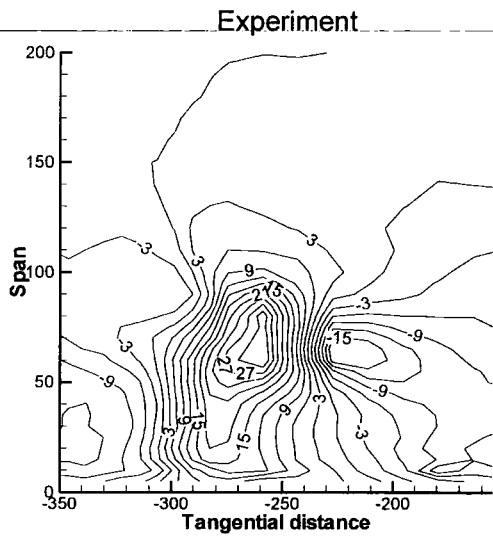


**Figure 7-5 Comparison of pitch flow angle contours at 28 percent axial chord downstream section**

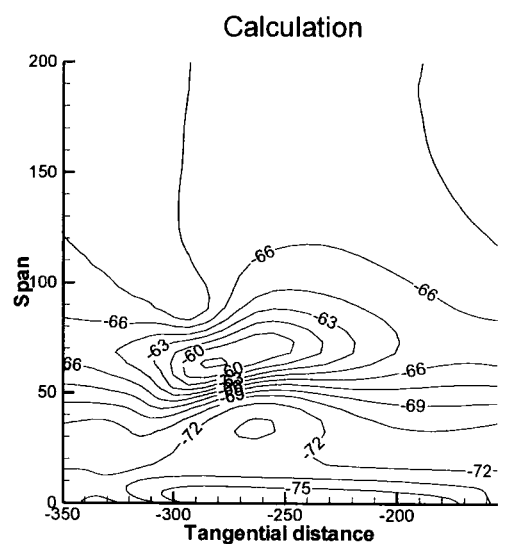
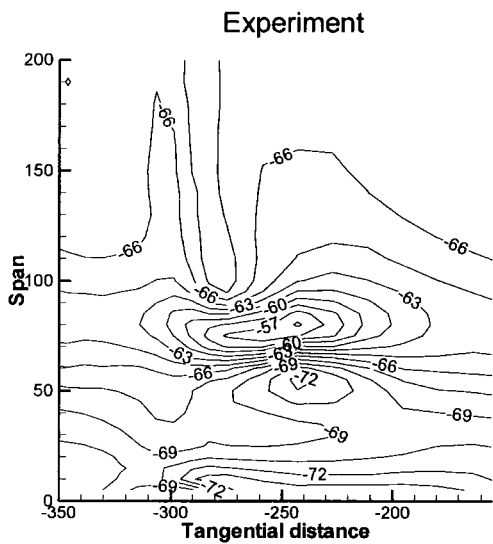


**Figure 7-6 Comparison of yaw flow angle contours at 28 percent axial chord downstream section**

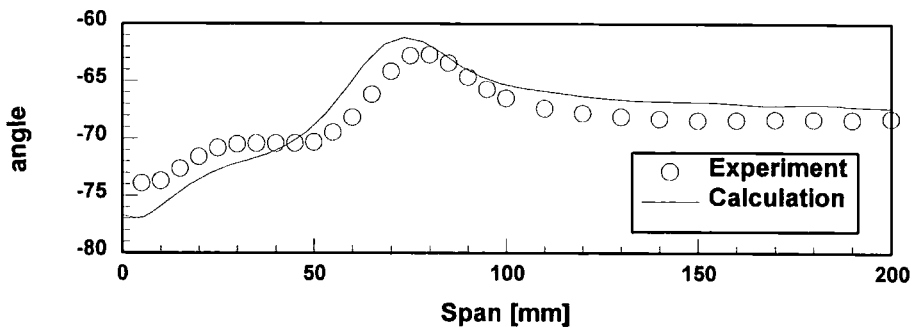


**Figure 7-7 Comparison of pitch-averaged yaw angle distributions at 28 percent axial chord downstream section**

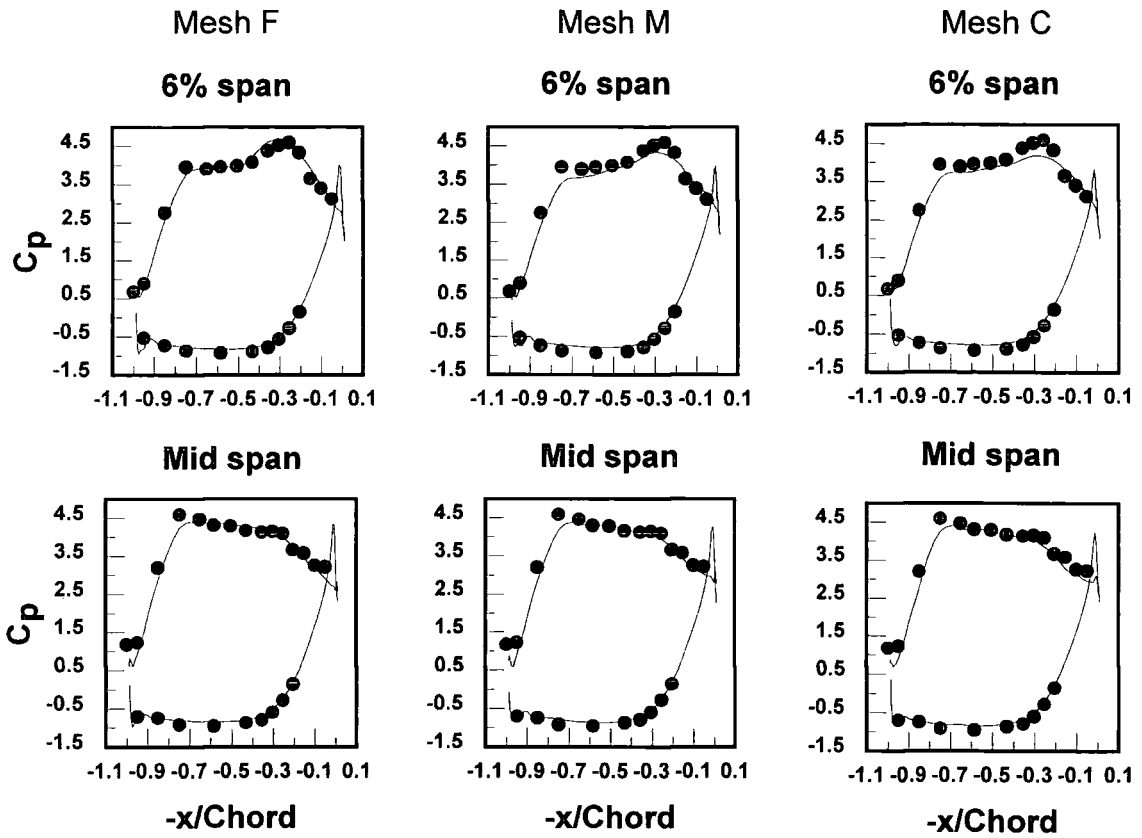


Figure 7-8 Mesh density dependency of static pressure coefficient distributions

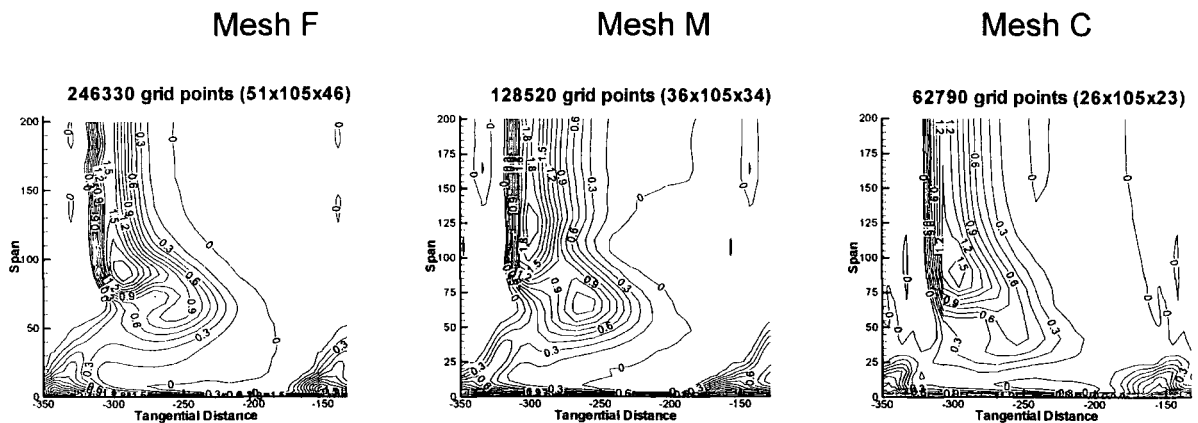


Figure 7-9 Mesh density dependency of total pressure loss contours at 28 percent axial chord downstream section

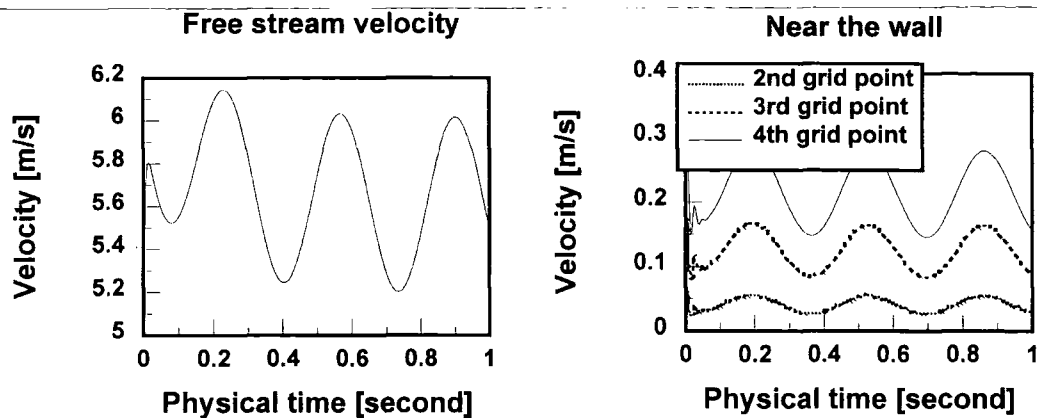


Figure 7-10 Histories of velocity fluctuations

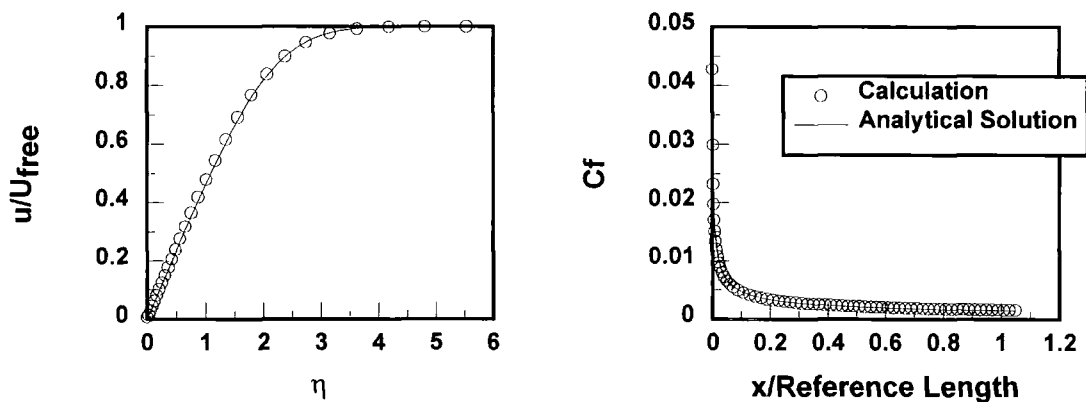


Figure 7-11 Comparison of calculated steady boundary layer solutions with analytical solutions

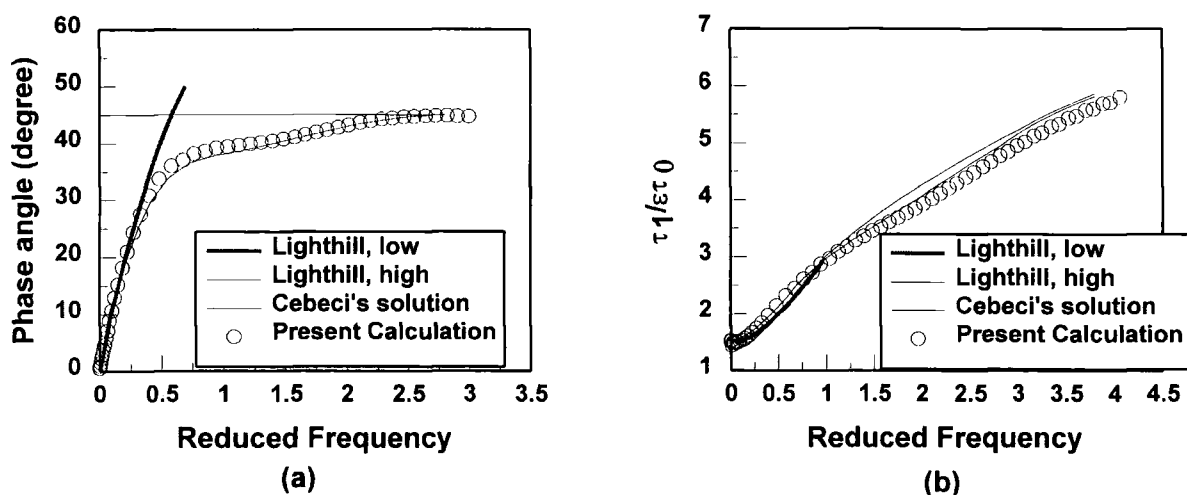


Figure 7-12 Comparison of phase angle between free-stream velocity and wall shear stress (a) and non-dimensionalised unsteady wall shear stress (b)

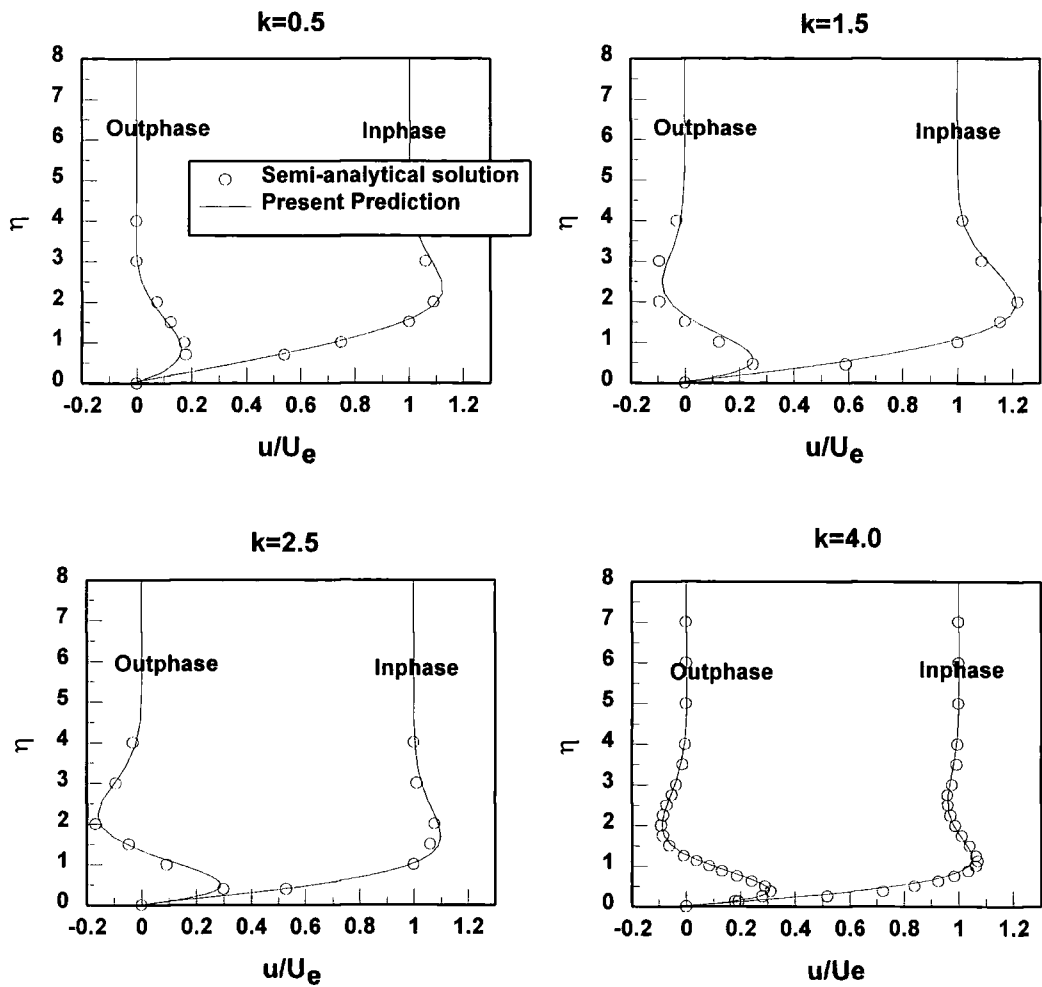


Figure 7-13 Unsteady velocity profiles in the boundary layer at four reduced frequencies

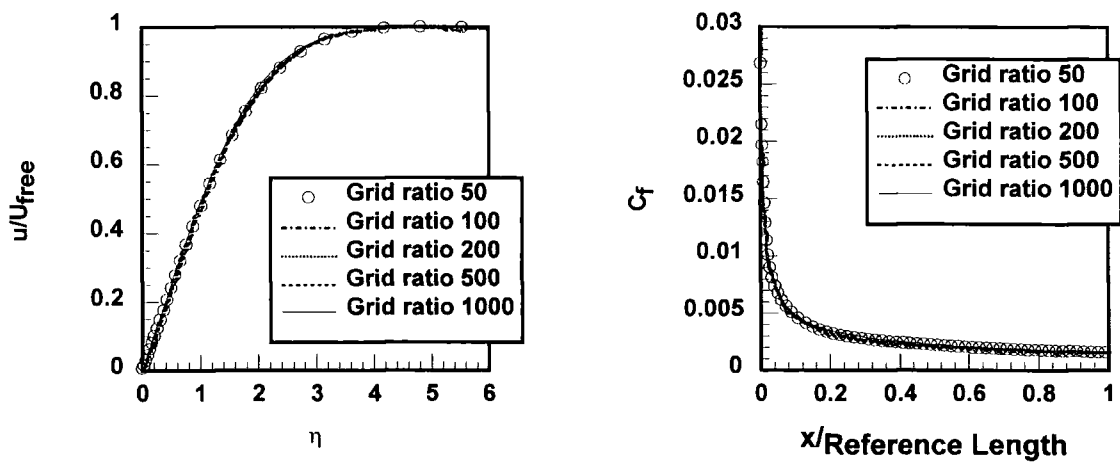


Figure 7-14 Dependency of steady solutions on grid ratio between basic fine grid and coarse grid



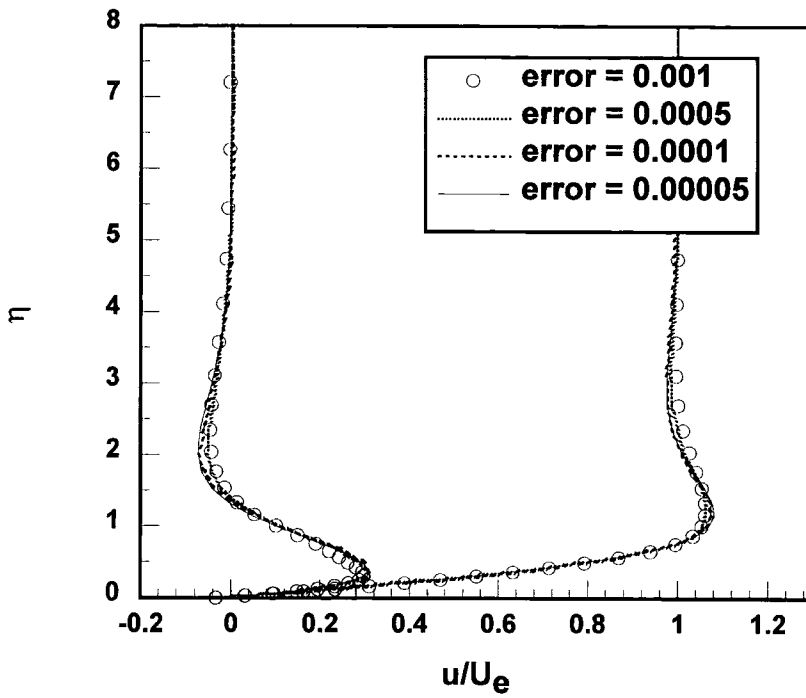
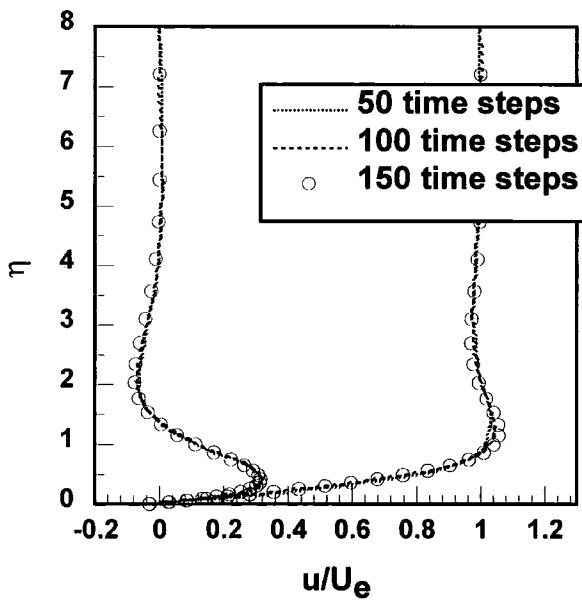
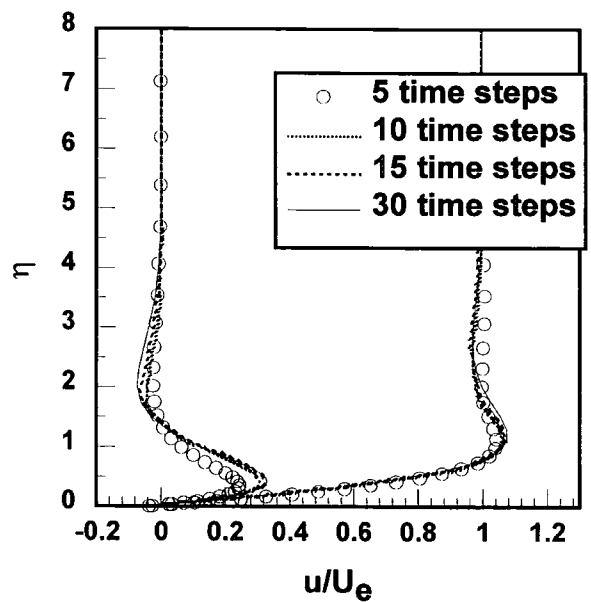


Figure 7-15 Dependency of unsteady solutions on error level in pressure field



(a)



(b)

Figure 7-16 Dependency of unsteady solutions on temporal resolution in a period

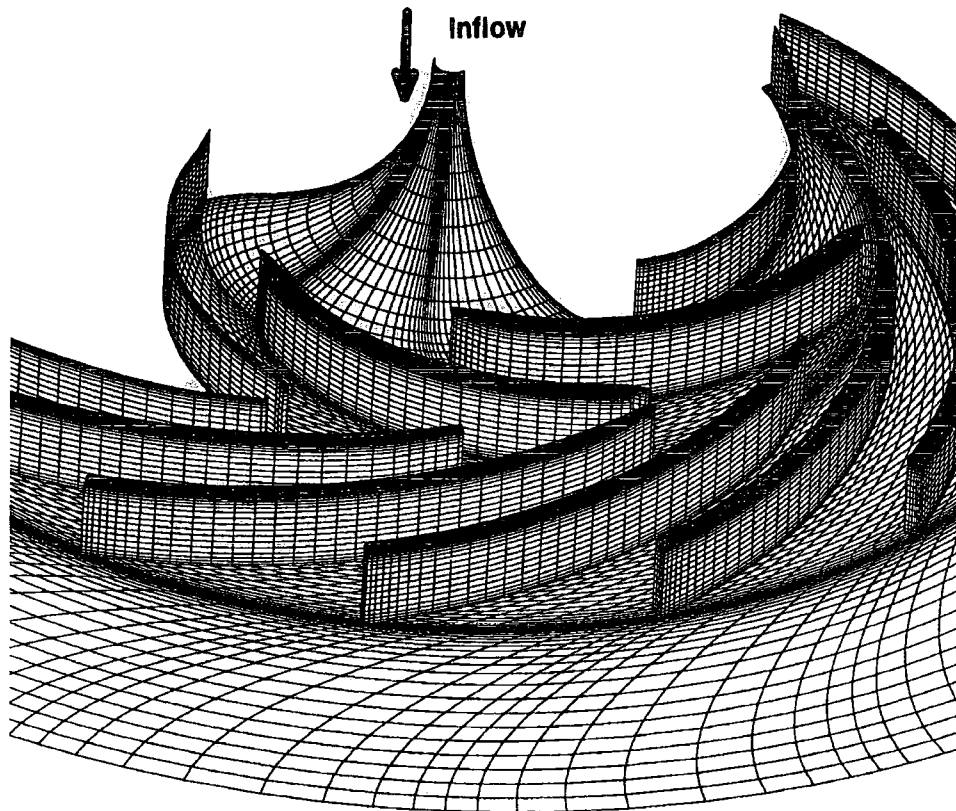


Figure 7-17 Three-dimensional view of computational mesh

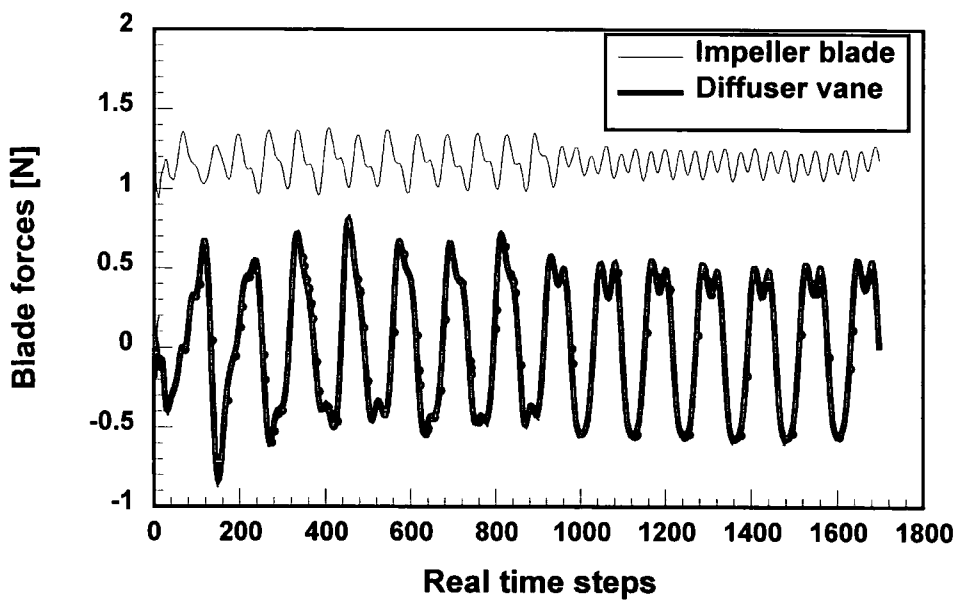


Figure 7-18 Histories of blade forces in the tangential direction on the impeller blade and the diffuser vane

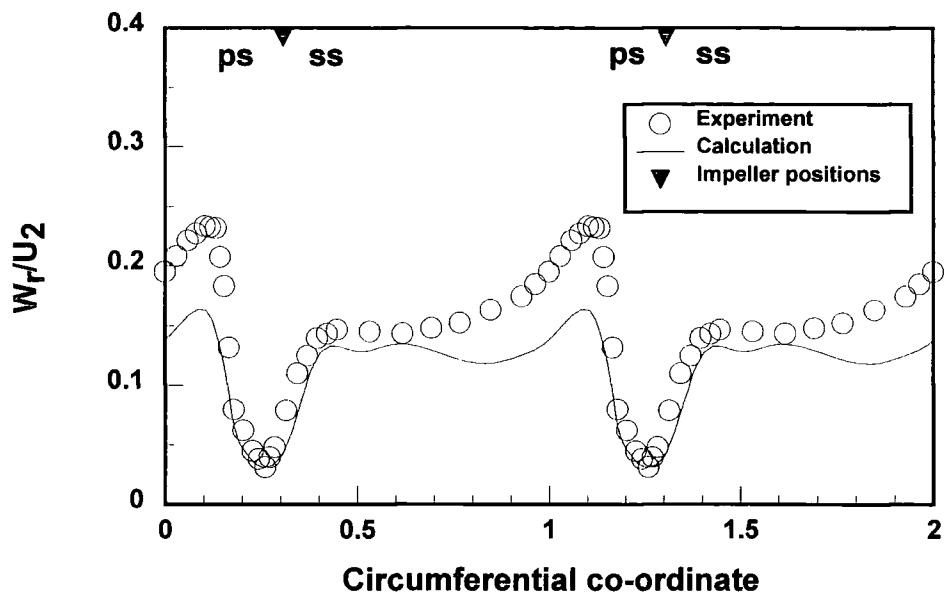


Figure 7-19 Time-averaged radial discharged velocity distribution along the pitch measured at the impeller exit, mid-span

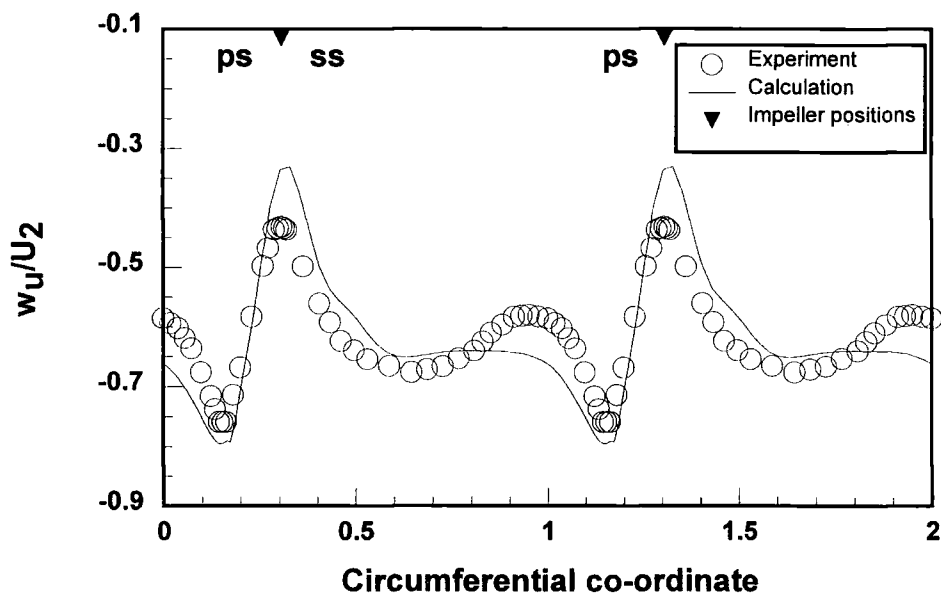
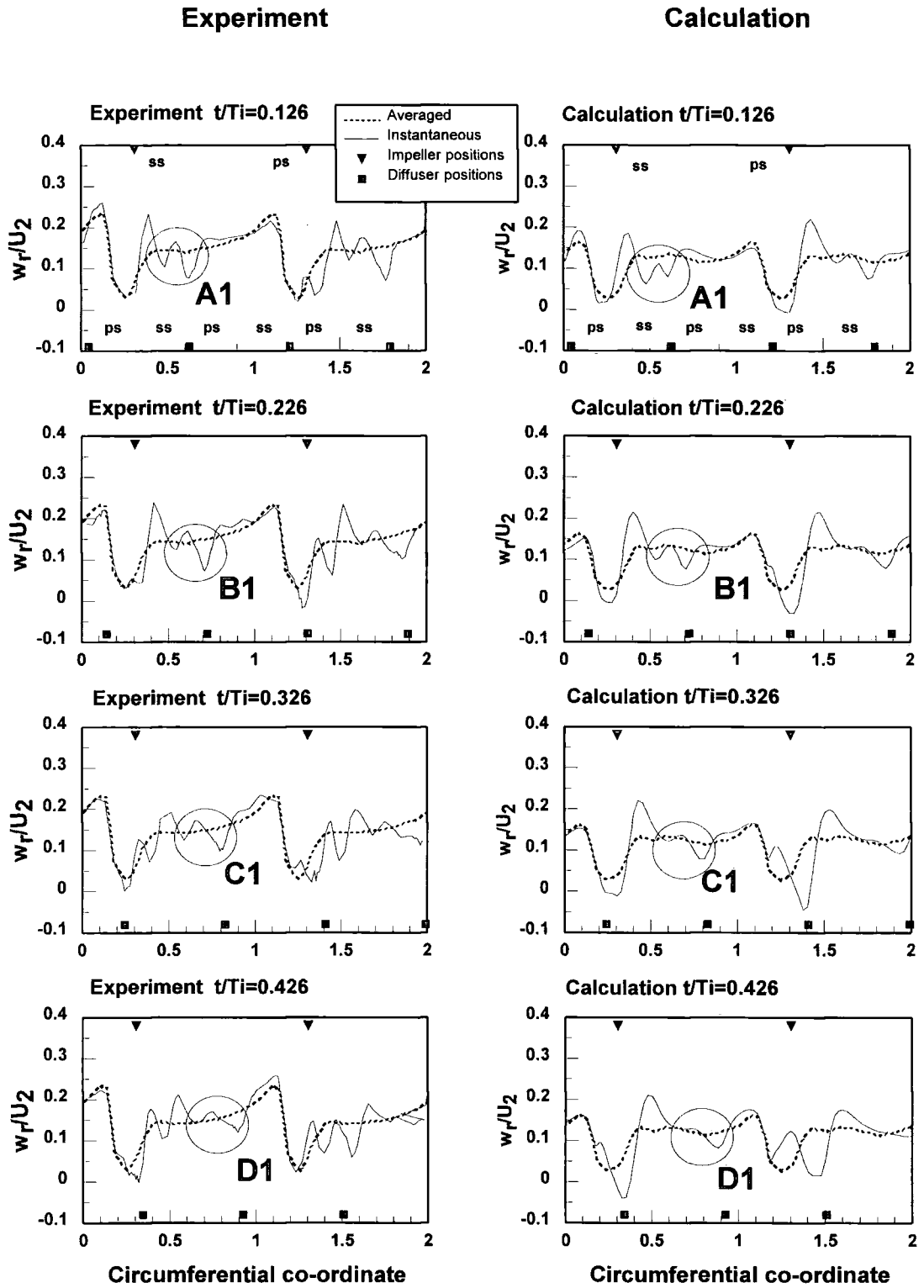


Figure 7-20 Time-averaged relative circumferential velocity distribution along the pitch measured at the impeller exit, mid-span



**Figure 7-21 Radial velocity profiles at four instantaneous positions measured at the impeller exit, mid-span**

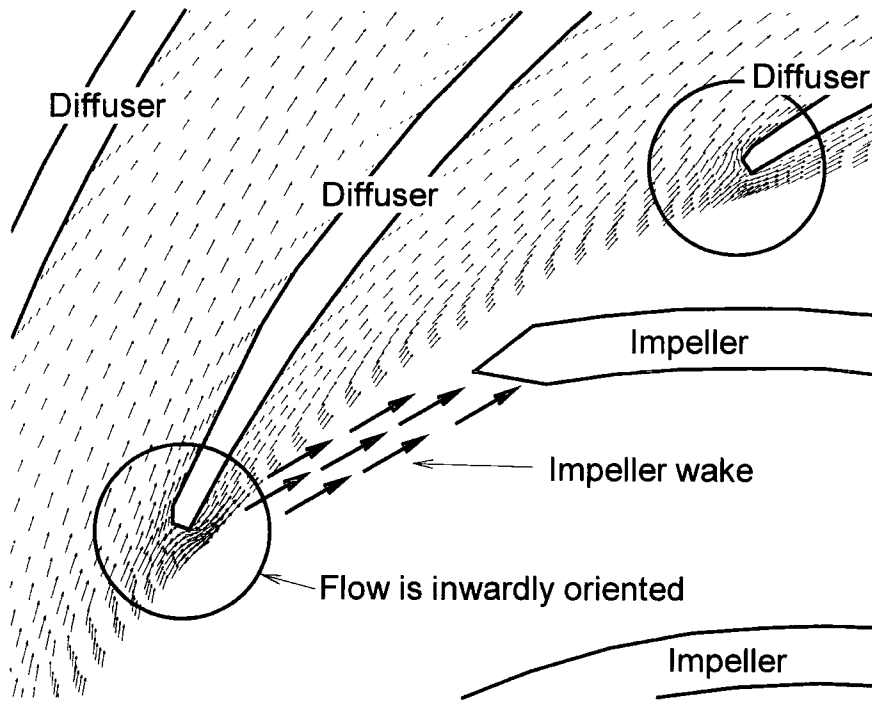


Figure 7-22 Instantaneous flow velocity vector map at mid-span

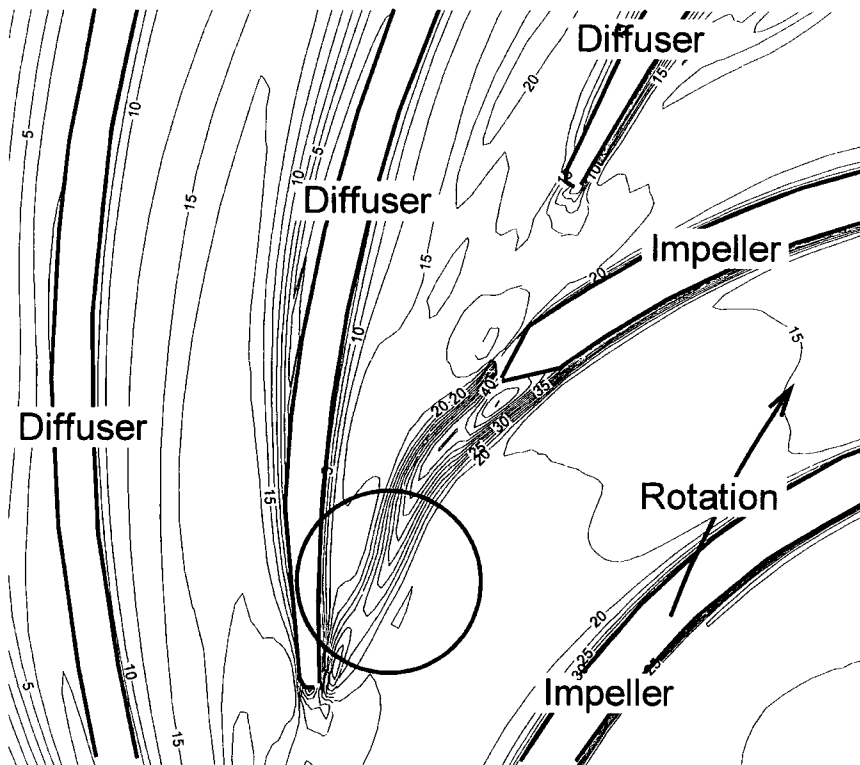
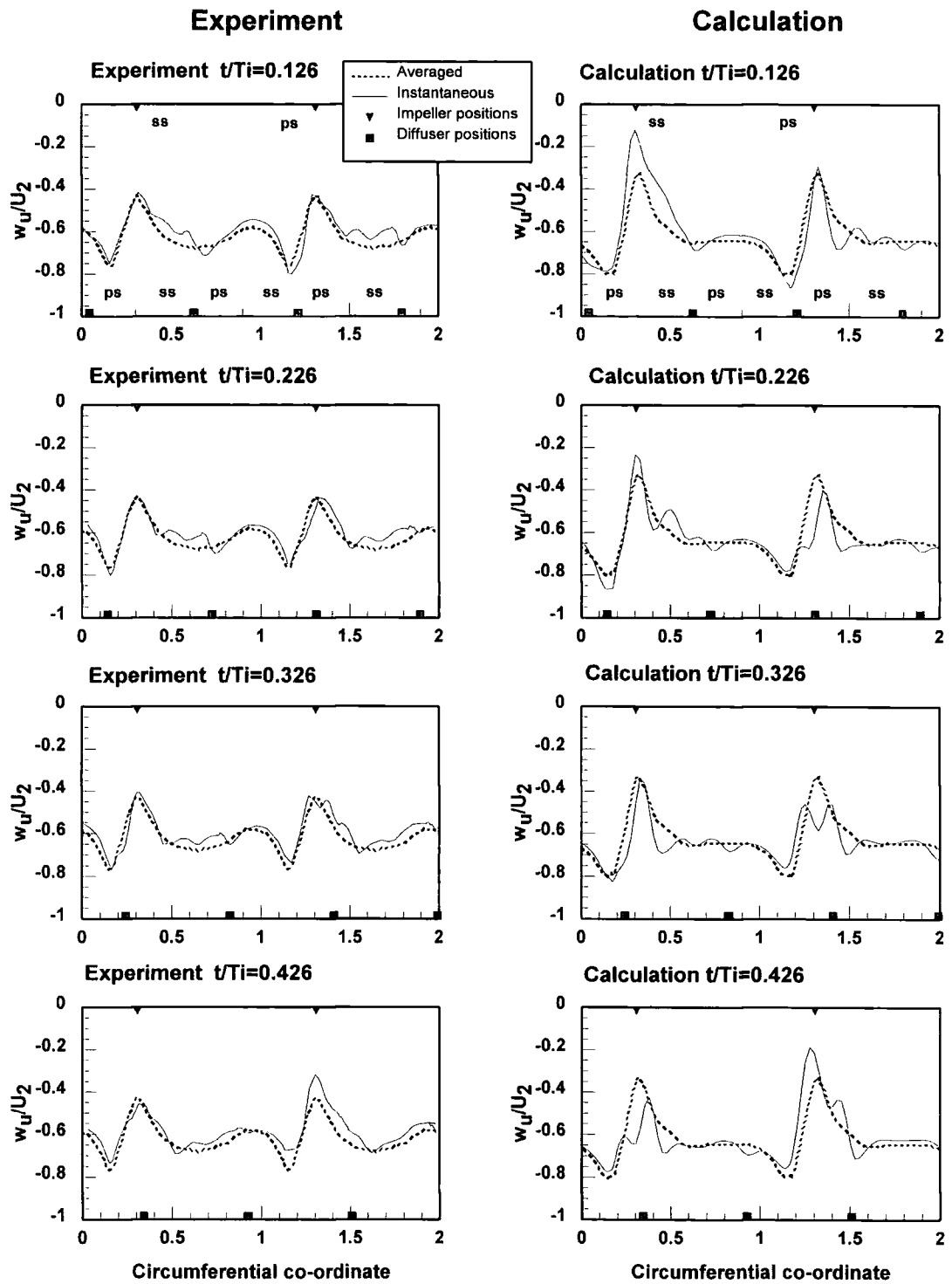


Figure 7-23 Instantaneous absolute velocity contours at mid-span



**Figure 7-24 Relative tangential velocity profiles at four instantaneous positions measured at the impeller exit, mid-span**

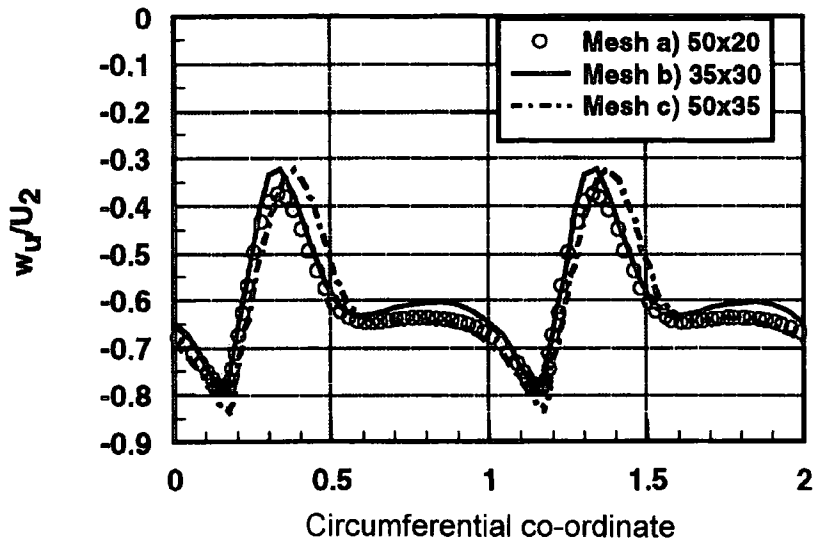
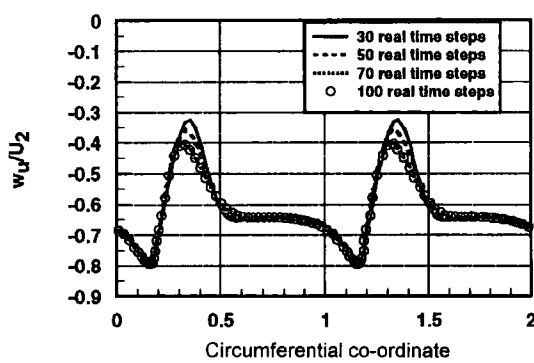
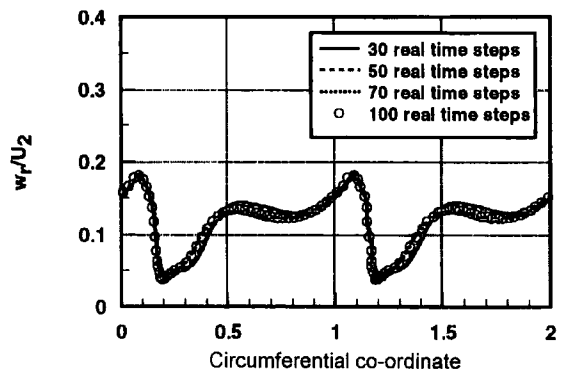


Figure 7-25 Dependency of solutions on mesh density – Comparison of time-averaged relative circumferential velocity profiles at the impeller exit, mid span



(a)



(b)

Figure 7-26 Dependency of solutions on time resolution – Comparison of time-averaged relative circumferential velocity profiles (a) and time-averaged radial velocity profiles (b) at the impeller exit, mid span

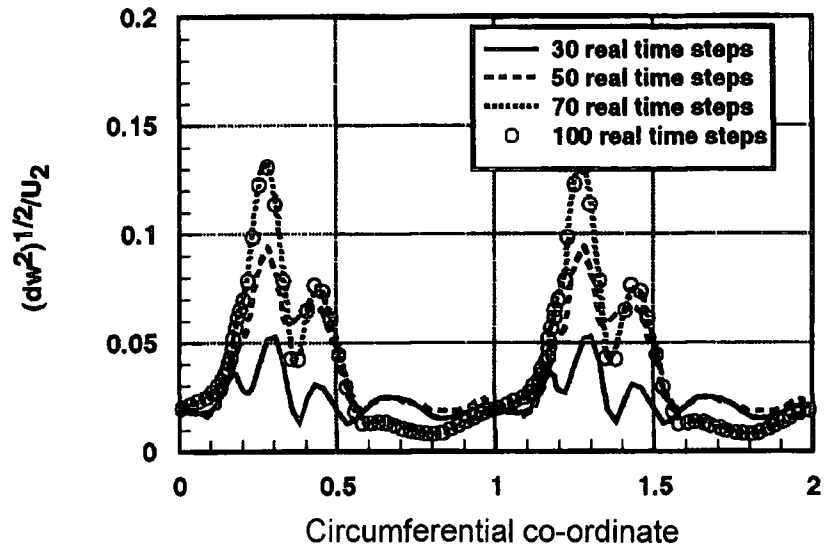


Figure 7-27 Dependency of the solutions on time resolution – Comparison of the stator-generated unsteadiness at the impeller exit, mid span

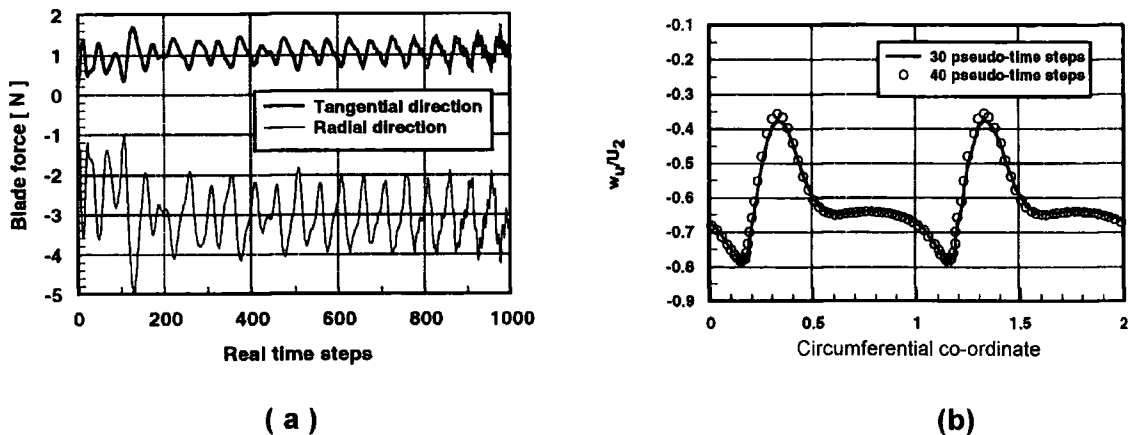


Figure 7-28 Dependency of solutions on the numbers of pseudo-time iterations – Blade force histories (a) and comparison of time-averaged relative tangential velocity profiles (b) at the impeller exit, mid span



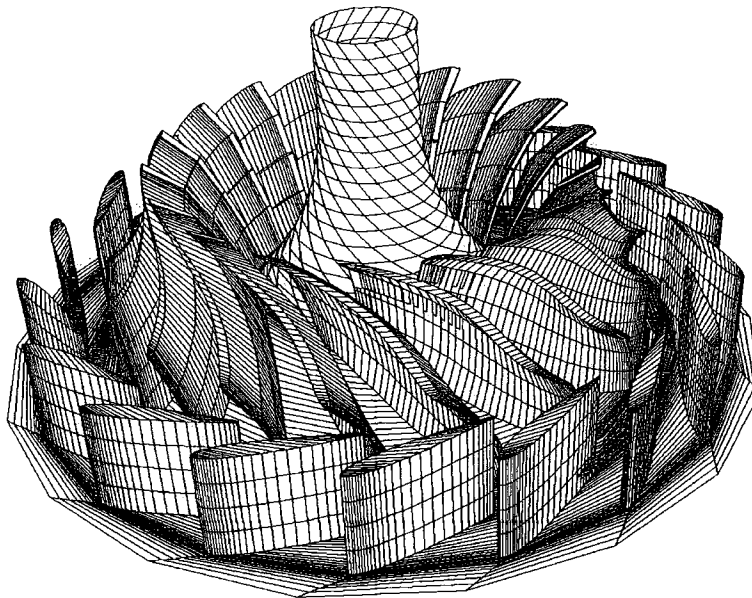


Figure 8-1 Three-dimensional view of the Francis turbine stage

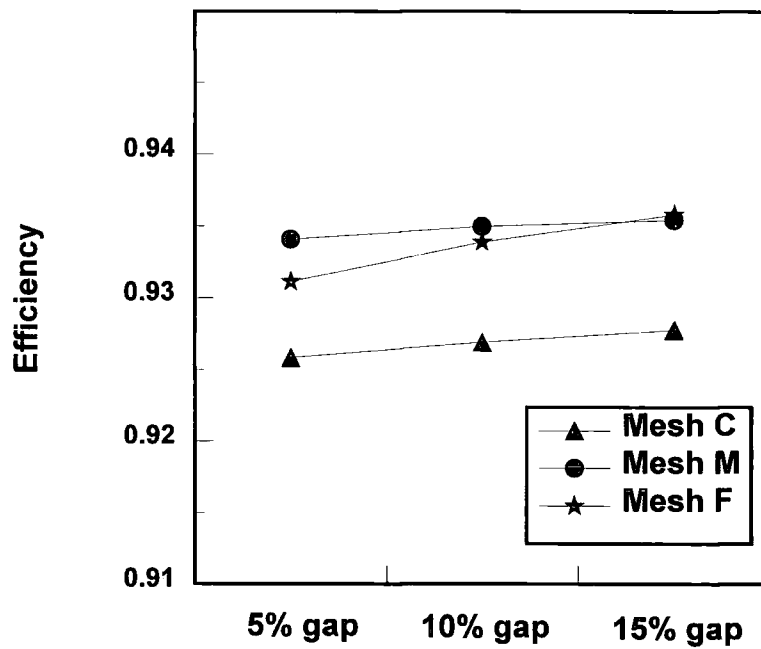


Figure 8-2 Comparison of efficiency among Francis turbine stages with three different settings of radial gap

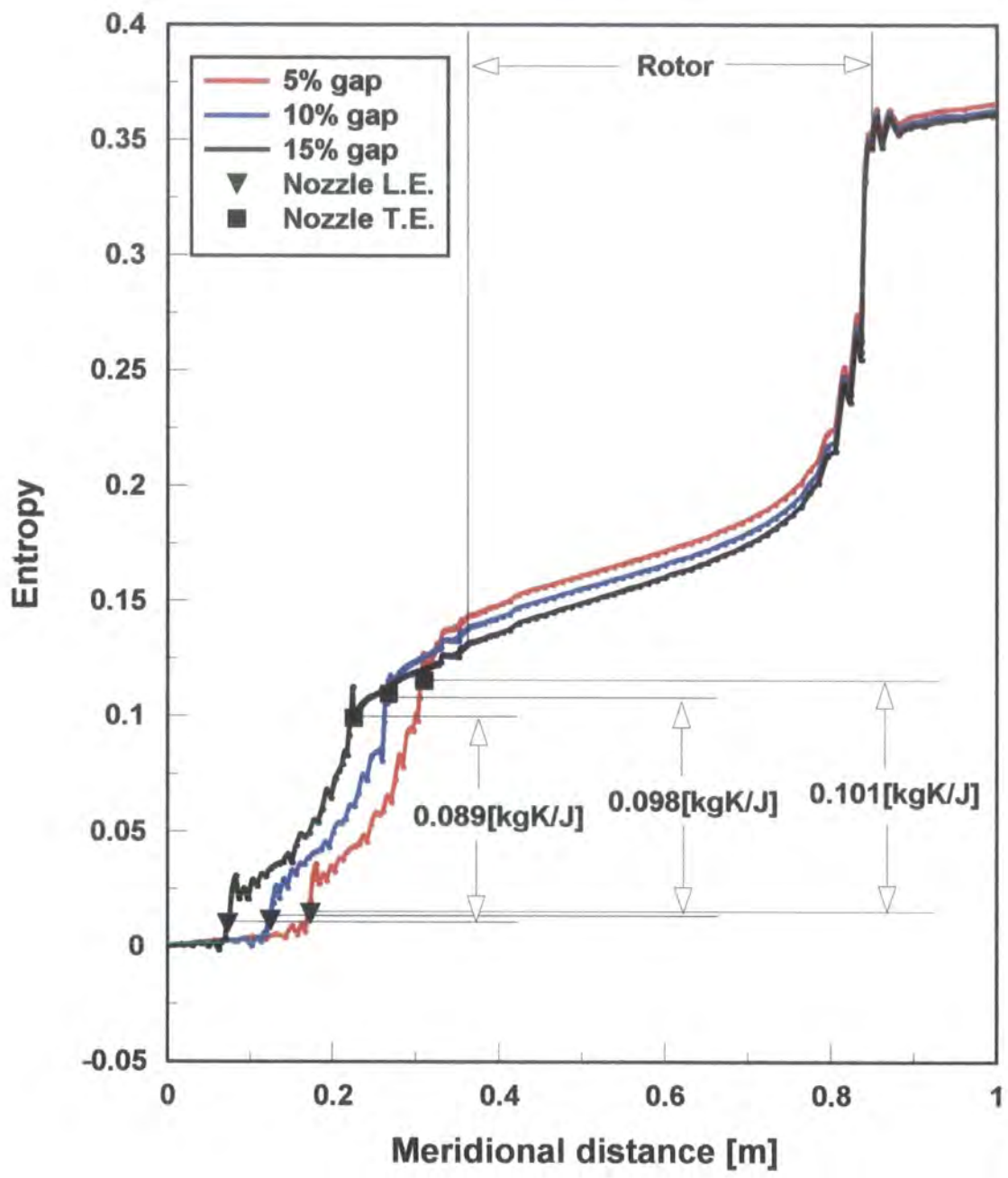


Figure 8-3 Comparison of entropy developments along flow paths among different radial gap configurations

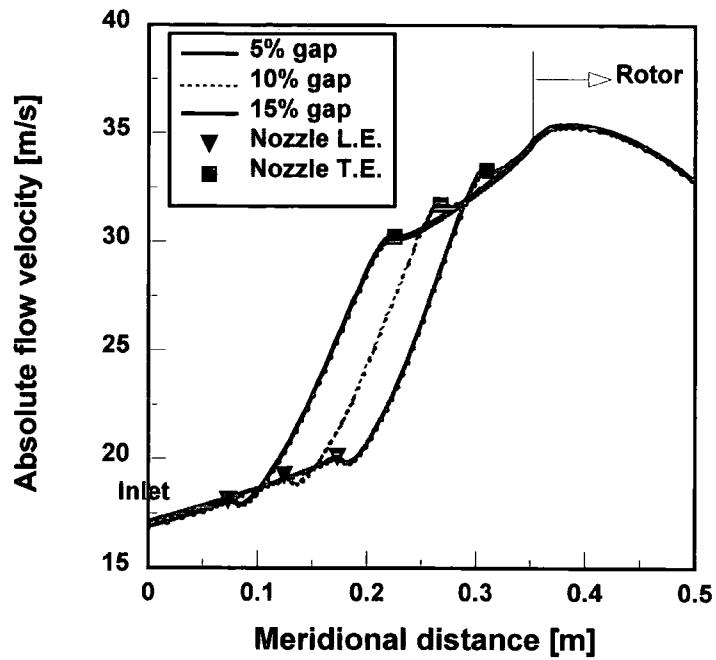


Figure 8-4 Comparison of velocity development along flow passage among three radial gap configurations

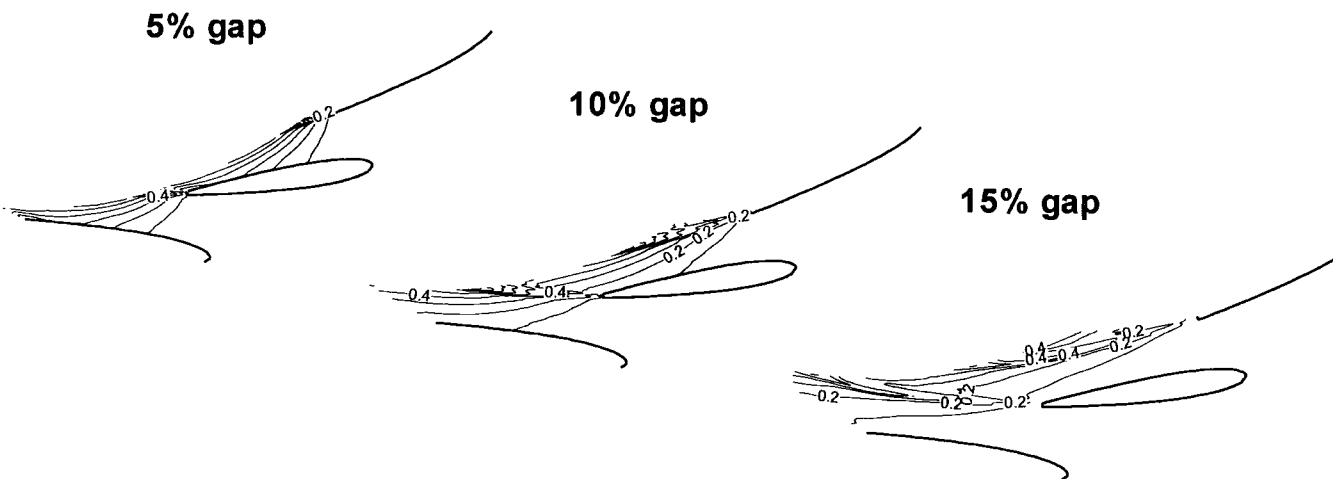


Figure 8-5 Comparison of velocity unsteadiness in the nozzle vane passage among three radial gap configurations

## Flow in the convergent duct

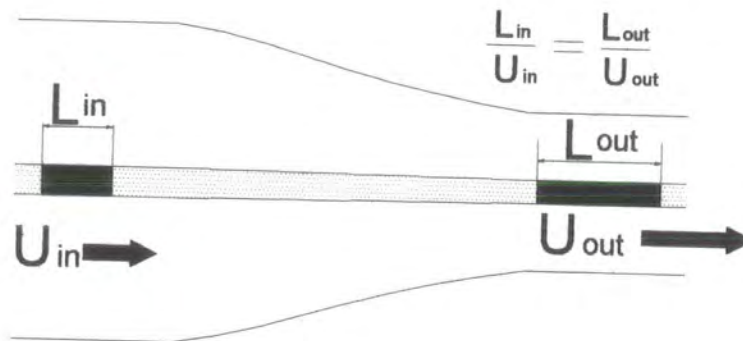


Figure 8-6 Schematic of wake flow stretching

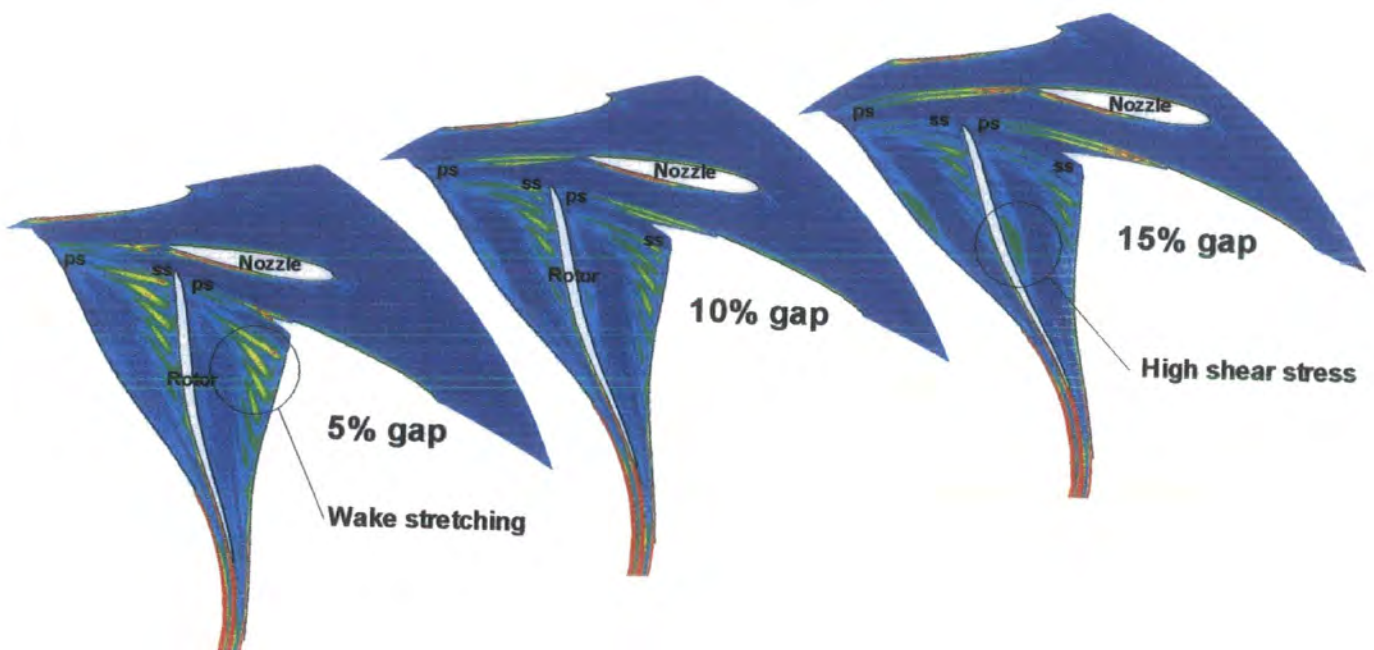


Figure 8-7 Comparison of vorticity contours among three radial gap configurations at mid-span

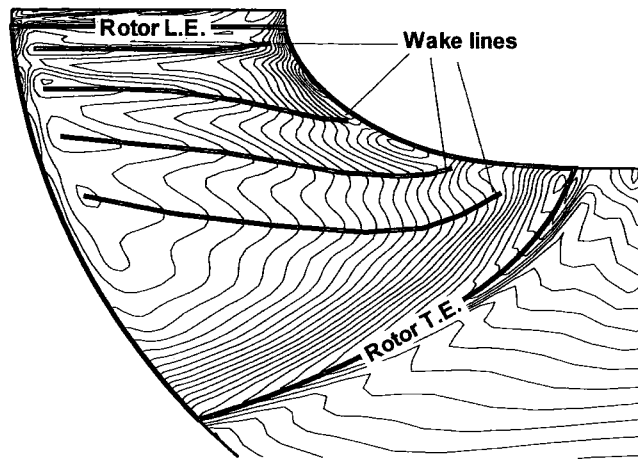


Figure 8-8 Relative velocity contours in a meridional section near the suction surface of rotor for 5% gap configuration

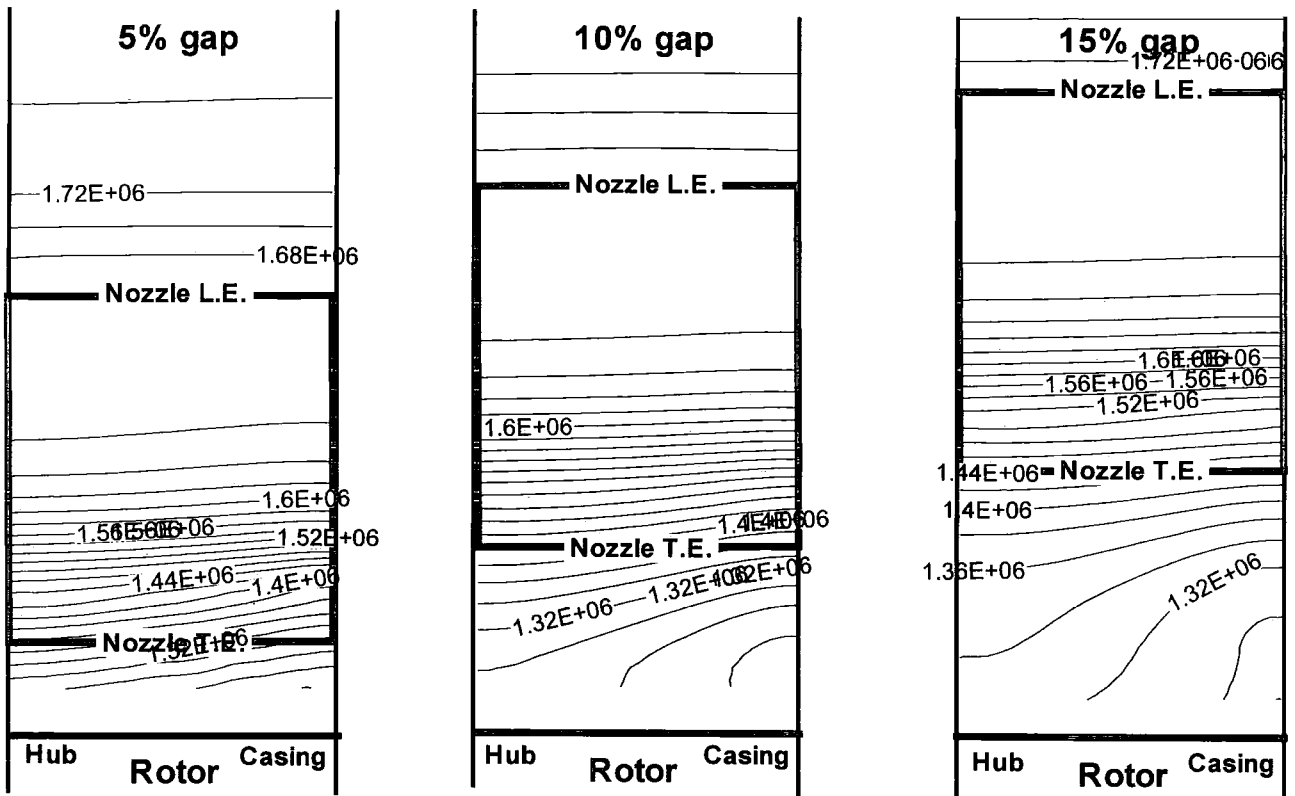


Figure 8-9 Comparison of static pressure contours in the nozzle passage among three radial gap configurations

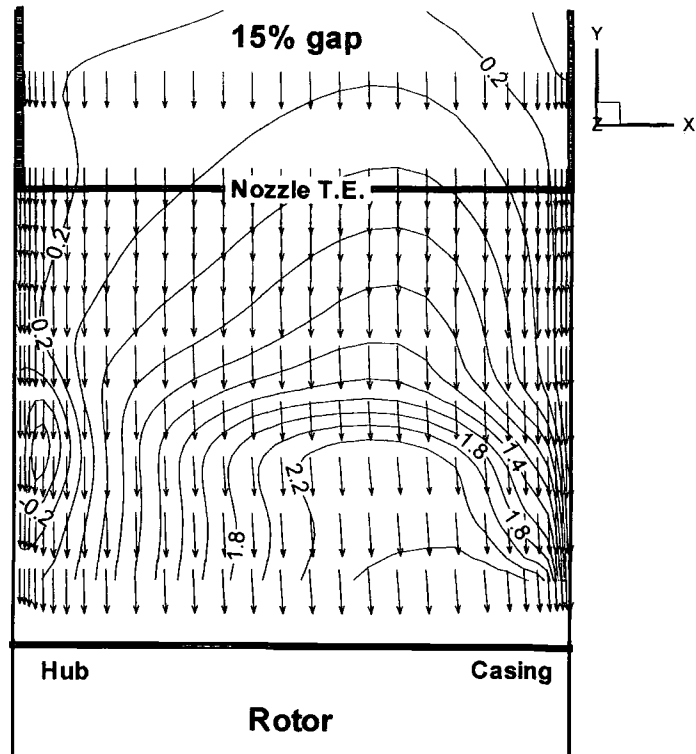


Figure 8-10 Axial flow velocity contours and flow velocity vectors in the vaneless space for 15% gap configuration

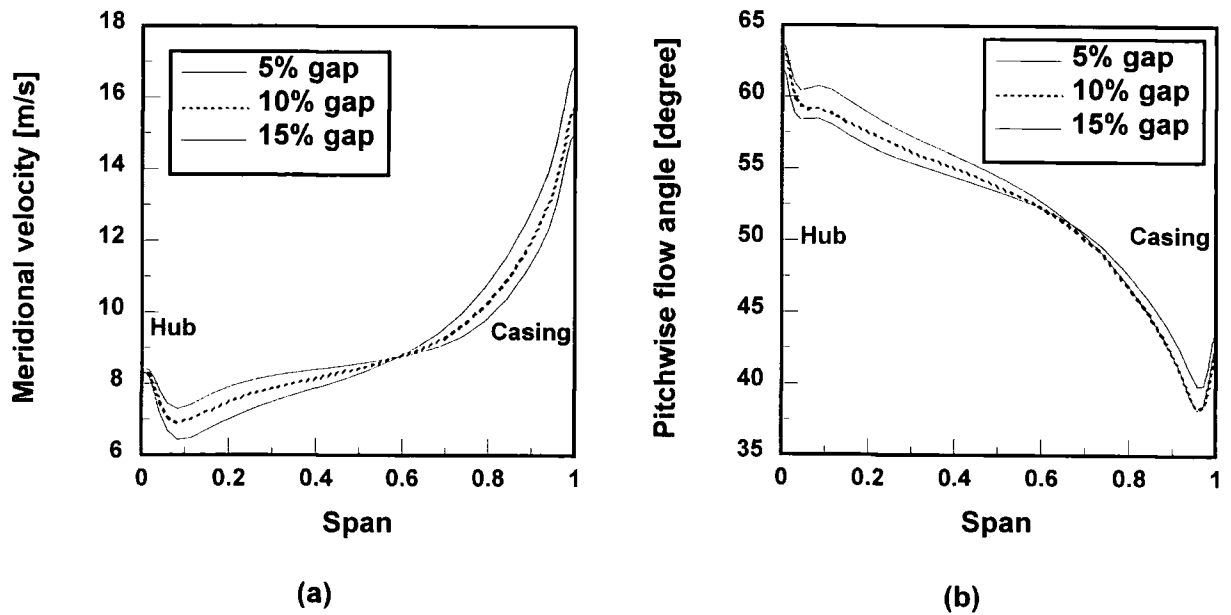


Figure 8-11 Comparison of spanwise meridional velocity distribution (a) and the relative flow angles (b) among three radial gap configurations

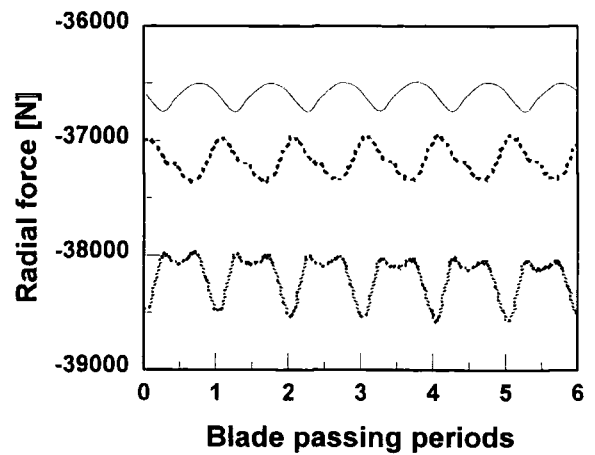
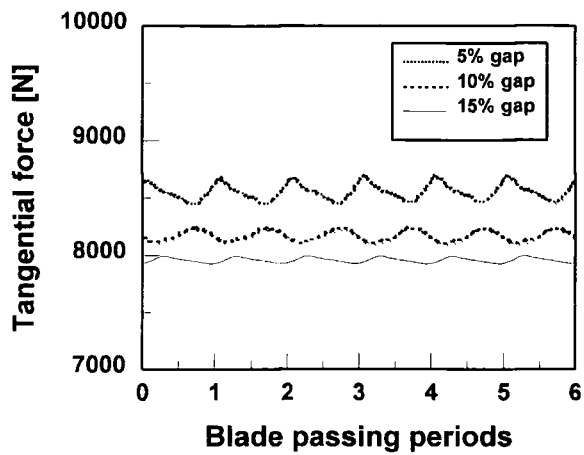
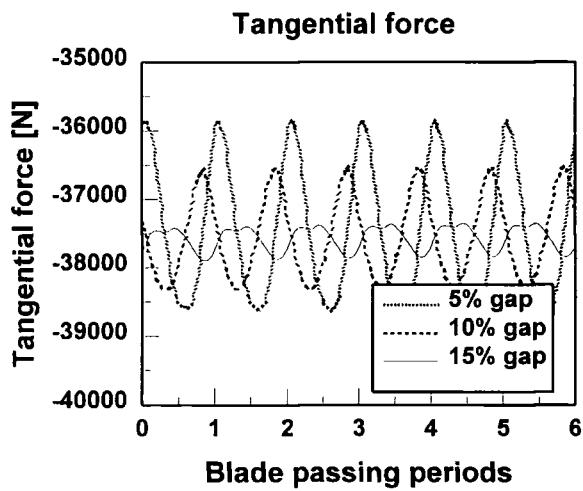
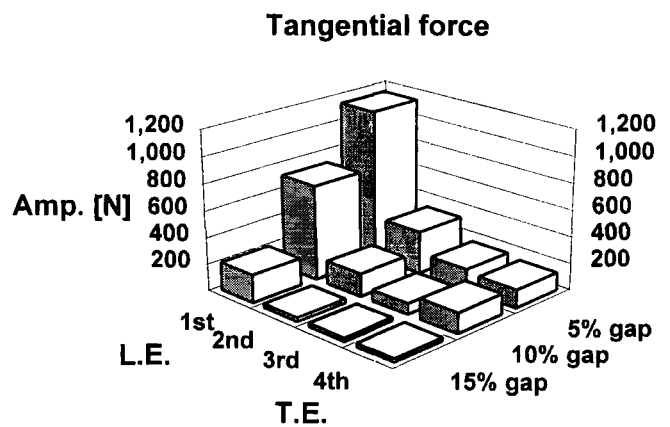


Figure 8-12 Comparison of histories of tangential and radial force components on the nozzle vane among three radial gap configurations



(a)



(b)

Figure 8-13 Comparison of blade force histories (a) and amplitudes of force fluctuation (b) on the turbine rotor among three radial gap configurations

